

FIELD-ION MICROSCOPY OF SUPPORTED NANOMETER SIZE AU
CLUSTERS AND CARBON NANOTUBES

A Thesis

Submitted to the Faculty

of

Purdue University

by

Daniel Lee Lovall

In Partial Fulfillment of the
Requirements for the Degree

of

Doctor of Philosophy

December, 1997

This thesis is dedicated to my parents Leland and Debra Lovall, and to the memory of my mother Adrienne.

ACKNOWLEDGMENTS

I would like to thank Prof. Ron Reifenberger for his support and insight during the course of this work. I would also like to thank Prof. Ron Andres for all the help he has given me during my research.

Thanks also to all my mentors and colleagues (each was a little of both) for many helpful lessons and discussions during my stay at Purdue: Barrett Gady, Michael Buss, Seunghun Hong, Todd Keaffaber, Matt Dorogi, David Schleef, Mario Paniccia, Tom Miller, Julio Gomez, and Jeff Bielefeld. I also would like to thank Elton Graugnard for his help this last summer in obtaining and analyzing the data on carbon nanotubes.

I also am grateful to Dr. Dilip Paithankar for providing the atom coordinates used in some of the FIM image simulations, and to Dr. Tom Castro and Dr. Gary Kellogg for extremely valuable discussions during the initial phases of this work. I cannot forget David Lubelski for sharing his vast knowledge of vacuum systems. Dr. Blair Stringfellow also lent the use of the HEP theodolite, which allowed me to align the tip in the cluster beam.

Lastly, I would like to thank my family and friends for their support during this part of my life, without which I could not have done this.

This research was funded under NSF Grant 9522248-CTS.

DISCARD THIS PAGE

TABLE OF CONTENTS

	Page
LIST OF TABLES	vi
LIST OF FIGURES	vii
ABSTRACT	xii
1. INTRODUCTION	1
2. CLUSTERS	5
2.1 Cluster Structure	5
2.2 Stability of Clusters	11
2.2.1 Quasimelting	11
2.2.2 Cluster-Substrate Interactions	13
2.2.3 Cluster Desorption in High Electric Fields	17
3. FIELD EMISSION AND FIELD-ION MICROSCOPY: THEORETICAL CONSIDERATIONS	21
3.1 FEM Principles	22
3.2 FIM Principles	24
3.2.1 Field Ionization	24
3.2.2 Performance of the FIM.	29
3.2.3 Simulation of FIM images	34
4. EXPERIMENTAL	37
4.1 Field-ion Microscope for cluster studies	37
4.2 Field Emission Microscope for Carbon Nanotube Studies	39
4.3 Preparation of W and Pt Field-ion Emitters	41
4.3.1 Etching	41
4.3.2 Secondary preparation	43
4.3.3 Other techniques	44
4.4 Cluster Production	45

	Page
5. EXPERIMENTAL RESULTS	52
5.1 Depositing Clusters on Field Emission Tips	52
5.1.1 Cluster Capture	52
5.1.2 Cluster Deceleration	53
5.2 Au Clusters on W Substrate	57
5.3 Au Clusters on Pt Substrate	61
5.4 Au Clusters on Pt/Ir Substrate	67
5.5 Observed Physical Characteristics of Clusters	73
5.5.1 Structure	73
5.5.2 Cluster Stability	74
6. CARBON NANOTUBE STUDIES	77
6.1 General Considerations	77
6.1.1 Physical Properties	77
6.1.2 Electrical Properties	78
6.2 Experimental Results	81
6.2.1 Nanotubes Included in This Study	81
6.2.2 Field Emission From Single Walled Carbon Nanotubes	82
6.2.3 Total Energy Distribution of Field Emitted Electrons	82
6.2.4 Field-ion Microscopy of SWNT Bundles	86
7. CONCLUSIONS	95
7.1 Supported Nanometer-Size Au Clusters	95
7.2 Carbon Nanotubes	96
7.3 Recommendations and Conclusion	97
LIST OF REFERENCES	99
APPENDICES	
Appendix A: A Listing of Programs Used During This Research	104
Appendix B: Cluster Coordinates	107
Appendix C: Carbon Nanotube Coordinates	120
VITA	132

DISCARD THIS PAGE

LIST OF TABLES

Table	Page
2.1 Characteristics for truncated octahedra with N atoms [1].	7
2.2 Characteristics for icosahedra with N atoms.	8
2.3 Summary of lattice spacing mismatches with Au(111). Qualitatively, Au clusters are expected to wet more readily on surfaces with a large lattice mismatch than on surfaces with a small lattice mismatch.	17
2.4 Values of the surface free energy for various cluster and tip materials [2].	19
3.1 Best Image Fields for various image gases [3].	34
4.1 Summary of cluster annealing studies using HRTEM [4].	47
4.2 Size distribution data for the plot in Fig. 4.7.	51
5.1 Results of cluster deceleration experiments. For the expected mean particle diameters, d_p assumes no acceleration downstream of the capillary exit of the annealing furnace. In column 3 we assume an initial particle velocity $v_{p,i} = 510$ m/s given by Eqn. 5.1. The next column, d_{p2} assumes complete acceleration in the free jet downstream of the capillary exit, with $v_{p,i} = 1766$ m/s, from Eqn. 5.2 above. The experimental size distributions in the final two columns suggest that the actual initial cluster velocity is located between these two values.	59

DISCARD THIS PAGE

LIST OF FIGURES

Figure	Page
2.1 The truncated octahedron (TO) series of clusters: (a) TO-, (b) TO, (c) TO+. Clusters with this shape follow a single crystal motif.	8
2.2 Multiply twinned particles: (a) Decahedron (Dh), (b) Icosahedron (Ih), (c) Marks Decahedron (M-Dh).	9
2.3 Excess energy Y divided by $N^{\frac{2}{3}}$ versus $N^{\frac{1}{3}}$ for Au clusters [5].	10
2.4 Phase diagram for small particles proposed by Ajayan and Marks [6]. The five regions identified in this diagram correspond to icosahedral (Ic), decahedral (Dh), single crystal (SC), quasimelting (QM), and liquid (L) particles.	14
2.5 Comparison of the force F_S required to separate a spherical Au cluster from a W tip to the electrostatic force F_E on the upper half of the cluster for the best image fields of Ar (180 MV/cm), H (220 MV/cm), and Ne (375 MV/cm).	20
3.1 Field emission micrograph of a (110) oriented W tip. Note the 4-fold symmetry about the central (110) facet.	25
3.2 Field emission micrograph of a (111) oriented Pt tip. Note the 3-fold symmetry about the central (111) facet.	26
3.3 Potential barrier associated with field emission. The solid line represents the deformation of the barrier by the applied field, while the dashed line includes the reduction by the electron's image charge.	27
3.4 FIM image of a (100) oriented Pt/Ir tip. $V=10\text{kV}$, $T \simeq 100\text{K}$	30
3.5 Potential energy diagram for an electron in an gas atom approaching a tip in a high electric field. I is the ionization energy for the gas atom and ϕ is the work function of the metal [3].	31

Figure	Page	
3.6	Image formation in FIM. An approaching gas atom strikes the tip and rebounds several times, becoming thermally accommodated with the tip. After it is ionized, it is accelerated to the imaging screen.	32
3.7	Schematic for thin shell simulations of FIM micrographs.	36
3.8	Illustration of the effect of varying the shell thickness on simulated images of a 309 atom icosahedral cluster, such as the one shown in Fig. 2.2b. a) $t = 0.75\text{\AA}$ b) $t = 1.00\text{\AA}$ c) $t = 1.50\text{\AA}$	36
4.1	FIM designed for the study of supported nanoclusters.	39
4.2	Close up of tip assembly. 1) Tip, 2) Cooling braid, 3) Tip manipulator, 4) Macor insulating stage, 5) High voltage electrical leads.	40
4.3	A single element of a channel plate. A potential of 1000V is applied between the front and back surfaces of the plate, causing a cascade of electrons when any impinging electrons or ions strike it [7].	40
4.4	Experimental setup for taking Fowler-Nordheim data.	42
4.5	Schematic of the Purdue Multiple Expansion Cluster Source (MECS) [8, 9].	48
4.6	TEM of MECS clusters deposited on a Cu TEM grid.	49
4.7	Histogram plot of the cluster size distribution in Fig. 4.6.	50
5.1	Schematic for alignment of the tip with the MECS cluster beam. The beam passes into the FIM and through the probe hole in the phosphor screen and strikes the alignment viewport at a point which has been marked for reference. A theodolite is used to align the FIM tip in the beam line. Afterwards the FIM tip is rotated 180° to point towards the phosphor screen.	54
5.2	Comparison of the cluster size distribution before (front) and after (back) deceleration. Note that deceleration causes the mean size to shift upwards.	58
5.3	Field emission image of a ~ 2 nm Au cluster deposited on a W tip. This cluster has been “cleaned” by successively applying higher positive biases with respect to the imaging channel plate.	62
5.4	FIM of a ~ 2 nm Au cluster deposited on a W tip. The cluster was held at a temperature of 100K. Ar was used as an imaging gas.	62

Figure	Page
5.5 (a) A 202 atom cluster shown in the orientation which best fits the experimental image in Fig. 5.4. The shaded atoms represent the atoms imaged in the experiment.(b) Comparison of a simulated FIM image of a 202 atom cluster to the experimental image in Fig. 5.4.	63
5.6 A field-ion image from a ~ 1 nm Au cluster, annealed in flight to a temperature of 1800 K, and soft landed on a Pt field emission tip. The approximate temperature of the tip and cluster is 100 K.	65
5.7 (a) The 39 atom cluster shown in the orientation that best fits the experimental FIM image. The shaded atoms represent those imaged in the experiment. (b) Simulated FIM micrograph (squares) of a 39 atom TO Au cluster which has been rotated to an orientation approximating that of the cluster imaged in Fig. 5.6. The contour plot shows the intensity of the recorded FIM image.	66
5.8 Field emission image of a Pt/Ir tip oriented in the 100 direction.	68
5.9 Field-ion image of an unannealed Au cluster. $V=4800V$, $T \simeq 100$ K.	69
5.10 Contour plot of a field-ion image of an unannealed Au cluster, enhanced to show dimly imaged atoms. $V \simeq 5300$ V, $T \simeq 100$ K.	70
5.11 (a) Proposed icosahedral structure which is close to that which produced Fig. 5.9. The shaded atoms are those which are imaged in Fig. 5.10. (b) Comparison of simulated image from the structure in (a) to the experimental image. The two show fair agreement. Discrepancies suggest that the cluster is either deformed by the substrate or a structure other than a “perfect” icosahedron.	71
5.12 (a) Proposed multiply twinned structure for an unannealed Au cluster which is closer to the experimental data which produced Fig. 5.9. Comparing this to the “ideal” decahedron in (b), note that the edges of the structure in (a) are of unequal lengths.	72
5.13 (a) Composite map for an annealed cluster deposited on a W tip, showing the underlying structure represented in (b).	75
5.14 The ridge structure consisting of three or four atoms in (a) was imaged on an unannealed cluster deposited on a Pt/Ir tip, on 5/6/97 at 14:08:41. It then disappeared and later returned in (b), at 21:50:22.	75

Figure	Page	
5.15	These images demonstrate the stability of an unannealed Au cluster deposited on a Pt/Ir tip. The image in (a) was taken at 4.8 kV and has been enhanced so the atoms are more clearly visible. The image in (b) was taken 9 min, 48 s later at 5.3 kV. This cluster remained essentially unchanged for over 12 minutes before the increased electric field caused it to slowly field evaporate.	76
6.1	Method of characterizing SWNTs. The hexagonal basis vectors \vec{a} and \vec{b} define a line perpendicular to the axis of the tube. If one cut a belt out of a sheet of graphite defined by $n\vec{a} + m\vec{b}$ and wrapped it so that the axis of the buckytube were perpendicular to $n\vec{a} + m\vec{b}$, the result would be a (n,m) buckytube. The tube can also be described by specifying the chiral angle θ , which describes the tube's helicity.	79
6.2	(a) A (10,10) nanotube. (b) A (10,0) nanotube. The tubes included in this study are expected to be (10,10) nanotubes, based on size and energy considerations.	80
6.3	Single walled carbon nanotube (SWNT) mounted on a Pt field emitter. The bundle thickness is uneven, with the radius ranging between $55 \pm 5 \text{ \AA}$ to $85 \pm 5 \text{ \AA}$. The end of the bundle is not resolved due to thermal vibrations.	83
6.4	Contour plot of a field-emission micrograph of a SWNT.	84
6.5	Fowler-Nordheim plot for a SWNT. The field compression factor β , and the bundle radius are given in the figure.	85
6.6	Total energy distribution of electrons field emitted from a SWNT bundle. For this fit, $T=100\text{K}$, $\phi=5.1\text{eV}$, $F=6.0 \times 10^7 \text{ V/cm}$	87
6.7	He FIM image of a SWNT bundle. This was taken at $\sim 100\text{K}$, 5700V	91
6.8	Scenarios used in simulations of FIM images from buckytubes. 1) bundle with one or more tubes sticking out further than the rest. 2) Bundle with all tubes terminating together. 3) Bundle with a rounded end form.	91
6.9	Simulated image from a single (10,10) nanotube. Note that the image spots from each of the C doublets terminating the tube have coalesced into single spots.	92
6.10	Simulated image from a single (10,0) nanotube.	92

Figure	Page
6.11 Simulated images from a bundle of 19 (10,10) nanotubes. Focus your attention on the tube in the center of the bundle. a) Original orientation. b) Central tube rotated 10° clockwise. c) Central tube rotated 20° clockwise. d) Central tube rotated 30° clockwise.	93
6.12 Simulated image from a bundle of SWNTs with a rounded end form. . .	94

ABSTRACT

Lovall, Daniel Lee. Ph.D., Purdue University, December, 1997. Field-ion Microscopy of Nanometer Size Au Clusters and Carbon Nanotubes. Major Professor: Ronald G. Reifengerger.

The structure and stability of nanometer-size Au clusters is investigated using field-ion microscopy. Molecular dynamics simulations of Au clusters in the 2-4 nm size range predict a truncated octahedral equilibrium structure. By comparing experimental field-ion microscope (FIM) images of Au clusters placed on the apex of a FIM tip to simulated images, a determination of the structure and orientation of clusters supported on a variety of substrates (W, Pt, Pt/Ir) is made. We find that clusters annealed in the gas phase attain a truncated octahedral shape. Unannealed clusters are found to exist as multiply twinned particles.

The electrical and structural properties of carbon nanotubes are investigated using field emission and field-ion microscopy. Measurements of the total energy distribution (TED) of field emitted electrons from a bundle of single walled nanotubes show that the bundle has metallic electrical properties. A determination of the work function of this bundle is made. Field-ion images of the same bundle are compared to simulated images from bundles of nanotubes with different end forms.

1. INTRODUCTION

Recently, nanometer-size systems and structures have been a topic of great interest. While the many researchers in this field use a variety of techniques and materials to create and study such systems, most share a common element: some kind of cluster or quantum dot. A cluster is a group of atoms which come together by self assembly. They can be comprised of anywhere between 2 and ~ 10000 atoms, and represent a sort of bridge between the atomic and bulk size regimes.

Much of the great interest in clusters is fueled by the many possible applications of clusters and the related nanoscale technologies. A well known and time-tested adage of the computer industry, Moore's law states that the minimum feature size of semiconductor devices has decreased by a factor of 2 every 18 months [10]. As components shrink quantum mechanical effects become more and more important, and eventually a fundamental limit on the smallness of these components will be realized. The observation of novel electronic properties such as single electron tunneling (SET) effects in cluster systems at room temperature [11] suggest that cluster assembled materials may be ideal for this purpose. Given the Coulomb staircase effects seen in such systems, one could envision a computational device which operates using multi-state logic instead of the binary logic of current devices.

The role of clusters in chemical systems is also intriguing. As particle size decreases, the ratio of surface atoms to interior atoms increases. A 38 atom cluster has 32 surface atoms and 6 interior atoms, while a 13 atom icosahedral cluster has 12 surface atoms and only 1 interior atom. Clearly, cluster materials are potentially more chemically reactive than bulk materials.

Clusters and other nanometer-scale materials also have many more esoteric applications. Already, Dai *et al.* have shown that carbon nanotubes (“buckytubes”) mounted on the ends of atomic force microscope (AFM) cantilevers can dramatically improve the resolution obtained in AFM micrographs [12]. Buckytubes also have potential as electron sources in flat-panel field emission displays for computers [13].

Concerns about the stability of nanometer size clusters represent a limitation on any potential applications. It has been known for some time that small particles do not necessarily possess static structures, but can rather have structures that evolve with time [14, 15, 16]. Many researchers have reported the observation of complete, apparently random restructuring of the atoms in clusters [15, 16]. This has been dubbed “quasimelting” since the clusters appear to exist in a sort of semi-molten state, switching from structure to structure.

The origin of these fluctuations is not clearly understood. The implications they have on possible applications of nanometer size particles however, is understood all too well. Since the electrical properties of these clusters is highly dependent on the structure they assume, any structural fluctuations could severely limit the performance of the performance of any device containing them.

Traditionally, high-resolution transmission electron microscopy (HRTEM) has been used to study the structure and stability of clusters [15, 16, 4]. Other techniques used include X-ray diffraction, ellipsometry, and mass spectrometry. Scanning probe techniques such as atomic force microscopy (AFM) and scanning tunneling microscopy (STM) have led to valuable insights about the elastic properties [17, 18, 19] and electronic properties [11, 20] of clusters, but very little information about the structure of clusters can be gained using AFM and STM unless tip convolution effects can be deciphered [21].

HRTEM is the only technique commonly used that is capable of imaging clusters with atomic scale resolution. Its use has often come into question with regards to studying the stability of clusters. Most studies focus on cluster which are unannealed, and are therefore metastable structures [22]. The TEM operates by focusing a high

energy electron beam on the sample, and many researchers have contended that this heats the clusters, causing them to fluctuate [16]. Charging effects due to the electron beam also undoubtedly have an effect, and could influence the structure and confound the issue of stability.

In light of the concerns about heating and charging effects in the HRTEM, it would be desirable to use other techniques to study quasimelting in clusters. Lin *et al.* studied the energy of field emitted electrons from Au clusters on a W support tip [23]. Fluctuations in the emission current were interpreted as the result of morphological fluctuations, but no direct observations of quasimelting were made. The field emission microscope (FEM) lacks the resolution to directly see quasimelting as it occurs.

Prior to Lin's studies of Au clusters with the FEM, Castro *et al.* developed techniques to capture and study nanometer-size clusters on the end of a field-ion microscope (FIM) tip [24]. The FIM is capable of true atomic resolution; in fact it was the first technique capable of true atomic resolution [25]. It is also operated at cryogenic temperatures, which should minimize any structure fluctuations which are due to thermal effects.

While the FIM has rarely been used to study clusters, the field emission microscope (of which the FIM is a variant) has a long history of studying small structures deposited on the end of tips. In the 60's many researchers used the field emission microscope to study nanometer size whiskers of Hg, C, Au, Ni, and other materials [26]. Many researchers also used the field emission microscope to study organic molecules [26, 27, 28]. Recently the FIM has been used to study diffusion of single atoms [29, 30] and raft like surface clusters [31, 32, 33].

In light of the advantages the FIM has to offer in the study of small clusters, a FIM was built specifically for the purpose of studying nanometer size Au clusters deposited on FIM tips. Techniques were developed for the characterization of clusters by interpreting FIM micrographs. The results of this comprehensive effort is presented below.

A brief summary of this thesis is as follows: Chapter two focuses on clusters and the issues behind the structure and stability of them. Chapter three presents the theory of operation of the field emission microscope and the FIM. Chapter four includes a discussion of the experimental aspects of this work, and chapter five presents the results. A brief introduction to carbon nanotubes, as well as preliminary experimental results from FEM and FIM studies of carbon nanotubes, are presented in chapter six. In chapter seven, the conclusions that can be drawn from this work are discussed and recommendations for further studies are presented.

2. CLUSTERS

2.1 Cluster Structure

The equilibrium structure of a cluster of atoms is a complicated issue. Primarily, it is one of energy considerations, but the history and kinetics of cluster growth also come into play when determining the structure for a given cluster [16]. Molecular dynamics simulations, based on a Lennard-Jones potential for Ar clusters, or on an embedded atom model (EAM) for metal clusters, have identified a number of structures which are energetically favorable. I will present a review of the findings for metal clusters, specifically Au clusters.

Clusters structures follow one of two basic motifs, single crystal or multiply twinned. As their name suggests, single crystal clusters are made of a single crystal domain. Multiply twinned clusters consist of two or more crystal domains. The structure is mirrored, or twinned across the boundary, hence the name. Fig. 2.1 shows the single crystal shapes based on the truncated octahedron (TO). The TO- is formed by removing a layer of atoms from the square (100) faces of the TO; by adding a layer of atoms to the square (100) faces a TO+ is formed. Three shapes for multiply twinned particles are shown in Fig. 2.2, the decahedron (Dh), icosahedron (Ih), and the so-called Marks-decahedron (M-Dh). Tables 2.1 and 2.1 give an overview of the relative size of clusters for truncated octahedra and icosahedra.

The earliest attempts to determine the equilibrium structures for small particles relied on a Wulff construction, which gives the minimum energy shape for single crystal particles for a given volume [16]. It is worth noting that the Wulff construction predicts a truncated octahedron as the minimum energy shape for FCC metals. The Wulff construction however does not predict such structures as multiply twinned

particles. In an effort to account for such particles, Marks has proposed a modified Wulff construction [16].

Formally, for a particle with facets of area A_i , the total free surface energy G is given by,

$$G = \sum_i \gamma_i A_i + \sum_{jk} e_{jk} \sigma_{jk}^i. \quad [2.1]$$

Here, γ_i is the free energy of the i th face per unit area, e_{jk} are the internal strains and σ_{jk}^i are the surface stress tensors, given by

$$\sigma_{jk}^i = \gamma_i + \frac{\partial \gamma_i}{\partial e_{jk}}. \quad [2.2]$$

Hence, we see that finding the minimum energy structure is an interplay between the surface free energy and the internal strains in the particle. For very small particles, twinning allows a lower total energy even though there is a certain amount of strain induced by the twin boundaries. As the particle size increases, the internal strain energy grows proportional to the volume while the surface energy grows proportional to the surface area. Eventually a critical size is reached, and a single crystal motif becomes favorable [34].

Though simple, Wulff constructions often require input parameters which are difficult to determine experimentally. Researchers have therefore employed molecular dynamics computer simulations utilizing the embedded atom method (EAM) [34, 4, 5]. For a cluster containing N atoms this is essentially an iterative energy minimization technique [5] which begins by writing the total potential energy in the form:

$$E = \epsilon N = \epsilon_b N + \epsilon_\sigma N + \alpha \epsilon_s N^{\frac{2}{3}}. \quad [2.3]$$

The terms ϵ , ϵ_b , ϵ_σ , and ϵ_s are the average potential energy in the cluster, potential energy in bulk, strain energy, and surface energy per atom, respectively. The α term is a constant related to the cluster geometry [34].

Table 2.1 Characteristics for truncated octahedra with N atoms [1].

N	edge atoms	number of rows in cluster	Distance Between (100) faces	Distance Between (111) faces
38	2	5	0.77Å	0.72Å
201	3	9	1.63	1.42
586	4	13	2.45	2.12
1289	5	17	3.26	2.83
2406	6	21	4.08	3.54
4033	7	25	4.90	4.25
6266	8	29	5.71	4.96
9201	9	33	6.53	5.66

A more useful form can be found by rearranging Eqn. 2.3 to find the excess energy, Y [5, 34]:

$$Y = (\epsilon - \epsilon_b)N^{\frac{1}{3}} = \epsilon_\sigma N^{\frac{1}{3}} + \alpha\epsilon_s. \quad [2.4]$$

By plotting Y vs. $N^{\frac{1}{3}}$, we can compare the energetic favorability of clusters of different sizes and structures, as shown in Fig. 2.3. A brief inspection of this figure reveals that truncated octahedra are clearly favored for larger ($N > 300$) clusters but there is little difference in Y for icosahedra and truncated octahedra at smaller sizes.

Very recently, theoretical studies of the structural evolution of Au clusters by researchers at Georgia Tech [22, 35] have identified a number of other structures which appear to be energetically favorable to TO clusters in the size range which we are focusing on. These include the TO+ clusters and the so-called ‘‘Marks decahedron’’ (M-Dh)[16, 22, 22], which is essentially a truncated decahedral structure.

Table 2.2 Characteristics for icosahedra with N atoms.

N	edge atoms	radius (nm)
13	2	0.4
55	3	0.6
147	4	0.8
309	5	1.1
561	6	1.3
923	7	1.6
1415	8	1.8
2057	9	2.0
2869	10	2.3
3871	11	2.5
5083	12	2.7

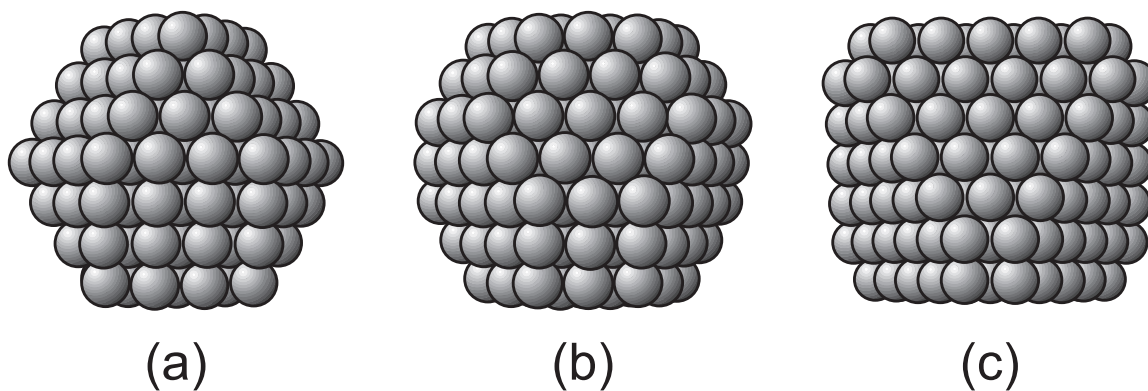


Figure 2.1 The truncated octahedron (TO) series of clusters: (a) TO-, (b) TO, (c) TO+. Clusters with this shape follow a single crystal motif.

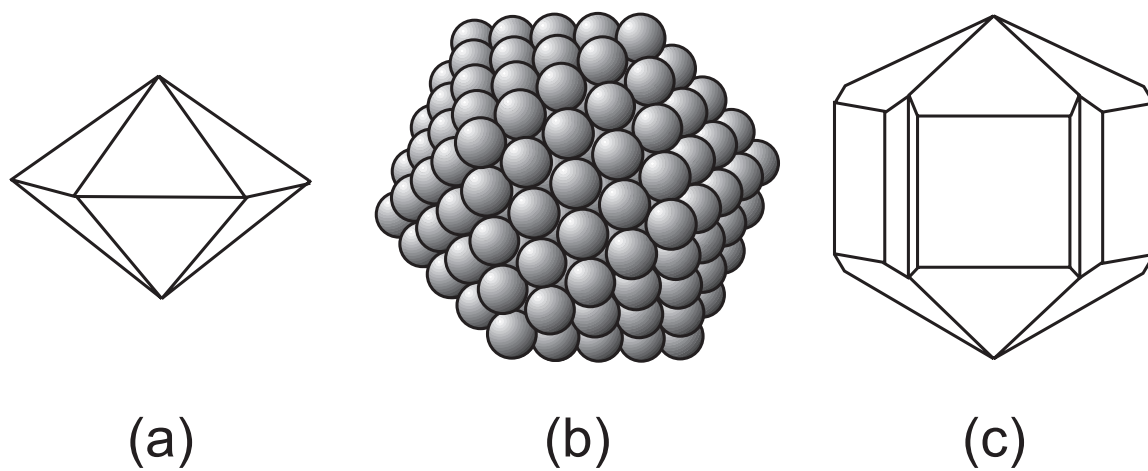


Figure 2.2 Multiply twinned particles: (a) Decahedron (Dh), (b) Icosahedron (Ih), (c) Marks Decahedron (M-Dh).

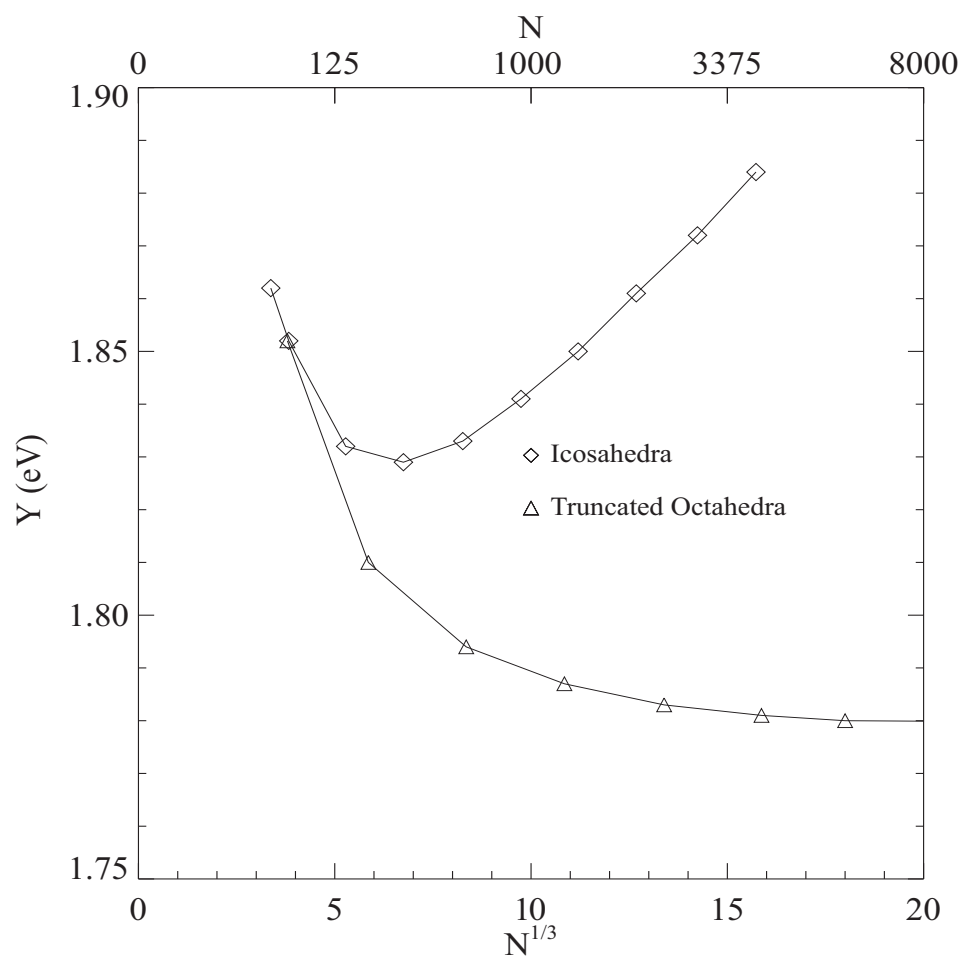


Figure 2.3 Excess energy Y divided by $N^{2/3}$ versus $N^{1/3}$ for Au clusters [5].

2.2 Stability of Clusters

Structural instabilities in nanometer-size clusters generally fall into three categories. In the first, the changes are due to inherent properties of the cluster. The structure taken on by a cluster may represent a metastable state. The cluster may undergo rapid fluctuations between two equilibrium states which are separated by a shallow energy barrier.

In the second, structural changes occur due to interactions between the cluster and the substrate [16]. Depending on the strength of the cluster-substrate interaction forces, the cluster may be “squished” against the substrate. In extreme cases the cluster may wet, collapsing on the supporting substrate [36].

The structure can also be influenced by external factors. Examples of this are heating due to energetic electron or ion beams, heating due to lasers, or charging effects due to electron or ion beams. This method is often cited when discussing the origins of quasimelting, since most studies of quasimelting utilize HRTEM, which bombards the sample with a high energy electron beam. In FIM and FEM these effects are minimal, since neither utilize techniques could produce such effects. We therefore focus on the first two categories in this thesis.

2.2.1 Quasimelting

The origin of quasimelting is a hotly debated topic, as the phenomenon represents a limitation on the size of any clusters used in any devices which may be the end result of cluster research. The electrical properties of clusters are highly dependent on the structure they assume; any cluster which is so small that its structural properties are unstable clearly also has unstable electrical properties.

To date most of the experimental evidence for quasimelting stems from HRTEM studies of small clusters in the 400 atom size range. Iijima *et al.* first reported structural instabilities in 2 nm clusters in 1986 [15]. They observed nanocrystals which moved and changed structure on Si or an amorphous C substrate while under electron

beam irradiation. They noted that a higher electron flux was required to initiate the fluctuations than was required to sustain them. The particles also exhibited a lower rate of change when resting on a conducting support such as amorphous carbon, implying that charging effects somehow play a role.

Ajayan and Marks also reported experimental evidence for quasimelting in 2-3 nm particles on a MgO surface [37]. They observed that the structural changes occur even at very low (below $0.1\text{A}/\text{cm}^2$, or $6.24 \times 10^{17}\text{e}/(\text{s cm}^2)$) flux levels.

In the experimental studies mentioned [15, 37, 16] quasimelting was observed while the clusters were under irradiation by a high energy electron beam. Estimates of the cluster temperature under these conditions are $\sim 1100\text{K}$ [15], below the melting temperature of the particles but near temperatures which are typically used when annealing clusters in the Purdue cluster source, a multiple expansion cluster source (MECS). Since the energy barriers separating structures are very shallow, it is possible that the added thermal energy could enable the cluster to perform a sort of random walk in configuration space, changing structure with time.

Molecular dynamics studies of cluster structure have shown that so-called “ideal” cluster shapes are only local energy minima in configuration space. There are many possible configurations for a given number of atoms which come together to form a cluster, all separated by relatively shallow energy barriers.

Theoretical treatments of cluster structure have almost unilaterally focused on clusters comprised of a limited set of atom counts, usually referred to as the “magic numbers”. A notable exception to this would be the studies of Paithankar *et al.*, who considered icosahedral clusters capped with a partial outer layer [4]. Indeed, studies of cluster size using mass spectrometry have confirmed that there are certain preferred sizes. Such preferred sizes correspond to ideal structures with complete shells. There are however no *a priori* reasons for clusters to *only* exist with complete shells. Extra atoms could be the key to understanding the mechanisms behind quasimelting. The addition of a single atom has been observed to completely rearrange raft-like surface

clusters [31, 32, 33]. It is possible that such reconstructions could occur in larger clusters as well.

Surface energy plays a large role in the equilibrium structure of clusters, mainly due to the large increase in the surface to volume ratio for nanocrystals [16, 4]. The increase in surface energy also plays a role in the melting point depressions which have been observed in small clusters [38, 39, 5]. It would not then be surprising if the increased surface energy in clusters played a role in quasimelting.

Theoretical treatments of quasimelting have been guided by the assumption that the morphology of small particles is defined by a potential energy surface [16], just as in theoretical treatments of the equilibrium structure. In 1988 Ajayan and Marks extended this idea to include entropic effects and proposed a phase diagram for small particles [6], shown in Fig. 2.4. In this diagram they identify five different regions corresponding to multiply twinned particles (icosahedra and decahedra), single crystal particles (truncated octahedra), quasimelting particles, and liquid particles. While it is mainly qualitative in nature, it does put forth a scientifically intriguing point: regardless of its origins, quasimelting may represent an inherent property of small particles.

2.2.2 Cluster-Substrate Interactions

The relationship between a surface and a cluster resting upon it is often a very complex one. The strength of the interaction is very important. Strong interaction forces between the cluster and substrate will lead to flattening of deposited clusters. This was confirmed experimentally by Mahoney *et al.* when they compared the diameters of clusters as measured in the TEM to their heights as measured in the AFM [40]. They found that δ , the amount that the clusters were flattened, was in reasonable agreement with predictions made according to the Maugis and Pollack theory [41], or

$$\delta = \frac{a_{plastic}^2}{2R} \quad [2.5]$$

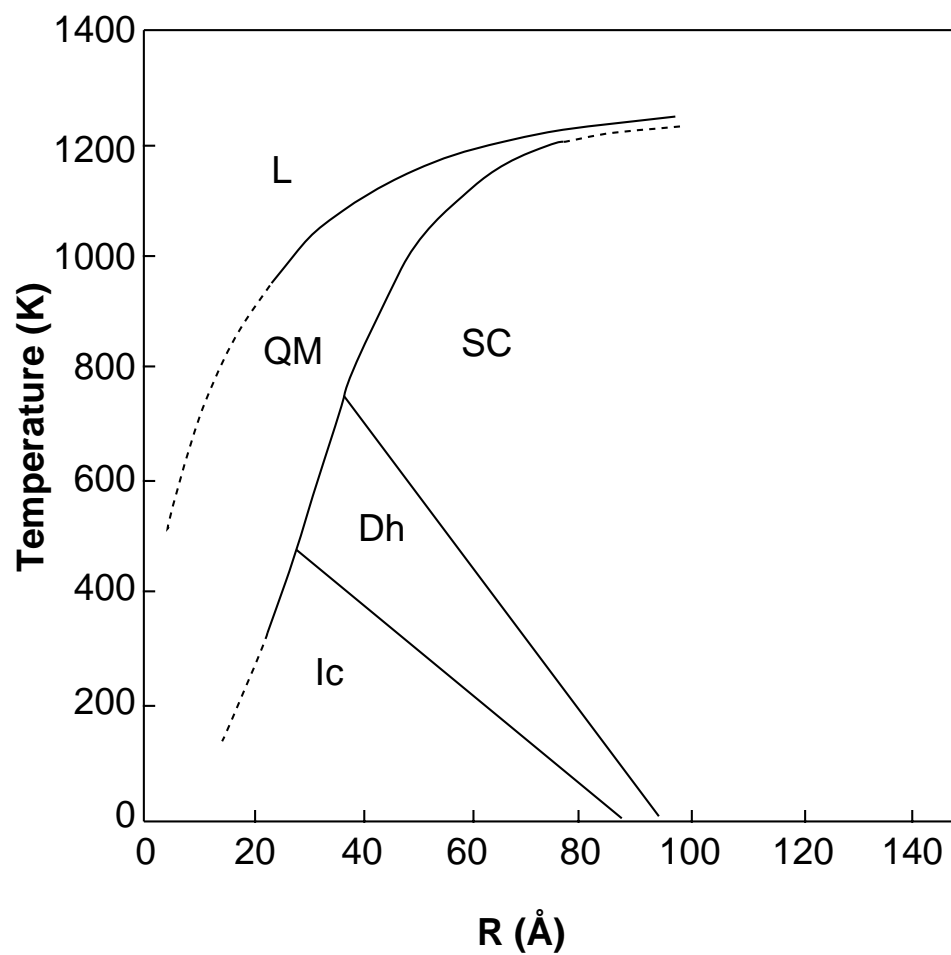


Figure 2.4 Phase diagram for small particles proposed by Ajayan and Marks [6]. The five regions identified in this diagram correspond to icosahedral (Ic), decahedral (Dh), single crystal (SC), quasimelting (QM), and liquid (L) particles.

where $a_{plastic}$ is the contact area of a metal sphere undergoing plastic deformation, given by

$$a_{plastic} = \sqrt{\frac{2WR}{3Y}}. \quad [2.6]$$

R is the radius of the metal sphere, while $W = 2\sqrt{\gamma_{cluster}\gamma_{substrate}}$ is the work of adhesion between the cluster and substrate. The γ terms are the surface free energies of the cluster and substrate, and Y is the yield stress of the metal from which the cluster is comprised.

The condition of the surface is very important, and the presence of contaminants can have a striking effect on the morphology of a supported cluster [16]. Chemisorbed species can cause an increase in the surface energy of the substrate, often resulting in a change in the surface lattice parameters [16]. This can lead to morphological changes in supported clusters.

MD simulations of supported Au nanostructures on a Ni(100) surface suggest that the settling and subsequent collapse of clusters begins with a spreading of the bottom layers of atoms [36], partly due to strains induced in both the cluster and the substrate by the large lattice mismatch between Ni(100) and Au. After this, the upper layers settle into vacancies left by the spreading bottom layer. Similar simulations of Au nanostructures on Au(111) substrates suggest that the spreading begins with an exchange mechanism similar to that observed in FIM studies of surface diffusion [36, 31]. The subsequent spreading and collapse occurs less readily than on the Ni substrate.

These observations suggest that selection of a suitable tip material is important for FIM work on supported nanoclusters. Care must be taken to choose a material which does not interact so strongly as to promote wetting of clusters on the tip substrate.

During the course of this research, W, Pt, and Pt/Ir tips were used as substrates for Au clusters. Au clusters are expected to land on the surface with a (111) face downward [40]. Therefore the lattice mismatch between the surface and Au(111)

cluster facet is a quantity of interest. A summary of these quantities is included in Table 2.2.2.

The importance of these considerations was seen in the relative speed with which clusters deposited on W tips wetted the surface. Clusters captured immediately after cleaning the tip were often observed to wet within seconds of impact. If there was a delay between tip cleaning and cluster deposition the clusters did not wet. Occasionally, a cluster would wet after a period of a few hours, but this was the exception and not the norm.

This observed dependence of the wetting behavior of Au clusters on the condition of the W substrate can be better understood by considering the adhesive forces involved. Ohmae *et al.*, used an FIM to study the adhesive force between Au atoms and a W substrate which has been given varying exposures to oxygen [42]. They found that increasing the amount of oxygen that the W tip is exposed to decreases the adhesion of Au atoms to the surface. In extreme cases, an adhesion force was not detectable.

This can be interpreted as follows: for a clean tip, the adhesion force between the W tip and the Au cluster is so great that the cluster wets the surface. As the tip is contaminated by exposure to O₂ and other gases present in the UHV chamber, the interaction between the cluster and tip is reduced enough that the cluster does not wet. If the tip is *too* contaminated however, the adhesion force may not be great enough to keep the cluster on the tip when it is subjected to the high electric field used in operation of the FIM. This may be why many of the clusters deposited on tips were removed by the electric field before they could be imaged.

While there is no data available for the adhesion of Au deposited on Pt and Pt/Ir surfaces, we can assume that the dependence on the oxygen coverage should be similar. In practice Pt and Pt/Ir tips are not as quickly contaminated since the sticking coefficient of O₂ molecules on Pt is not as great as for O₂ molecules on W. However, experimental observations under similar conditions showed that Au clusters

Table 2.3 Summary of lattice spacing mismatches with Au(111). Qualitatively, Au clusters are expected to wet more readily on surfaces with a large lattice mismatch than on surfaces with a small lattice mismatch.

Material	plane	d (Å)	difference from Au(111)
Au	(111)	2.35	-
W	(100)	3.16	34.5%
	(110)	1.58	-32.8%
Pt	(100)	1.96	-16.6%
	(111)	2.40	2.1%

did not wet as readily on Pt and Pt/Ir as they did on W. Clusters that were observed to wet in general took longer (over 10 minutes) to wet than those observed on W.

2.2.3 Cluster Desorption in High Electric Fields

An important consideration when using FIM to study supported clusters is the ability of the cluster to resist removal from the tip by the high electric fields present. For FIM experiments to succeed, the electrostatic force on the cluster must be less than that required to overcome adhesion of the cluster to the tip. From previously published work, rough limits can be set on the electric fields required to successfully perform FIM studies. For example, the evaporation field for single Au atom on a W tip is 260 MV/cm[43], while the field required to evaporate a Au atom from an Au surface is 350 MV/cm[30]. Electric fields somewhat less than these values should be used or otherwise the cluster may be field desorbed from the tip.

From these simple considerations, it is evident that FIM of supported clusters is possible providing that the best image field (BIF) of the imaging gas is sufficiently low, a result consistent with the experimental fact that FIM images of supported Au

clusters have been obtained using H_2 . However, the electrostatic force on the upper surface area of larger imaged clusters will increase faster than the adhesion force on the area in contact with the tip, and at some point the electrostatic force may exceed the force necessary to remove the cluster, even if the electric field is below the field necessary to perform field evaporation of single atoms. A model comparison of the electrostatic forces involved to the force required to pull a cluster from the tip is therefore in order.

We treat the supported Au cluster as a spherical object on the apex of a tip. The JKR theory of elastic solids [44] predicts that F_S , the magnitude of the force required to separate two elastic bodies is

$$F_S = \frac{3}{2}\pi WR. \quad [2.7]$$

where R is the radius of the spherical cluster and W is the work of adhesion, given by

$$W = 2\sqrt{\gamma_{cluster}\gamma_{tip}}. \quad [2.8]$$

Here $\gamma_{cluster}$ and γ_{tip} are the surface free energies of the cluster and tip, respectively. Values of the surface free energies for typical cluster and tip materials are listed in Table 2.2.3.

The electric field E exerts a net force F_E on the upper half of the sphere given by

$$F_E = \frac{\pi\epsilon_0}{2}E^2R^2. \quad [2.9]$$

In order for the cluster to remain on the tip,

$$F_E < F_S. \quad [2.10]$$

A plot of F_S and F_E for Au clusters on a W tip as a function of cluster diameter is shown in Fig. 2.5.

Table 2.4 Values of the surface free energy for various cluster and tip materials [2].

Material	γ (J/m ²)	note
Au	1.40	molten value
W	2.50	
WO _{2,3}	0.100	
WC	2.82	
Pt	2.30	

The results of this analysis suggest that FIM imaging of Au clusters with diameters less than ~ 5 nm is possible when using H₂ as an imaging gas and clusters with a diameter less than ~ 7.5 nm is possible when using Ar as an imaging gas. Based on these considerations, it seems likely that with care, small Au clusters can be observed in the FIM without field evaporating them as a whole from the tip provided Ar or H₂ is used as the imaging gas.

Wetting and migration of clusters must also be considered. Au atoms on a clean W surface have been observed to migrate from (110) to other regions of the tip [45]. It might be concluded that Au clusters will behave in a similar fashion. However, since cluster deposition is performed by placing the tip in a mixed stream of Au clusters and He carrier gas under conditions of high vacuum ($\sim 10^{-9}$ Torr), the surface of the tip is likely coated with a monolayer of O₂ or He, causing the surface free energy of the tip to decrease from the value expected for the clean metal. Qualitatively, this means that the cluster is less apt to wet the surface, and more likely to remain on W(110) for imaging, a prediction that agrees with experimental observations.

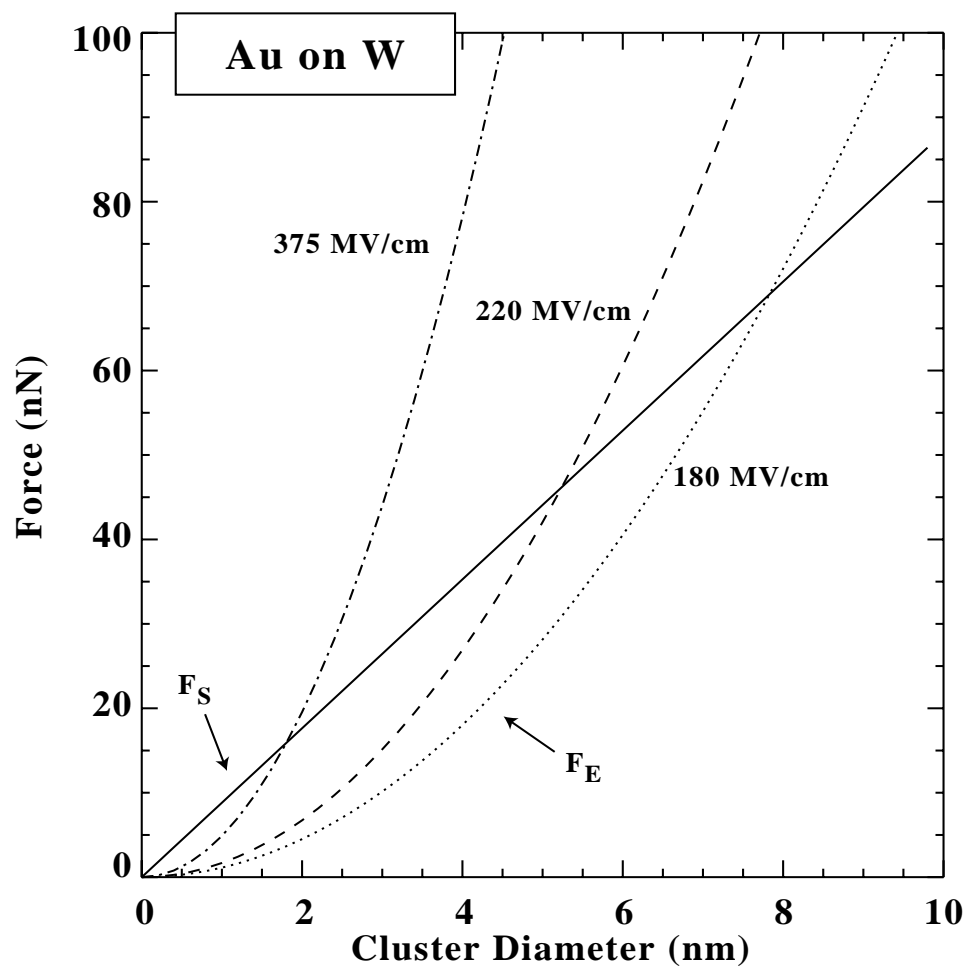


Figure 2.5 Comparison of the force F_S required to separate a spherical Au cluster from a W tip to the electrostatic force F_E on the upper half of the cluster for the best image fields of Ar (180 MV/cm), H (220 MV/cm), and Ne (375 MV/cm).

3. FIELD EMISSION AND FIELD-ION MICROSCOPY: THEORETICAL CONSIDERATIONS

Cold emission of electrons from metals had long been a topic of interest before the invention of the field electron microscope (FEM) in 1937. In 1928 Fowler and Nordheim treated the problem of cold emission of electrons quantum-mechanically, however it was not until Erwin Müller developed the FEM that their theory was satisfactorily verified.

In its simplest form, the FEM consists of a sharp metal cathode, or tip which is placed inside an ultra-high vacuum (UHV) chamber and pointed at a phosphor screen. A high voltage is applied between the tip and screen and the resulting high electric field deforms the potential barrier which holds the electrons inside the metal tip. The electrons are able to tunnel out of the tip and are subsequently accelerated towards the screen, forming a characteristic pattern.

The field-ion microscope (FIM) is essentially the same apparatus. It was developed in 1951 by the same man [25], and in 1956 it became the first technique capable of atomic resolution[46]. The key difference between the FIM and the FEM is a small amount of an imaging gas (usually He or H₂) which is admitted into the UHV chamber. In FIM, the tip is biased positive with respect to the screen, and the resulting electric field ionizes any gas atoms which come sufficiently close to the tip. The positive ions are accelerated towards the screen, forming an image of the surface of the tip. This image is essentially a stereographic projection of the positions of the atoms on the tip, much in the same way that maps in an atlas are a stereographic projection of the surface of the earth.

3.1 FEM Principles

The process of field, or cold emission of electrons is separate and distinct from that of thermal emission, where thermal energy is added to electrons which subsequently overcome the potential barrier at a metal-vacuum interface. In field emission, an electric field of about $3 - 5 \times 10^7$ V/cm is applied to the cathode, thus deforming the potential barrier holding electrons inside the metal as shown in Fig. 3.3. This enables electrons to tunnel out of the metal. Upon tunneling past the potential barrier, the electrons are accelerated by the high field to the screen, forming a pattern which is essentially a map of the work function variation on the surface of the tip. Representative field emission images are shown in Figs. 3.1 and 3.2.

Consider a tip with an end radius r and its apex at $x = 0$. The potential barrier near the surface of the tip is approximated by the superposition of the potential produced by the applied electric field and the contribution due to the electron's image charge. For $x > 0$ in the region $x \ll r$, this is given by

$$V(x) = -Fex - \frac{e^2}{4x}. \quad [3.1]$$

The transmission coefficient for an electron with energy E can be calculated using the WKB approximation to a one-dimensional potential barrier,

$$D[V(x), E] = \exp\left(-\frac{2}{\hbar} \int_{x_1}^{x_2} \{2m[V(x) - E]\}^{\frac{1}{2}} dx\right), \quad [3.2]$$

where x_1 and x_2 are the classical turning points, given by the zeros of the integrand.

The number of electrons of mass m emerging from the metal surface per second with energies between E and $E + dE$ is [47]

$$P(E)dE = D[V(x), E]N(E)dE. \quad [3.3]$$

The supply function $N(E)$ is the number of electrons incident on the surface per second. It is given by

$$N(E)dE = -\frac{4\pi m}{\hbar^3} \frac{dE}{1 + e^{\frac{E+\phi}{k_b T}}} \quad [3.4]$$

where ϕ is the work function of the metal and T is the temperature.

If $P(E)$ is integrated over all energies, one can also calculate the current density of electrons emerging from the surface. This is a standard result given by the Fowler-Nordheim equation [47],

$$j = \frac{1.54 \times 10^{-6} F^2}{\phi t^2(y)} e^{-6.83 \times 10^7 \frac{\phi^{\frac{3}{2}}}{F} v(y)} \quad (\text{in } A/cm^2.) \quad [3.5]$$

Here, F is the applied field in volts/cm, ϕ is the work function of the metal in eV, and μ is the Fermi energy in eV. The dimensionless parameter y is defined as

$$y = \frac{\sqrt{e^3 F}}{\phi}. \quad [3.6]$$

If F is in V/cm and ϕ in V, $y = 3.79 \times 10^{-4} \frac{F^{\frac{1}{2}}}{\phi}$. Referring to Fig. 3.3, the electric field reduces the potential energy barrier which an electron in the tip experiences by an amount Fex . The electron's image charge reduces the barrier an additional $\frac{e^2}{4x}$. At the point where the potential $V(x)$ is a maximum, the image contribution is equal to $\sqrt{e^3 F}$. Thus y is the ratio of the image contribution at $V(x) = V_{max}$ and the work function ϕ . The other parameters, $t(y)$ and $v(y)$ are smoothly varying functions of y . Tables of these parameters can be found in the literature[47, 48].

The Fowler-Nordheim equation can be rewritten

$$\frac{j}{F^2} = a e^{-\frac{\alpha \phi^{\frac{3}{2}}}{F}} \quad [3.7]$$

with $a = \frac{1.54 \times 10^6}{\phi t^2(y)}$ and $\alpha = 6.83 \times 10^{-7} v(y)$. A plot of $\ln \frac{j}{F^2}$ vs. $\frac{1}{F}$ is therefore linear. Note that the current density j is also given by $\frac{I}{A}$ with I being the current and A the relevant surface area of the emitter.

It is customary to assume that the electric field is constant over the surface of the tip and linearly proportional to the applied voltage V . This means that

$$F = \beta V \quad [3.8]$$

where

$$\beta = \frac{1}{kr_{tip}}. \quad [3.9]$$

Here, k is a factor expressing the compression of the field by the presence of the tip shank. If we insert $k = 1$ into Eqn. 3.9 we get the familiar result for the electric field produced by a sphere held at a voltage V , $F = \frac{V}{r}$. Equation 3.7 can be re-written

$$\frac{I}{V^2} = A\beta a e^{-\frac{\alpha\phi^{\frac{3}{2}}}{\beta V}}. \quad [3.10]$$

Therefore, a plot of $\ln \frac{I}{V^2}$ vs. $\frac{1}{V}$ is also linear. This provides a means by which the field at the tip surface and the tip radius can be estimated. It is easy to show that the slope b of such a plot will be related to β by

$$\beta = -\frac{0.683\phi^{\frac{3}{2}}}{b}s(y) \quad [3.11]$$

where

$$s(y) = v(y) - \frac{y}{2} \frac{dv(y)}{dy} \quad [3.12]$$

and y is defined as above. The function $s(y)$ has been tabulated [47]. Thus by measuring the emitted current as a function of the applied voltage, the tip radius can be estimated. This is one of the most fundamental uses of the Fowler-Nordheim formula.

3.2 FIM Principles

3.2.1 Field Ionization

Field ionization is the most important physical process required to understand FIM, and is shown schematically in Fig. 3.6. In many respects it is very similar to field emission. A high positive voltage is applied to the tip. The potential barrier

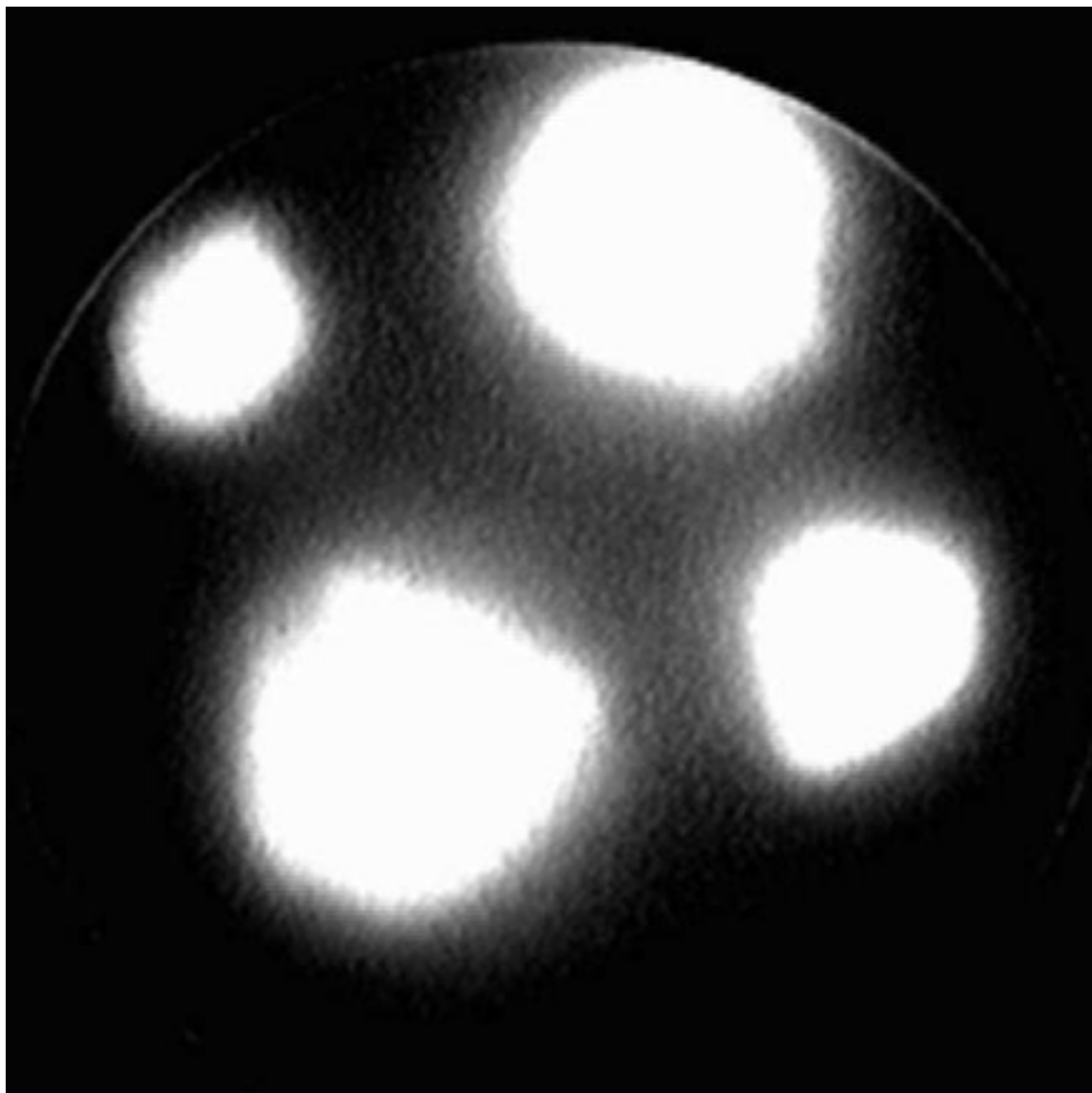


Figure 3.1 Field emission micrograph of a (110) oriented W tip. Note the 4-fold symmetry about the central (110) facet.

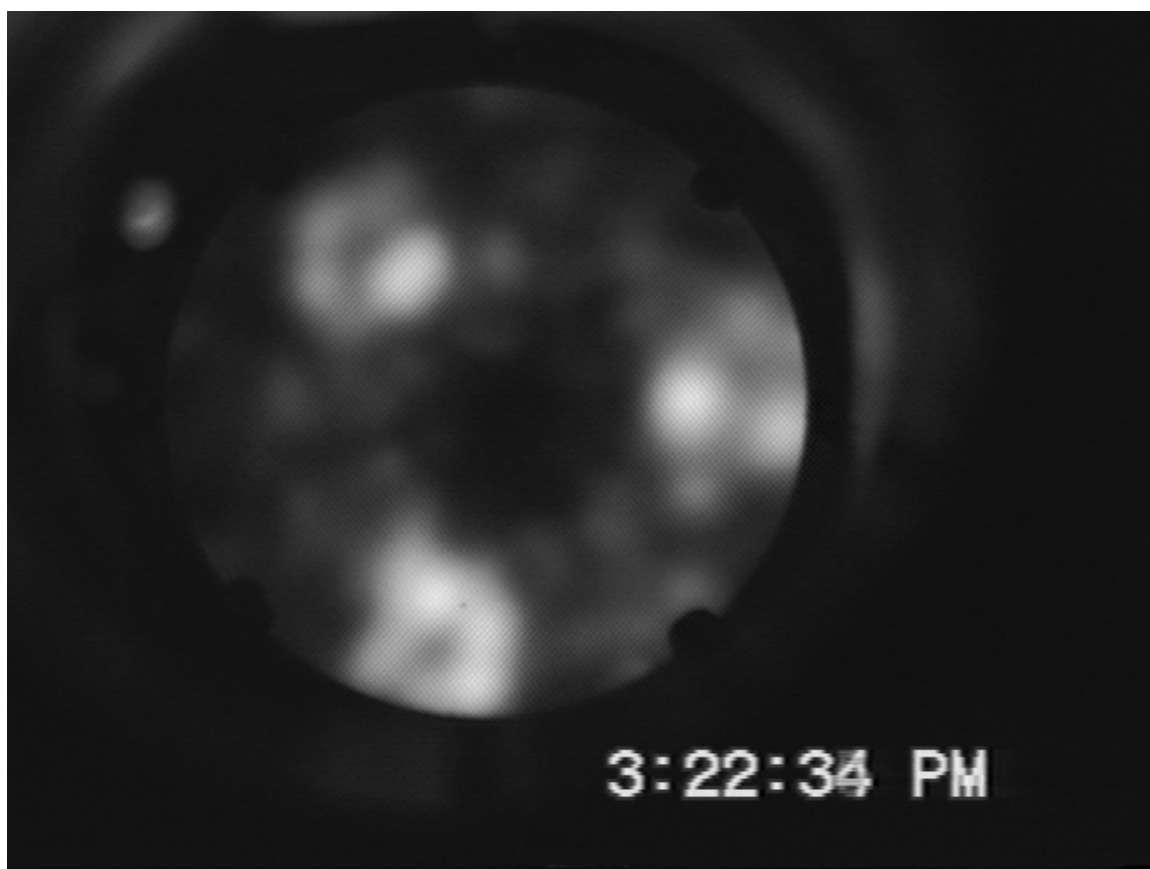


Figure 3.2 Field emission micrograph of a (111) oriented Pt tip. Note the 3-fold symmetry about the central (111) facet.

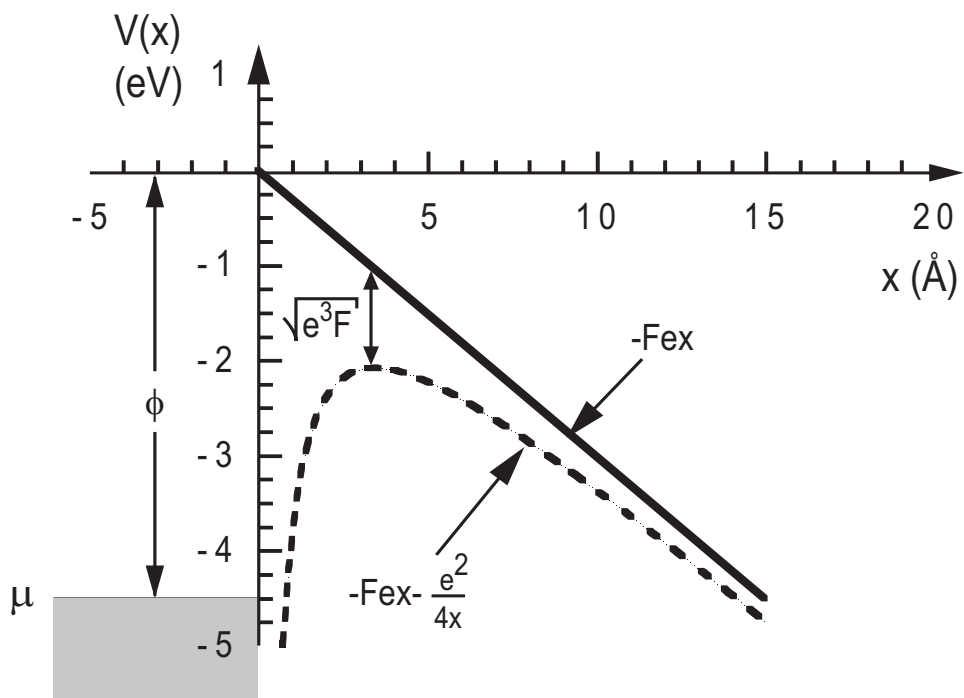


Figure 3.3 Potential barrier associated with field emission. The solid line represents the deformation of the barrier by the applied field, while the dashed line includes the reduction by the electron's image charge.

influencing the outermost electrons in the approaching gas atoms is essentially determined by the applied field. As a result, electrons tunnel from the gas atoms into the tip (see Fig. 3.5.)

Consider an approaching gas atom at a distance x_i from the surface of a metal with an electron at x . As the atom nears the tip in an applied electric field F , the potential barrier encountered by the electron is

$$V(x) = eFx - \frac{e^2}{|x_i - x|} + \frac{e^2}{x_i + x} - \frac{e^2}{4x}. \quad [3.13]$$

Taken term by term, this accounts for contributions from the applied field, the interaction of the electron with the ion, the interaction of the electron with the negative image of the ion, and the interaction of the electron with its own positive image charge.

The transmission coefficient for an electron with energy E can be calculated using Eqn. 3.13 and the WKB approximation for a one-dimensional potential barrier,

$$T[V(x), E] = \exp\left(-\frac{2}{\hbar} \int_{x_1}^{x_2} \{2m[V(x) - E]\}^{\frac{1}{2}} dx\right). \quad [3.14]$$

Here, x_1 and x_2 are the edges of the potential barrier at a given electron energy E , and m is the electron mass. This expression can be evaluated numerically. As the gas atom approaches nearer to the tip, $T[V(x), E]$ increases and reaches a maximum at a distance x_c . Beyond x_c the ground state of the atom falls below the Fermi level of the tip and tunneling is prohibited as a consequence of the Pauli exclusion principle.

At x_c electrons at the ground state of the atom must be raised to the Fermi level μ in order for tunneling to occur[26]. This requires that

$$eFx_c = I - \phi - \frac{e^2}{4x_c} + \frac{F^2(\alpha_a - \alpha_i)}{2} \quad [3.15]$$

with I being the atom's ionization potential, and α_a and α_i being the polarizabilities of the atom and the resulting ion, respectively. The last two terms are negligibly small, so

$$x_c \simeq \frac{I - \phi}{eF}. \quad [3.16]$$

For the case of H₂ (I = 15.4 eV) being used to image a tungsten surface ($\phi = 4.5\text{eV}$) at a field strength of 220 MV/cm, $x_c = 4.95 \text{ \AA}$.

A more useful form of the penetration coefficient can be found by approximating the potential barrier with an equilateral triangle of height $(I - 2\sqrt{e^3F})$ with a base of $\frac{(I-\phi)}{eF}$ [3]. For F in V/Å and I and ϕ in eV, this gives

$$T(x_c, E) = \exp\left\{-0.683 \frac{(I - \phi)}{F} \sqrt{I - 7.59F^{\frac{1}{2}}}\right\} \quad [3.17]$$

The mean lifetime of a gas atom before it is ionized can be found by multiplying the transmission probability T by the frequency ν with which the electron strikes the barrier,

$$\tau = (\nu T)^{-1} \quad [3.18]$$

For the above case of hydrogen being used to image a tungsten surface, $\nu = 4.1 \times 10^{16} \text{ s}^{-1}$ [3] and $\tau = 2 \times 10^{-14} \text{ s}$.

3.2.2 Performance of the FIM.

The major advantages of the FIM are its large magnification and high resolution. The magnification is typically $\sim 10^6$, and the resolution is limited to $\sim 1.5 \text{ \AA}$ at 0K [49], though resolutions on the order of 2-2.5 Å are more typical. The FIM can be idealized as a point-projection microscope with a magnification equal to the ratio of the tip-to-screen distance R and the tip radius r_{tip} . However, the field lines which the ions follow are compressed by a dimensionless factor ρ by the presence of the tip shank, so the magnification is given by

$$M = \frac{R}{\rho r_t}. \quad [3.19]$$

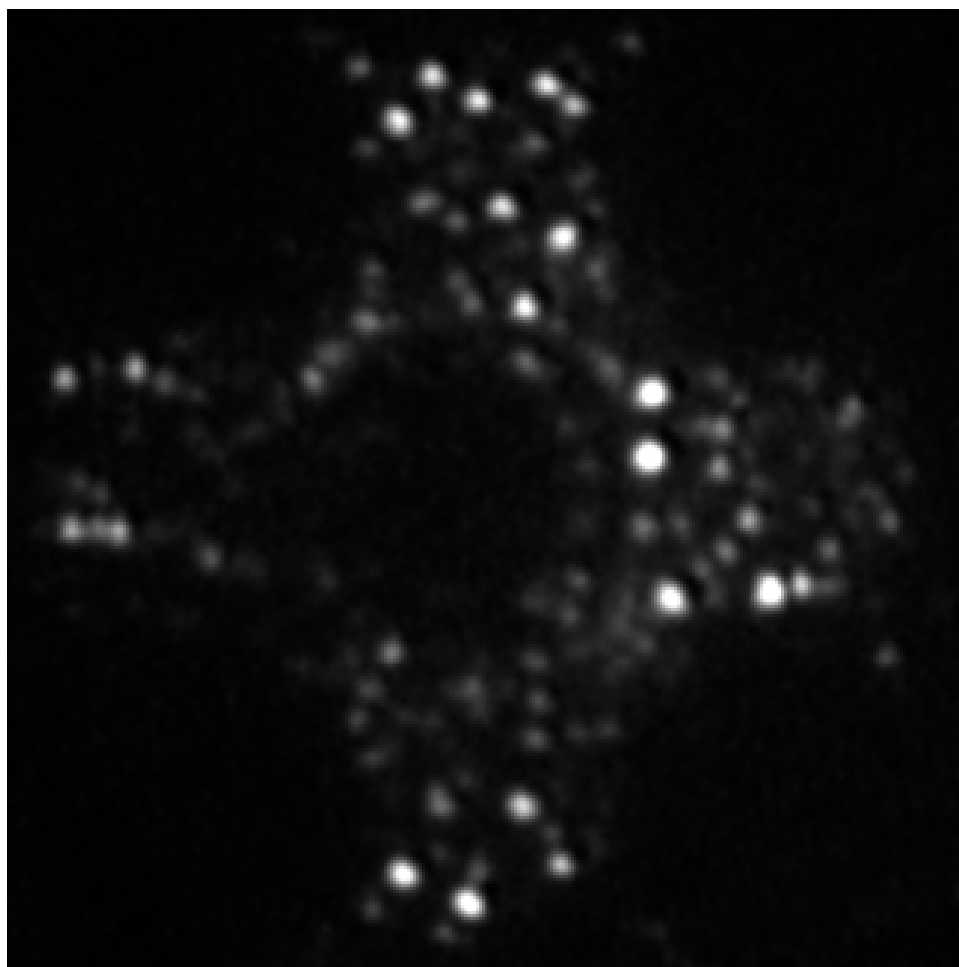


Figure 3.4 FIM image of a (100) oriented Pt/Ir tip. $V=10\text{kV}$, $T \simeq 100\text{K}$.

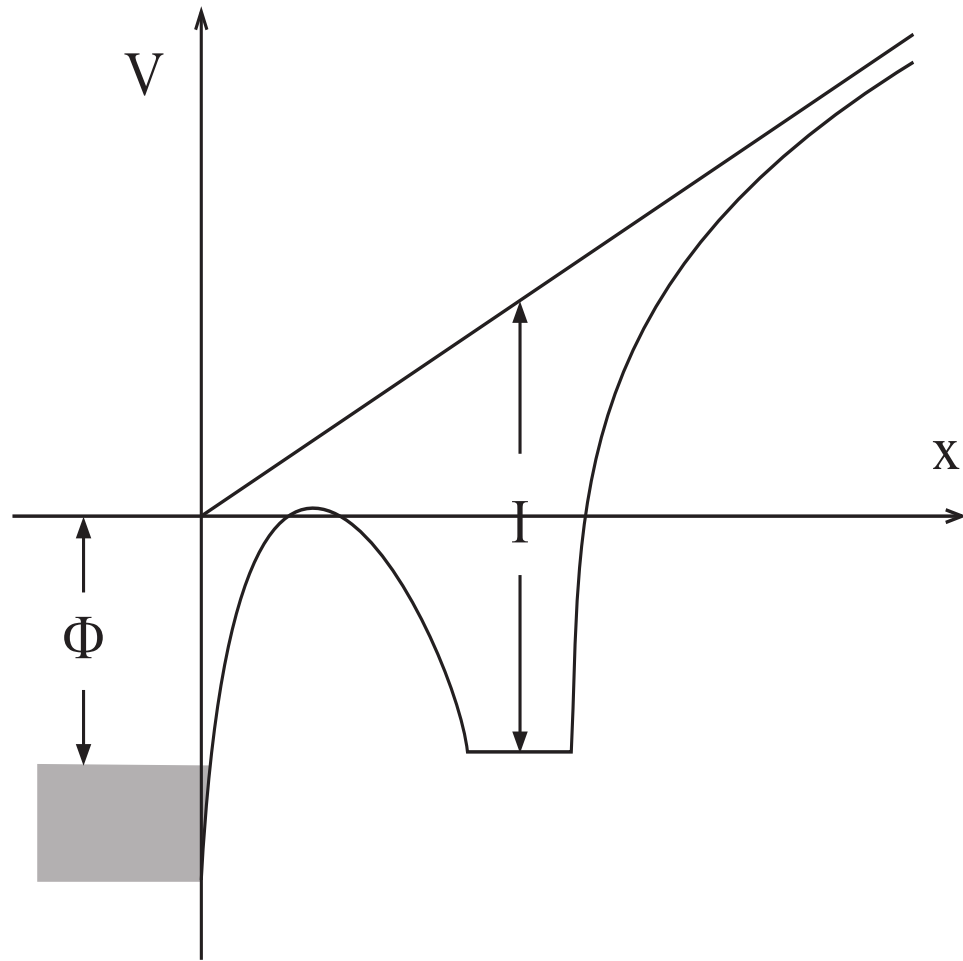


Figure 3.5 Potential energy diagram for an electron in a gas atom approaching a tip in a high electric field. I is the ionization energy for the gas atom and ϕ is the work function of the metal [3].

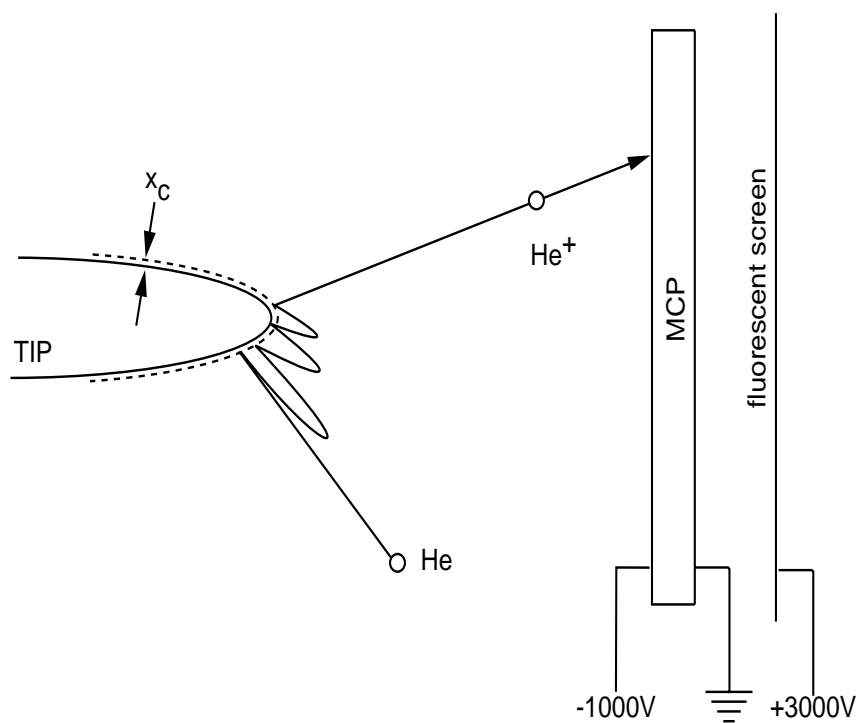


Figure 3.6 Image formation in FIM. An approaching gas atom strikes the tip and rebounds several times, becoming thermally accommodated with the tip. After it is ionized, it is accelerated to the imaging screen.

ρ can be calculated if the ion paths are known, but it is usually much simpler to merely measure ρ directly from the FIM. A value of 1.5 is typical for ρ [26].

When a cluster is placed on the end of a standard FIM tip, the magnification is increased as a result of the local enhancement of the electric field in the vicinity of the cluster. This increase in resolution was first calculated by Rose [50] and later treated by Castro [51]. For a cluster of radius r_c on a tip, the magnification is [51]

$$M' = 1.1M\sqrt{\frac{r_t}{r_c}} \quad [3.20]$$

where M is the magnification for the bare tip, given by Eqn. 3.19.

The generally accepted definition of resolution for the FIM does not follow the typical Rayleigh definition of resolution, or the minimum separation of two objects which are just discernible. Rather, it is defined as

$$\delta = \frac{D_{min}}{M} \quad [3.21]$$

where D_{min} is the diameter of the smallest image size of a discernible atom. Castilho and Kingham give the expression [52]

$$\delta = [\delta_o^2 + \frac{4\rho\hbar r_t \rho^{\frac{1}{2}}}{(2m\epsilon V_o)^{\frac{1}{2}}} + 16\kappa(\frac{\rho^2 r_t^2}{eV_o})\epsilon_T]^{\frac{1}{2}} \quad [3.22]$$

for the resolution. Broken down term-by-term, this shows that the resolution is the result of contributions of the ionization cross section (δ_o), the combined effect of the Heisenberg uncertainty in the ion momentum and the broadening of the ion beam by magnification, and the thermal energy of the atoms prior to ionization.

The thermal energy ϵ_T is given by [49]

$$\epsilon_T = \gamma k_b T, \quad [3.23]$$

where γ is the degree with which the atoms are thermally accommodated to the tip. It is a dimensionless constant between 0 and 1. While the mean life time of gas atoms in the vicinity of the tip is exceedingly short, most are not ionized when they first

Table 3.1 Best Image Fields for various image gases [3].

Image Gas	BIF (MV/cm)
He	440
Ne	375
H ₂	220
Ar	180

approach. These approaching atoms collide with the tip and perform a series of short hops on the surface of the tip until they are ionized. In doing so they come into thermal equilibrium with the tip.

A number of factors influence the quality of images formed in the FIM. For instance, if the applied field is too high, atoms will be ionized further away from the tip, and will not be as fully accommodated with the tip. This leads to a subsequent loss in resolution[24]. The best image field (BIF) is the electric field at which the optimal amount of image contrast is obtained. For a given geometry, this field will occur at a specific voltage, the best image voltage (BIV). Above the BIF, image contrast and picture quality decrease.

BIFs for various image gases have been measured and are generally well defined [3]. Assuming a BIF of 440 MV/cm for He, the values for other gases can be calculated by holding the transmission probability, Eqn. 3.17 constant. Table 3.2.2 summarizes the BIFs for various image gases.

3.2.3 Simulation of FIM images

Since the probability of an image gas atom in the FIM being ionized is exponentially dependent on the local electric field strength, the majority of the atoms which ionize gas atoms are those which reside on step-edges or so-called “kink sites”. This,

along with the fact that the FIM is essentially a point projection microscope greatly simplifies computer simulation of FIM micrographs.

The most common algorithm used to simulate FIM images is commonly known as the “thin shell method” [53, 7, 3, 30]. As is shown schematically in Fig. 3.7, a crystal lattice for a tip or cluster is first assumed. Next a thin shell is defined about the perimeter of this crystal lattice. Any atom whose center falls within this thin shell is considered to have contributed to the simulated image, and its position is projected onto a two-dimensional virtual screen.

Both the thickness of the shell and the projection point can be adjusted to fit the simulated images to experimental data [53, 54]. The projection point is typically chosen to be a point $2R$ behind the apex of the tip, where R is the radius of the tip. This corresponds to a stereographic projection, which most closely approximates experimental data [54]. Experimentally, the position of the projection point is related to the compression of the electric field.

Varying the thickness of the thin shell roughly corresponds to experimentally varying the applied electric field. As the shell thickness is increased, more atoms on the surface meet the thin shell criteria (see Fig. 3.8) just as more atoms are imaged as the electric field is increased. However, as the electric field is increased the resolution of the FIM is affected adversely, so this analogy only goes so far.

When matching a simulated image to experimental data, provisions must be made for rotating the initial crystal lattice. FIM tips made from BCC metals typically are oriented with the apex pointing in the (110) direction and those made from FCC materials are typically oriented with the apex along the (100) or (111) direction, but this is not always the case. Similarly, a cluster landed on the apex of a tip can in principle land in almost any orientation. The simulation program used in the current studies therefore allows the rotation of the lattice through any combination of standard Euler angles [55].

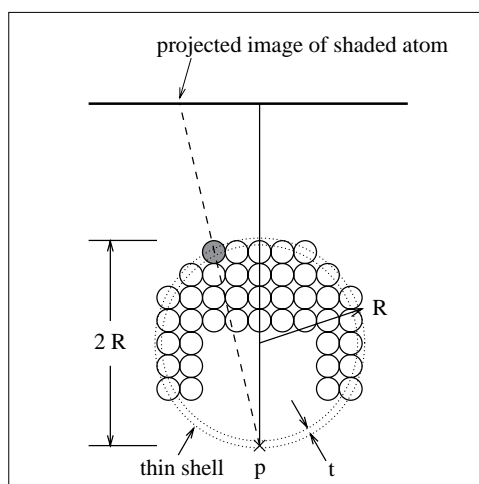


Figure 3.7 Schematic for thin shell simulations of FIM micrographs.

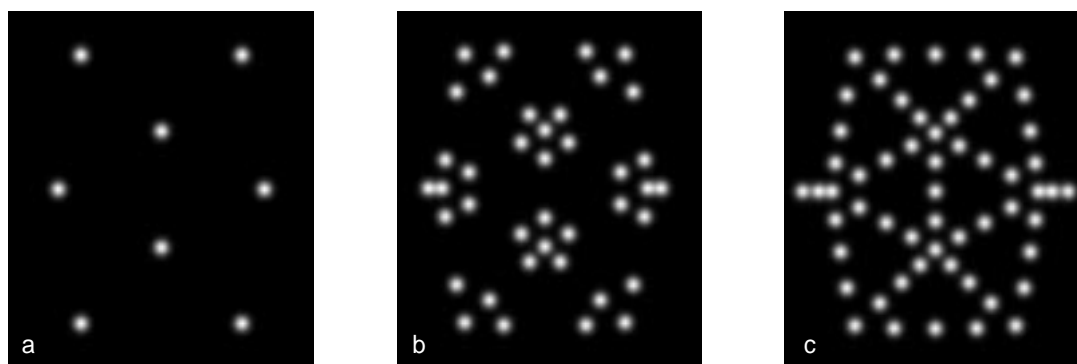


Figure 3.8 Illustration of the effect of varying the shell thickness on simulated images of a 309 atom icosahedral cluster, such as the one shown in Fig. 2.2b. a) $t = 0.75 \text{ \AA}$ b) $t = 1.00 \text{ \AA}$ c) $t = 1.50 \text{ \AA}$.

4. EXPERIMENTAL

4.1 Field-ion Microscope for cluster studies

A homebuilt field-ion microscope was used in these studies. The FIM (see Fig. 4.1) is located inside a custom designed UHV chamber pumped by a 220 l/s ion pump. The main chamber features four 6" ports, four 2.75" ports and top and bottom 8" ports. During imaging it can be isolated from the ion pump by means of an 8" gate valve.

In order to capture clusters on FIM tips, the tip must be placed in a cluster beam approximately 1/8" in diameter. To do this reliably, tips are mounted on a sample manipulator which has three degrees of translational and two degrees of rotational freedom. The sample mounting stage has three degrees of translational freedom and two degrees of rotational freedom, enabling us to precisely align the tip with the cluster beam.

Tips are mounted on modified electron gun filament holders as shown in Fig. 4.2(1). The filaments have been replaced with W support loops on to which the tips are spot welded. The filament holder plugs into two stainless steel sockets on the mounting stage, which greatly simplifies tip replacement. A Cu collar attached to the manipulator's LN₂ fixture (2) fits around the ceramic base of the tip holder so that the tip can be cooled.

The stock sample holder on the XYZ-R manipulator (3) was modified to allow use of the high voltages necessary in the FIM. A 5mm thick macor block (4) was added to the top of the stage for high voltage insulation. The two stainless steel sockets are mounted in this to accept the tip assembly. Cu electrical leads (5) are also attached to these.

The cluster beam passes into the main chamber via one of the 2.75" ports, after passing through a space which is differentially pumped with a turbo pump. A Cu septum with a capillary tube separates the FIM and the differentially pumped space. This protects the UHV chamber from contaminants in the medium vacuum of the MECS, keeping the pressure in the FIM to around 10^{-9} Torr during cluster capture. During normal operation, a gate valve is used to separate the two chambers.

Captured clusters can be imaged on either a small fluorescent screen or a channel plate with an integral fluorescent screen. During cluster capture the cluster beam passes through a small probe hole in the fluorescent screen. The tip is aligned with the cluster beam and pointed at the screen so that the progress of the cluster capture can be monitored.

The channel plate is used for imaging clusters in both field emission and field-ion mode. FIM typically produces an image using a total ion current of only about 10^{-12} A, so some method of intensifying the inherently weak images is necessary so that traditional video imaging techniques can be used. Modifications to the FIM such as a dynamic gas supply to increase the ion current density [3] intensify images by a factor of 50 or so, but this is still so dim that traditional video techniques are not feasible. Electrostatic shielding of the tip to increase the ion energy can intensify the image by a factor of ~ 100 [56, 3], but this happens at the expense of requiring a higher applied voltage so the technique is only feasible for small tip radii. Channel plates have come into favor because of their high gain (a factor of $\sim 10^4$) and ease of use. A channel plate is essentially a collection or bundle of ceramic tubes arranged in a disk shape. A voltage of about 1000V is applied between the front and back surfaces, and any impinging electrons or ions cause a cascade of secondary electrons to travel along the tube to a phosphor screen. A schematic of one tube from a channel plate is shown in Fig. 4.3.

During the latter stages of the current study an electron energy analyzer built by Omicron Instruments was added to the chamber. This is built on a cylindrical sector analyzer (CSA) design and is ultimately capable of 2meV resolution. This gives us

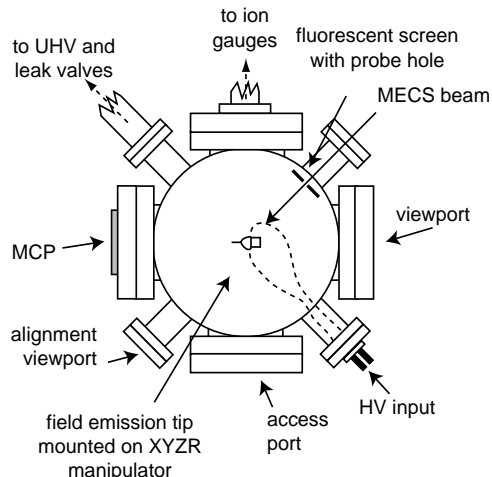


Figure 4.1 FIM designed for the study of supported nanoclusters.

the unique ability to study both the structural and electrical properties of the same cluster.

4.2 Field Emission Microscope for Carbon Nanotube Studies

A separate field emission microscope was used for the studies of carbon nanotubes. This was done to allow the uninterrupted study of Au clusters. The separate chamber also provided a test chamber for perfecting techniques for using Pt tips in the Au cluster studies.

Overall, the UHV chamber surrounding the FEM is much smaller than the cluster FIM, allowing for quick turn-around times following tip changes. The tip to screen distance in the FEM is only 2.5 cm, as compared to about 14 cm in the cluster FIM.

The microscope used in the carbon nanotube studies is essentially a “bare bones” all metal field emission microscope (FEM). A commercially obtained phosphor screen mounted off of a $3\frac{3}{8}$ ” viewport allows for the recording of field emission patterns. Tips are mounted using the same modular design as in the larger FIM. They are placed at the end of a simple sample manipulator which allows for three degrees of freedom.

Fowler-Nordheim data was taken using a 286 PC as shown schematically in Fig. 4.4. During data acquisition, the tip is held at ground and a positive bias is applied

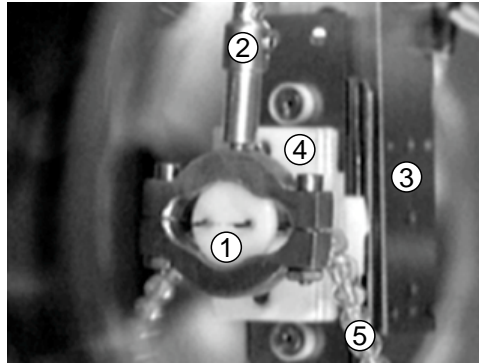


Figure 4.2 Close up of tip assembly. 1) Tip, 2) Cooling braid, 3) Tip manipulator, 4) Macor insulating stage, 5) High voltage electrical leads.

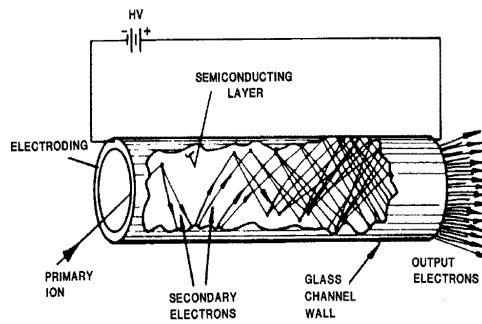


Figure 4.3 A single element of a channel plate. A potential of 1000V is applied between the front and back surfaces of the plate, causing a cascade of electrons when any impinging electrons or ions strike it [7].

to the screen. Because of this, a higher voltage must be applied to achieve the same electric field at the tip than would be necessary if the screen were grounded and the tip held at a negative voltage. This also affects the field compression factor (β in Eqn. 3.8) calculated from this data, as the two scenarios are not equal but opposites of each other.

4.3 Preparation of W and Pt Field-ion Emitters

The heart of the field-ion microscope is its tip. Typically this is a very sharp needle made of W or some other material, with an end radius on the order of 1000\AA . Tips are normally prepared by electrochemical etching [3, 30, 57] but other techniques can be employed for other, more exotic materials [7].

W, Pt, and Pt/Ir tips were used in the course of this study. Tip radii were typically $\sim 1000\text{\AA}$ as determined by a Fowler-Nordheim plot. This corresponds to a BIF of 10-12 kV in the FIM. In each case the tips were mounted on modified electron gun filaments. The filaments were removed and replaced with support loops made of the respective materials. The tip holders then fit into sockets in the sample manipulator, allowing the tips to be changed quickly and easily.

Tip preparation and conditioning can take place both outside and inside the UHV chamber which houses the FIM. In what follows, various techniques for preparing W and Pt tips will be described.

4.3.1 Etching

After being spot welded to the support loop, W tips are etched at about 3 VAC in a 1 N solution of NaOH in H_2O . Inspection of the tips in an optical microscope usually reveals that the resulting tips have an end radius of a few thousand angstroms. To further sharpen the tips they are etched as follows [58, 57, 3]: A drop of a 1 normal solution of NaOH in 50% H_2O and 50% glycerin is placed in a W loop, and then the tip is placed in the solution and etched at a few millivolts. The process is viewed through a stereoscopic microscope. Using this technique, often known as

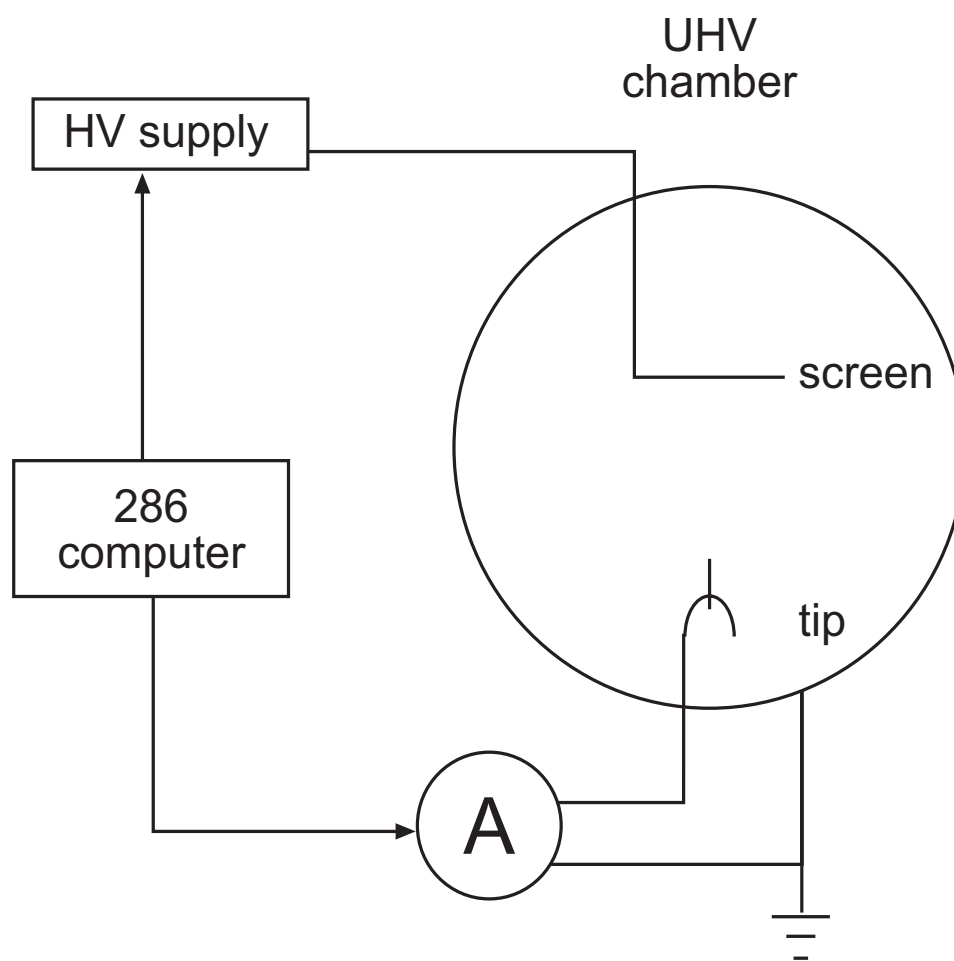


Figure 4.4 Experimental setup for taking Fowler-Nordheim data.

“zone electropolishing”, tips with an end radius of a few hundred angstroms can be made. With practice, the process can be used predictably, and tips with a desired end radius can be produced routinely.

Most researchers etch Pt tips in a solution of KCN or molten salts [3, 30]. Because of the obvious health risks and the general difficulty of these techniques, other techniques have been developed. [59] The Pt tips used in this study were etched at about 4-5 VAC in a solution of CaCl_2 , H_2O , and acetone. The resulting tips were about 500-1000 Å in radius.

Pt/Ir alloy tips were used after it became apparent that Pt tips were not robust enough to withstand the frequent pulse cleaning often required during cluster capture. Wire with a 0.1mm diameter made from a 90% Pt / 10% Ir alloy was used to make these tips. The addition of Ir makes etching more difficult, so a solution of 14g CaCl_2 in 80ml H_2O was used. A second step similar to that used to make W tips was used to further sharpen the tips. A drop of the etching solution was suspended in a Pt/Ir wire loop and used for zone electropolishing at 30VAC.

4.3.2 Secondary preparation

When a tip is etched, the final separation of the bulk wire and what remains on the support loop is usually due to gravity. The weight of the portion of wire below the surface of the etching solution causes the wire to break in the region that has been etched. The surface is therefore a jagged fracture surface rather than an ideal, atomically smooth surface.

Because of this, the tip must be smoothed out before it is usable as a field emitter and as a substrate for cluster experiments. The easiest way to do this is by thermally annealing the tip. The tip is mounted on a thin support loop so that when a current is passed through the loop, the loop and the tip are heated. This is also an effective way of cleaning contaminants from the surface of the tip.

During this phase of tip preparation, the end radius of the tip will increase. This is desirable for our experiments, since for cluster experiments the radius of the tip should be much greater than the size of the clusters being studied.

After thermally annealing the tip, field evaporation can be used to prepare an atomically smooth surface. Field evaporation is the removal of lattice atoms from the tip using a high electric field. In principle field evaporation is little different from field ionization, and in fact field ionization can be modeled by the charge-exchange model of field evaporation [26, 3, 30], yielding results consistent with the standard picture of field ionization. The removal of adsorbed atoms and lattice atoms from the tip are theoretically identical, however the term “field evaporation” is usually reserved to describe removal of lattice atoms. The removal of adsorbed atoms from the surface is referred to as “field desorption”.

For the case of desorption of a metal atom from its own lattice (i.e. field evaporation) $Q(F)$, the activation energy for field evaporation of an ne charged ion, can be written, [7]

$$Q_n(F) = \Lambda + \frac{1}{2} \left(\frac{n^3 e^3 F}{\pi \epsilon_0} \right) + \frac{1}{2} (\alpha_a - \alpha_i) F^2. \quad [4.1]$$

Here Λ is binding energy of a neutral atom to the substrate, F is the applied electric field, and α_a and α_i are the polarizabilities of the atom and ion, respectively.

In practice, field evaporation as a method of preparing an atomically smooth tip is a self-regulating process. Atoms at kink sites and step edges cause an enhancement in the local electric field, and will be removed if the local field is high enough. This continues until a smooth surface with a relatively uniform electric field is obtained.

4.3.3 Other techniques

Sometimes it is necessary to further “tweak” the tip in order to make it suitable for a specific study. Tips can be blunted and sharpened *in situ* if necessary, within reason. This was necessary in the course of the present studies because it is desirable to have a tip substrate which has a radius of curvature which is much larger than

the radius of a typical cluster. On the other hand, a tip which is too blunt must be sharpened so that the electric field required for imaging is within the abilities of the equipment.

Blunting a tip is relatively straightforward. Passing a DC current of about 4 to 5 A is enough to heat the tip to near its melting point. As the tip is heated, some blunting occurs. Applying the current for longer periods of time will blunt the tip more, and carefully monitoring the voltage required for field emission makes it possible to blunt the tip to a desired radius.

Sharpening a tip *in situ* is somewhat less straightforward. The usual method is by ion sputtering. [60, 61] If a partial pressure of heavy gas atoms such as Ar or Ne is admitted into the chamber and the tip operated in field emission mode, electrons striking gas atoms will ionize the gas atoms. The resulting ions will then be accelerated towards the tip. This bombardment will gradually erode the tip, sharpening it. By keeping the field emission current approximately constant, the radius of the tip can be monitored and the tip can be sharpened to a desired radius.

4.4 Cluster Production

Cluster production is typically a growth process where constituent atoms are brought together one by one, as opposed to a destructive process where particles are made by subdividing a bulk material. At some point the process is stopped and the clusters are separated from each other, either by chemical or spatial means. Thus the particles are kept from growing to sizes where bulk effects dominate the properties of the material.

There are many strategies taken to produce nanometer size clusters. For example, the clusters can be self-assembled by evaporation onto a substrate such as graphite or MgO [16, 31]. While this method is capable of producing uniform clusters, there is considerable interaction between the clusters and the substrate. The substrate invariably plays a role in the synthesis process and affects the final structure. Clusters

produced in this method are difficult to harvest, and the experimental exploitation of these clusters is limited.

Colloidal chemistry techniques have also been used to produce nanometer size metal clusters. Metal salts are typically used; they are reduced in an aqueous solution to form clusters [62]. The resulting cluster colloid is a useful medium for storage of clusters until they are needed. This technique, however often results in a very broad size distribution in the clusters formed.

In our studies, clusters are formed by self-assembly in the gas phase [16, 8], in a multiple-expansion cluster source (MECS) as shown in Fig. 4.5 [8]. These clusters are easily collected for use in a variety of experiments. The Purdue MECS is located in the Potter Engineering building and was developed by Prof. R. P. Andres in the School of Chemical Engineering. A schematic is shown in Fig. 4.5. In what follows a brief description of its operation is given.

The Purdue MECS is capable of both one- and two-component clusters with a uniform size distribution [8, 9]. Single component clusters were included in this study so special attention will be given here to their production.

Cluster production begins in the oven region, where the component metal is contained in a C crucible. This is heated to evaporate atoms from the surface of the metal, and the resulting gas is superheated so that only monomers and dimers of the metal exist in this region. This superheated gas then undergoes a sonic expansion into a region of lower pressure where it is mixed with a quench gas. The species of gas used for the quench affects the final structure and size of the clusters [8]. Typically He is used for production of Au clusters.

The gas/metal mixture encounters a high temperature gradient when it is expanded into the quench region. This causes the mixture to become supersaturated, and individual metal atoms begin to clump together to form clusters. By controlling the pressure in this region, the time that the gas/metal mixture resides in this region is controlled. This in turn affects the ultimate size of the clusters produced.

Table 4.1 Summary of cluster annealing studies using HRTEM [4].

Annealing Temperature	Cluster Diameter	Structure
none	all	MTPs with fcc domains 1-2 nm in diameter
1200K	> 8 nm	icosahedra and decahedra
	< 8 nm	single fcc crystals
> 1400K	all	single fcc crystals

After the quench, or growth region, the clusters pass through a capillary tube into an annealing region which consists of an Al_2O_3 tube which passes through an annular oven [8]. In this region clusters can be raised above their melting temperatures [8]. In the case of Au clusters this results in a reconstruction of the clusters, resulting in a single crystal motif.

After the annealing furnace, the clusters can be collected for use in a variety of experiments. Means are provided by which they can be collected in a colloidal suspension using the metal cluster colloid reactor (MCCR) [62] or on transmission electron microscope (TEM) grids [8]. A representative TEM image of MECS clusters deposited on a Cu grid is shown in Fig. 4.6. By viewing the clusters in the TEM an estimation of the cluster size distribution can be made an example of which is shown in Fig. 4.7, with the data in Table 4.4. The structural properties of clusters can also be ascertained. Systematic studies of the effects of cluster annealing on cluster structure were undertaken [4]. In these studies, clusters were annealed at different temperatures and captured on TEM grids. A summary of the results is given in Table 4.4 [4].

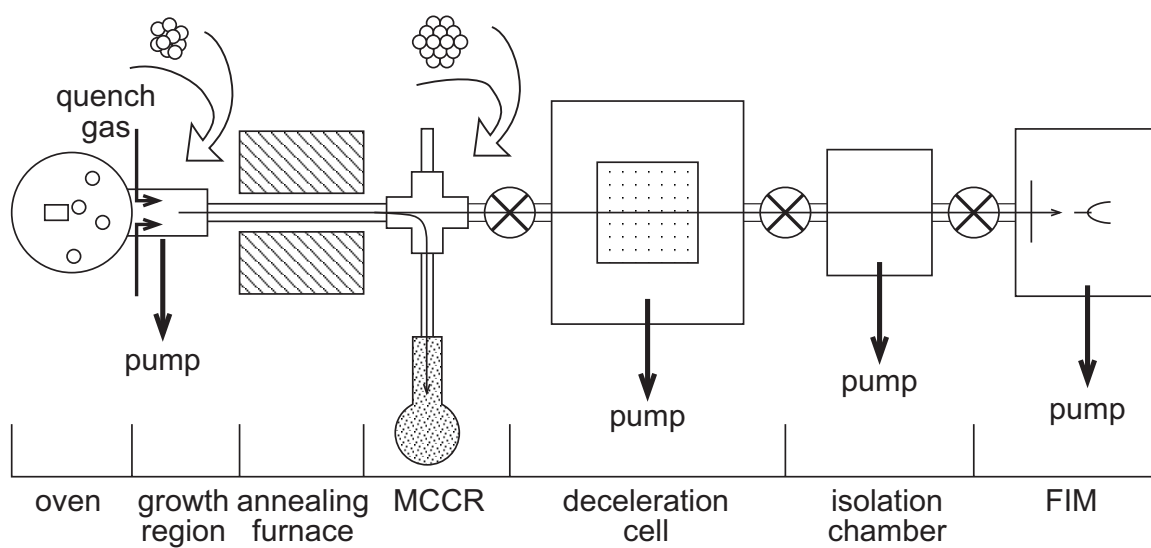


Figure 4.5 Schematic of the Purdue Multiple Expansion Cluster Source (MECS) [8, 9].

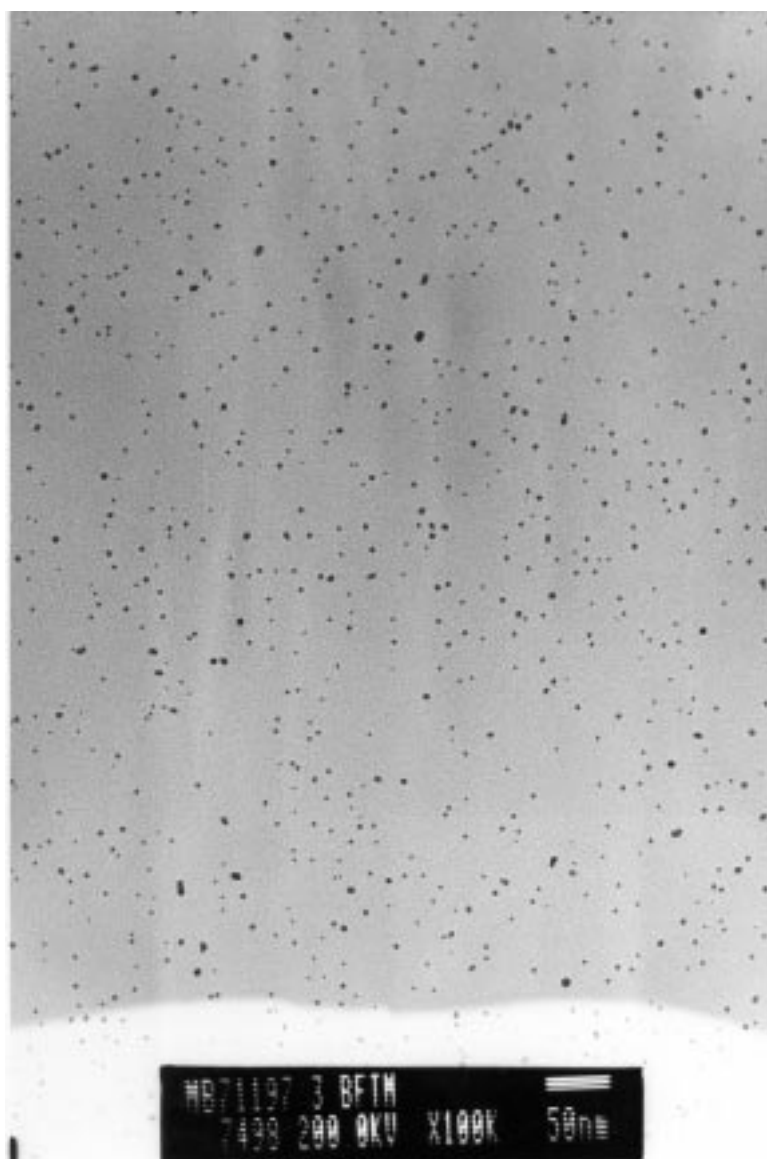


Figure 4.6 TEM of MECS clusters deposited on a Cu TEM grid.

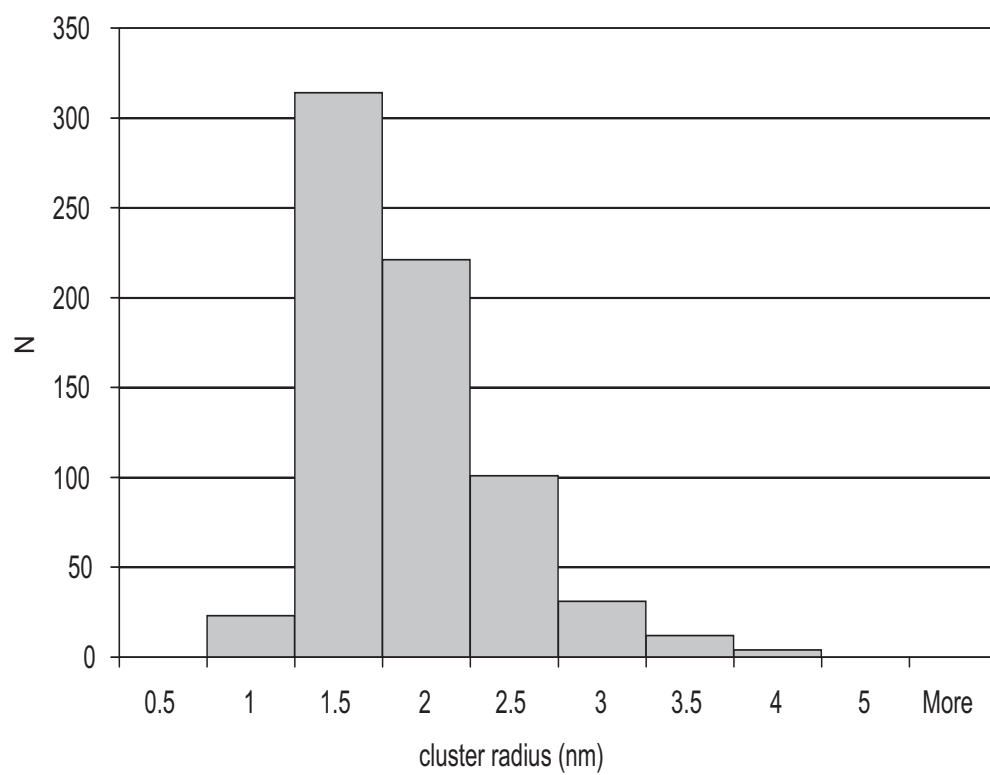


Figure 4.7 Histogram plot of the cluster size distribution in Fig. 4.6.

Table 4.2 Size distribution data for the plot in Fig. 4.7.

<i>radius (nm)</i>	<i>count</i>
0.5	0
1.0	23
1.5	314
2.0	221
2.5	101
3.0	31
3.5	12
4.0	4
5.0	0
More	0

5. EXPERIMENTAL RESULTS

5.1 Depositing Clusters on Field Emission Tips

5.1.1 Cluster Capture

Individual Au clusters were deposited on a suitably etched Pt tip mounted on a support loop and carefully aligned with the 2 mm diameter cluster beam using a theodolite as shown in Fig. 5.1. The tip is pointed toward a fluorescent screen and biased to promote field emission of electrons. Before deposition, the characteristic field emission pattern of the tip material is observed at some voltage V_o which is typically about 2000 V.

The applied voltage is then lowered to $\frac{2}{3}V_o$, causing the field emission pattern from the tip to disappear. The deposition of a cluster is then signaled by the appearance of a bright spot on the screen, indicating the presence of an object with a high radius of curvature on the FIM tip. Assuming good alignment of the cluster beam with the tip, a tip of radius 100 nm, and the cluster flux of 7×10^{10} clusters/cm²s, the mean time of arrival between clusters is estimated to be 7 s if no cluster deceleration is used. This is in good agreement with the 5 - 10 s required to capture an un-decelerated cluster on the tip. When clusters are decelerated from their initial speed of 500-1700 m/s to a final mean velocity of ~ 4 m/s to avoid impact damage, the capture time required increases significantly.

As soon as localized electron emission is observed at a reduced voltage, the voltage is reduced to about $\frac{1}{2}V_o$ and the cluster beam is blocked off by closing a gate valve. Electron emission from the cluster can then be imaged by rotating the tip toward a multi-channel plate equipped with an integral fluorescent screen. Electron emission

studies have sometimes been conducted over a period of a few days with no evidence of cluster diffusion or wetting.

After cleaning, $\sim 2 \times 10^{-5}$ Torr of Ar imaging gas is admitted into the chamber so that the cluster can be imaged in the FIM mode. The tip/cluster is cooled using a liquid nitrogen cold finger to about 100K. Ar was chosen as an imaging gas based upon its relatively low best image field (BIF). The initial FIM images are sometimes found to be uneven and occasionally, the entire cluster will desorb during this initial imaging procedure. The uneven nature of the image is thought to be due to the field desorption of weakly bound Au atoms, probably from the cluster facets. After a few minutes however, a stable image of the edge and corner atoms from the cluster usually become evident.

During the course of these studies, Au clusters were captured and successfully imaged on W, Pt, and Pt/Ir tips. The resulting FIM images were matched with cluster structures and the orientation of the cluster on the tip substrate was determined. These results are presented below.

5.1.2 Cluster Deceleration

MD calculations have shown that clusters deposited onto a substrate at high kinetic energies can suffer damage upon impact [63, 64]. In particular, Cheng and Landman considered Cu_{147} clusters incident on a (111) oriented Cu surface. They found that significant damage (cluster deformation and mixing of surface and cluster atoms) occurred for impacts where the kinetic energy was greater than ~ 1 eV/atom, or for cluster speeds of greater than 2 km/s. Betz and Husinsky studied Al and Pb clusters impinging on Cu surfaces, with similar results [64]. Minimal damage occurred for collisions with an average kinetic energy of < 1 eV/atom.

In the Purdue MECS, the clusters are swept along with the He carrier gas. After passing through the annealing furnace, the cluster/gas mixture passes into the main chamber through a 1mm diameter capillary tube. Inside the capillary, we make the assumption that the cluster speed is equal to that of the carrier gas as it passes

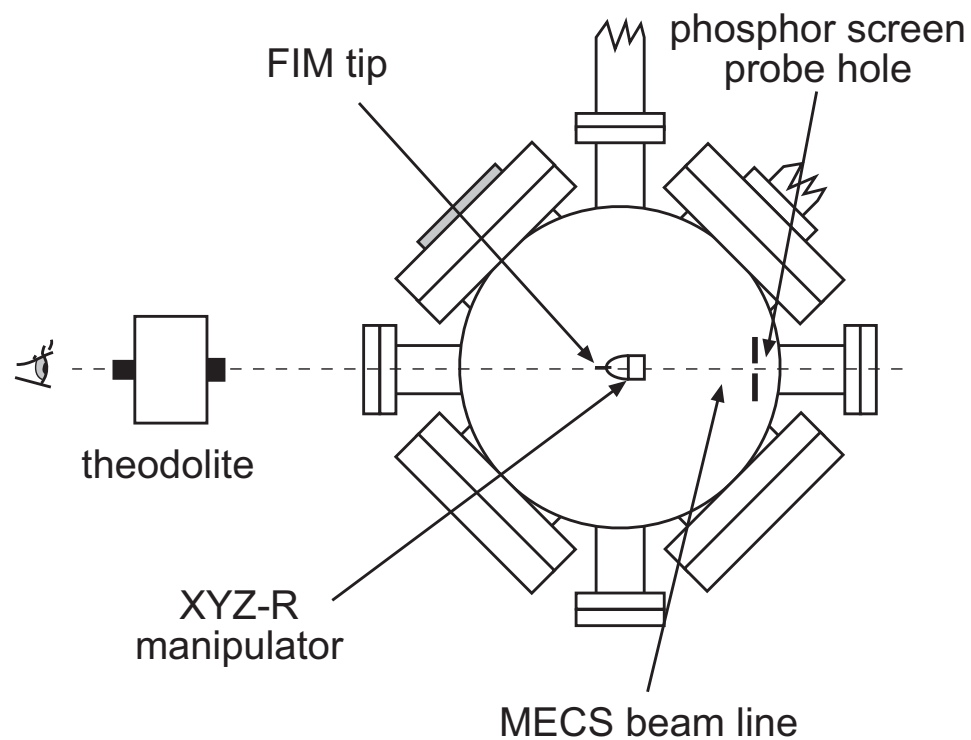


Figure 5.1 Schematic for alignment of the tip with the MECS cluster beam. The beam passes into the FIM and through the probe hole in the phosphor screen and strikes the alignment viewport at a point which has been marked for reference. A theodolite is used to align the FIM tip in the beam line. Afterwards the FIM tip is rotated 180° to point towards the phosphor screen.

through the capillary nozzle between the main oven and the vacuum chamber. This is given by [65]

$$v_{p,i} = \frac{1}{2} \sqrt{\frac{\gamma k T_g}{m_g}} \quad [5.1]$$

with $\gamma = 1.67$ being the specific heat ratio of the He carrier gas. T_g and m_g are respectively the temperature and mass of the carrier gas, while k is the Boltzmann constant. For He this gives a cluster speed of about 510 m/s, or a kinetic energy of ~ 0.26 eV/atom for Au clusters.

After passing through the capillary tube, the carrier gas undergoes a second expansion as it enters the main vacuum chamber. Clusters will be further accelerated in this expansion via collisions with gas molecules. The cluster speed will then be equal to or less than the speed of gas molecules in this region. Considering clusters acceleration in the supersonic free jet between the capillary exit of the annealing furnace and the entrance of the deceleration chamber yields an upper limit on the cluster velocity prior to entering the deceleration box. This speed will be [65]

$$v_{p,i} \leq \sqrt{\frac{5kT}{m_g}}. \quad [5.2]$$

If we assume complete acceleration, the clusters will have a velocity of ~ 1770 m/s, corresponding to an energy of ~ 3.2 eV/atom for Au clusters. This is sufficient energy for significant damage upon impacting the tip. Clusters must therefore be decelerated prior to deposition.

For deceleration, clusters pass through a box which is held at a higher pressure than the rest of the main MECS chamber by leaking in Ar gas. The distance required to stop a particle with diameter d_p and density ρ_p traveling through a stagnant gas is [66]

$$X_{max} = \left(\frac{2}{8 + \pi} \right) \frac{d_p \rho_p v_{p,i}}{n_g m_g} \left(\frac{\pi m_g}{2kT_g} \right)^{\frac{1}{2}}. \quad [5.3]$$

Note that here, n_g denotes the gas density. This equation assumes that the gas particles have a Boltzmann distribution of thermal velocities. X_{max} is determined by monitoring the cluster flux with a film thickness monitor (FTM). The pressure in the deceleration cell is adjusted until the FTM signal drops to 50 % of the FTM signal prior to deceleration. When this occurs, X_{max} is equal to the length of the deceleration cell, ~ 61 cm in the current configuration.

As can be seen in Eqn. 5.3, smaller clusters are decelerated more than larger clusters. The smallest clusters tend to be stopped completely, while larger clusters pass through with a final mean thermal velocity

$$v_{p,f} = \sqrt{\frac{8kT}{\pi m_c}}. \quad [5.4]$$

Here, m_c is the mass of the cluster. For 2 nm spherical Au cluster, $v_{p,f} = 4.0$ m/s, corresponding to an impact kinetic energy of 1.6×10^{-5} eV/atom.

Returning to Eqn. 5.3, the expected mean particle size can be calculated given the 50 % stopping pressure and the length of the deceleration box. A summary of a series of experiments studying the mean size of decelerated clusters is given in Table 5.1.2. The results suggest that the initial velocity of clusters before they enter the deceleration box is in between the values predicted by Eqns. 5.1 and 5.2. This is reasonable, since it is not likely that there will be a sufficient number of collisions to accelerate the clusters to the maximum velocity given by Eq. 5.2.

If an initial size distribution of clusters passes through the deceleration box, the smaller clusters will be nearly completely filtered out, while larger clusters will pass through. The largest clusters will pass through with a mean velocity

$$v = v_0 \left(1 - \frac{l}{X_{max,p}} \right). \quad [5.5]$$

$X_{max,p}$ is the X_{max} for the particle in question, while l is the length of the deceleration box.

This filtering will result in a change in the size distribution. This was studied by sampling the cluster beam both before and after the deceleration box, capturing

clusters on TEM grids. The cluster size distributions on the resulting TEMs were analyzed. A representative comparison of the size distributions from the front (before the deceleration box) and rear (after deceleration) FTM positions are shown in Fig. 5.2. The rear FTM data was sampled from the cluster beam directly before passing into the FIM and therefore is representative of the size distribution of clusters present in FIM experiments.

5.2 Au Clusters on W Substrate

W substrates were first chosen for our studies. There are many reasons for this. It is a relatively easy tip material to work with. W tips are very robust and can be cleaned repeatedly by passing a high (>5 A) current through the support loop. Castro [67] and Lin [68] also used W tips with success in their studies of small Au clusters.

It was initially unclear as to whether or not clusters deposited on W tips would desorb due to the high electric fields encountered in FIM. The electric field required to desorb single Au atoms from a W substrate is only 260 MV/cm [43]. Since the majority of studies dealing with single atom diffusion are performed using He (BIF = 440 MV/cm) as an imaging gas, few studies of diffusion of Au on W have been performed [31]. As previously mentioned in Sec. 2.2.3, Ar was chosen as an image gas because of its relatively low best image field (BIF).

During the course of this study approximately 30 annealed clusters were successfully deposited for imaging on W tips during 14 runs. Of these, three yielded FIM data. One is shown in Fig. 5.4. Yet another was able to be identified as a truncated octahedron after integrating the images obtained as discussed in Sec. 5.5.2, below. Several more (50-100) were discarded for various reasons: immediate wetting, landing too far from the apex of the tip, or landing too near to other clusters. This was done by flash cleaning of the tip as mentioned above.

Clusters captured on W tips were often seen to wet the surface shortly after landing. The wetting rate seemed to be related to surface contamination. Qualitatively,

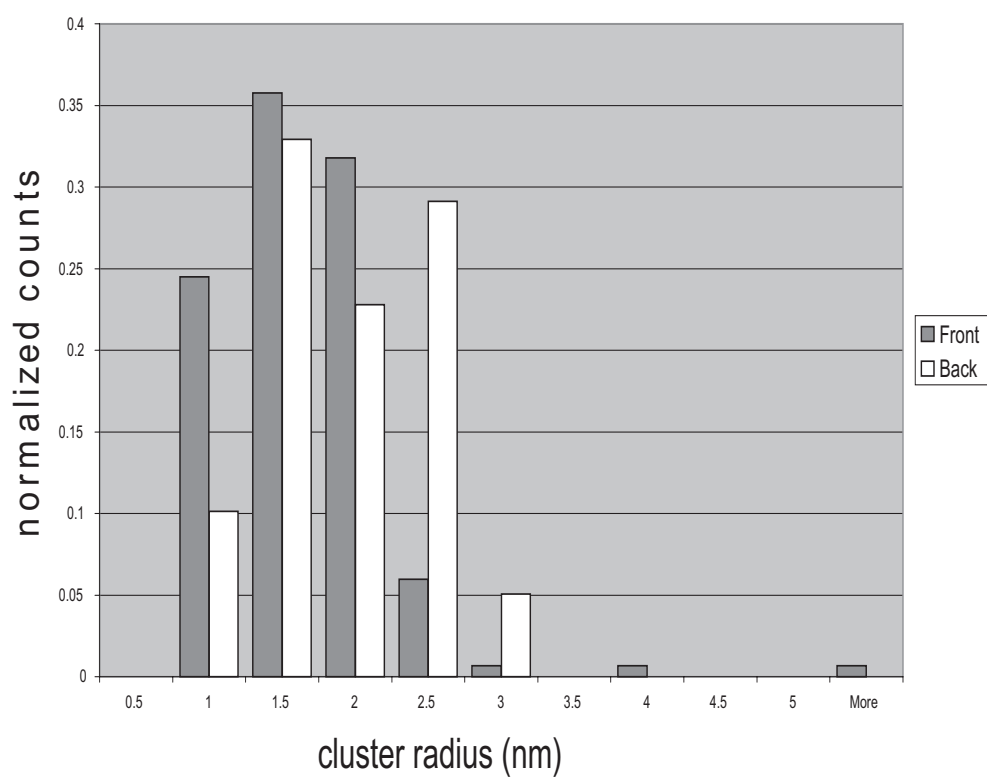


Figure 5.2 Comparison of the cluster size distribution before (front) and after (back) deceleration. Note that deceleration causes the mean size to shift upwards.

Table 5.1 Results of cluster deceleration experiments. For the expected mean particle diameters, d_p assumes no acceleration downstream of the capillary exit of the annealing furnace. In column 3 we assume an initial particle velocity $v_{p,i} = 510$ m/s given by Eqn. 5.1. The next column, d_{p2} assumes complete acceleration in the free jet downstream of the capillary exit, with $v_{p,i} = 1766$ m/s, from Eqn. 5.2 above. The experimental size distributions in the final two columns suggest that the actual initial cluster velocity is located between these two values.

Experiment ID	$P_{50\%}$ (mTorr)	$d_p(nm)$ $v_{p,o} = 510$ m/s	$d_{p2}(nm)$ $v_{p,o} = 1766$ m/s	d_{exp} (nm)	σ (nm)
e2997	41	6.02	1.74	3.36	1.04
f1097	38	5.58	1.61	2.78	0.64
f1397	33	4.85	1.40	3.37	1.12
f1997	33	4.85	1.40	3.60	1.08
g1197	40	5.88	1.70	3.29	1.04

clusters which were captured shortly after pulse cleaning were more likely to wet the surface than clusters captured several minutes afterward. Similarly, the wetting rate decreased as the time after cleaning increased. This seems to indicate that the interaction forces between a clean W surface and Au clusters is extremely strong. As the surface becomes contaminated, the interaction becomes weaker.

Interestingly, the clusters seemed to preferentially avoid certain areas of the tip. Clusters were seldom seen to land on the (110) oriented areas of the tip, and landed on the rougher, less densely packed regions instead. Whether the clusters actually did not land on the (110) faces or simply migrated from them too quickly to be seen is unknown. Clusters which did land on the (110) faces often wet the surface.

These observations are reminiscent of studies of Au migration on W by other authors [43, 69, 45]. Jones observed that Au evaporated onto a W tip was repelled from the (110) regions of the tip, which are the most densely packed and have the highest surface free energy. This continued until a critical coverage was reached, and the Au subsequently “invaded” the (110) regions.

The FIM images obtained were initially found to be uneven and occasionally, the entire cluster would desorb during this initial imaging procedure. The uneven nature of the image is thought to be due to the field desorption of weakly bound Au atoms, probably from the cluster facets. After a few minutes however, stable images of the edge and corner atoms from the cluster usually became evident. The image would remain stable for a period of 30 sec to a few minutes, then deteriorate as more and more atoms were removed from the cluster via field evaporation. In the cases where imaging was continued until the entire tip surface was visible, the last remaining atoms from the cluster remained until an electric field of $\sim 260\text{MV/cm}$ was applied. Even in cases where the entire cluster was removed during the initial stages of imaging, a return to field emission mode would reveal areas of enhanced electron emission where the cluster had been, presumably from a decrease in the work function due to Au atoms adsorbed on the W surface.

A representative field emission image from a Au cluster deposited onto a W tip is shown in Fig. 5.3. This cluster was hard landed and later imaged during the process of determining a lower limit on the electric field (and thus the applied voltage) required to desorb it from the tip. Sequentially higher positive biases with respect to the imaging channel plate were applied. This cluster remained on the tip even after an applied voltage of approximately 10 kV, near the BIV for the tip it was captured on. This indicates a very strong interaction force between the cluster and the tip.

A FIM image of the same cluster is shown in Fig. 5.4. The hexagonal symmetry apparent in the image clearly identifies this cluster as a member of the TO family. Comparisons to simulated images identify this cluster as being based on a 201 atom core, with a few extra atoms on the faces.

A comparison between the experimental image and the best simulation is shown in Fig. 5.5. The two show good agreement. The hexagonal face on the right side of the image appears to be more compressed in the X-direction in the experimental image than in the simulated image; this can be explained by the fact that the cluster landed far from the apex of the tip, which will affect the electric field lines. The simulations do not account for the position of the cluster on the tip, and so will not predict such effects.

5.3 Au Clusters on Pt Substrate

While images resulting from imaging Au clusters on W tips were promising, problems remained. Clusters often wet the W surface shortly after capture. Those that did not wet were often completely removed from the tip by the high electric field necessary for imaging.

Pt tips were used in an effort to more fully understand the interactions between the tip and clusters. Pt has been more widely used than W in the FIM community as a tip material in studying single atom diffusion of Au atoms [31]. It is however a much more difficult tip material to work with than W. Initial results with making and characterizing Pt tips was discouraging; it was very easy to blow out the tip end

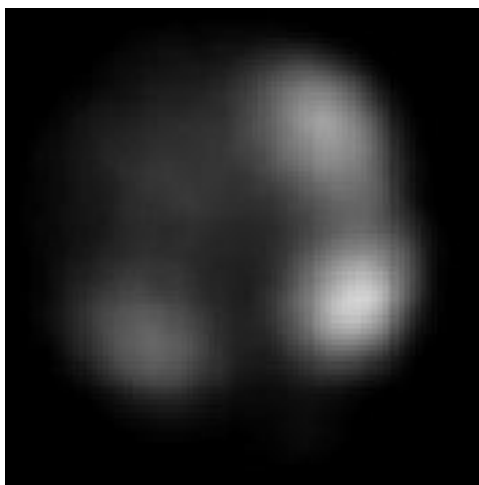


Figure 5.3 Field emission image of a ~ 2 nm Au cluster deposited on a W tip. This cluster has been “cleaned” by successively applying higher positive biases with respect to the imaging channel plate.

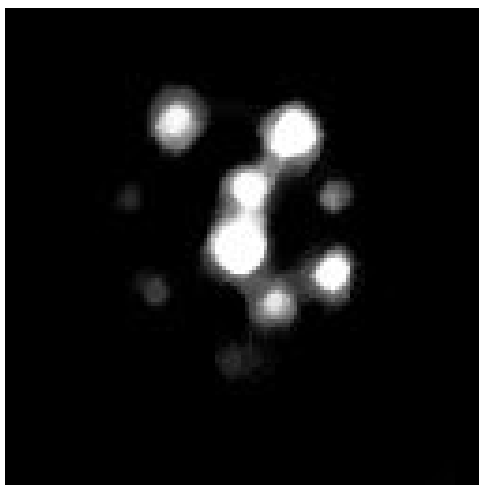


Figure 5.4 FIM of a ~ 2 nm Au cluster deposited on a W tip. The cluster was held at a temperature of 100K. Ar was used as an imaging gas.

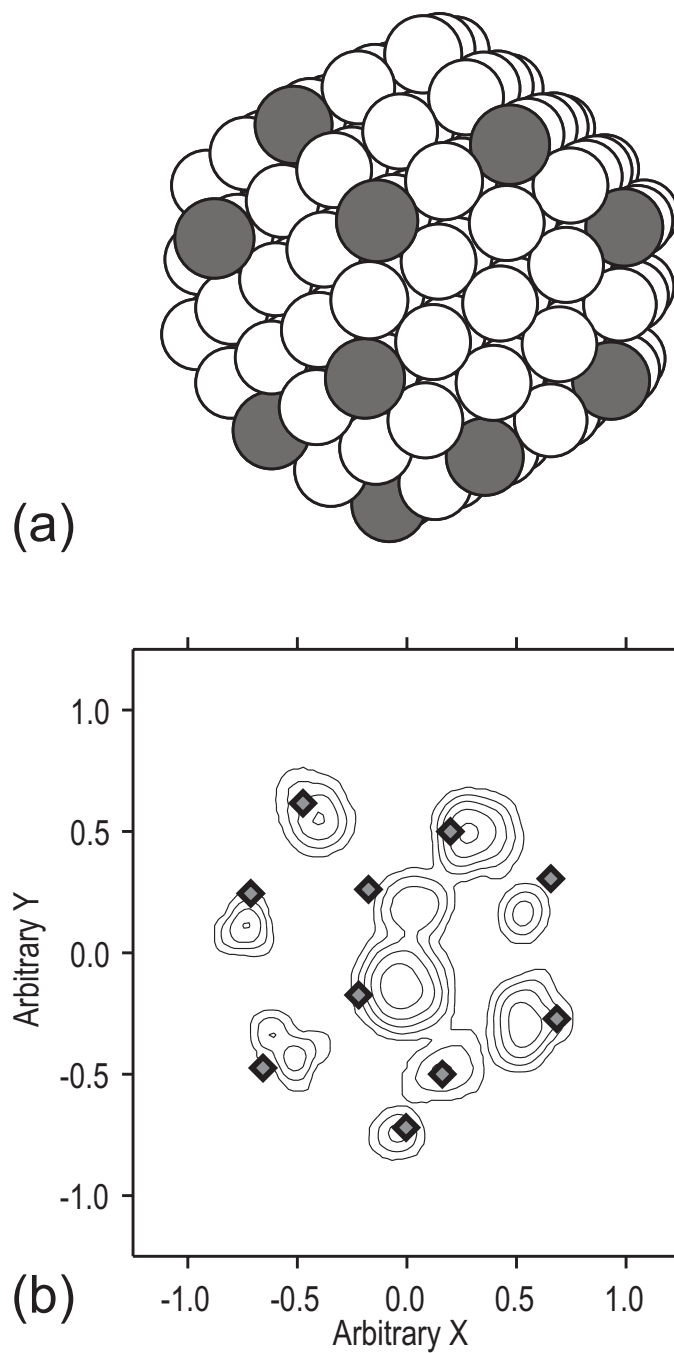


Figure 5.5 (a) A 202 atom cluster shown in the orientation which best fits the experimental image in Fig. 5.4. The shaded atoms represent the atoms imaged in the experiment. (b) Comparison of a simulated FIM image of a 202 atom cluster to the experimental image in Fig. 5.4.

during pulse cleaning. Two tips were lost in this manner during the initial phase of using Pt tips, before any cluster capture attempts were made.

Finally, a good Pt tip was made. This Pt tip used had an end radius of $\sim 570\text{\AA}$ as determined by a Fowler-Nordheim plot. It was oriented in the (111) orientation, as shown in Fig. 3.2. The BIV for this tip was $\sim 10\text{kV}$.

This tip was used during three runs, capturing a total of four clusters. The tip was blown out during a fourth run. Initial field emission observations of clusters captured on this tip were encouraging. The clusters were not seen to wet as they did on W tips. While the FIM images did not always yield enough data to match a structure and orientation to the imaged cluster, three of the clusters captured on Pt remained on the tip long enough to at least be partially imaged. A representative image is shown in Fig. 5.6.

Systematic examination of simulated FIM images quickly revealed that the cluster imaged in Fig. 5.6 was based on a 38-atom TO structure. The best orientation of the 38 atom cluster that agrees with experiment is shown in Fig. 5.7 (a). The resulting comparison between the simulated FIM image (squares) and the experimental image (represented as an intensity contour plot) is given in 5.7(b). To optimize the agreement, an additional atom was added to the 38 atom core cluster. The atoms contributing to the final image are all found to be corner atoms and are shaded in Fig. 5.7(a).

The resulting simulated image shows excellent agreement with the experimental image. Discrepancies between the experimental and simulated images are minor and can be attributed to the position of the cluster on the tip. Choice of the projection point used in the simulations may have also been a factor, since a true stereoscopic projection was assumed for the simulated images. In reality this is only an approximation for FIM images, and a more accurate simulation would require a more precise knowledge of the electric fields inside the UHV chamber.

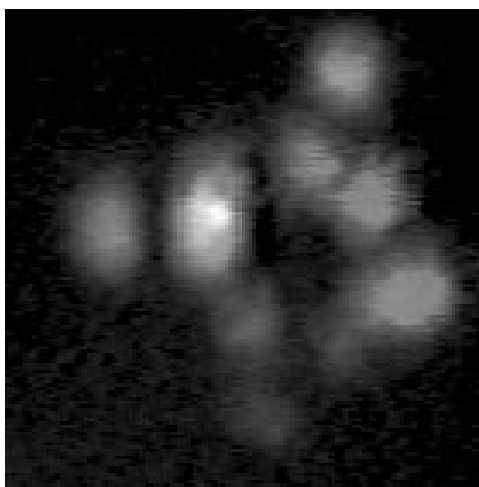


Figure 5.6 A field-ion image from a ~ 1 nm Au cluster, annealed in flight to a temperature of 1800 K, and soft landed on a Pt field emission tip. The approximate temperature of the tip and cluster is 100 K.

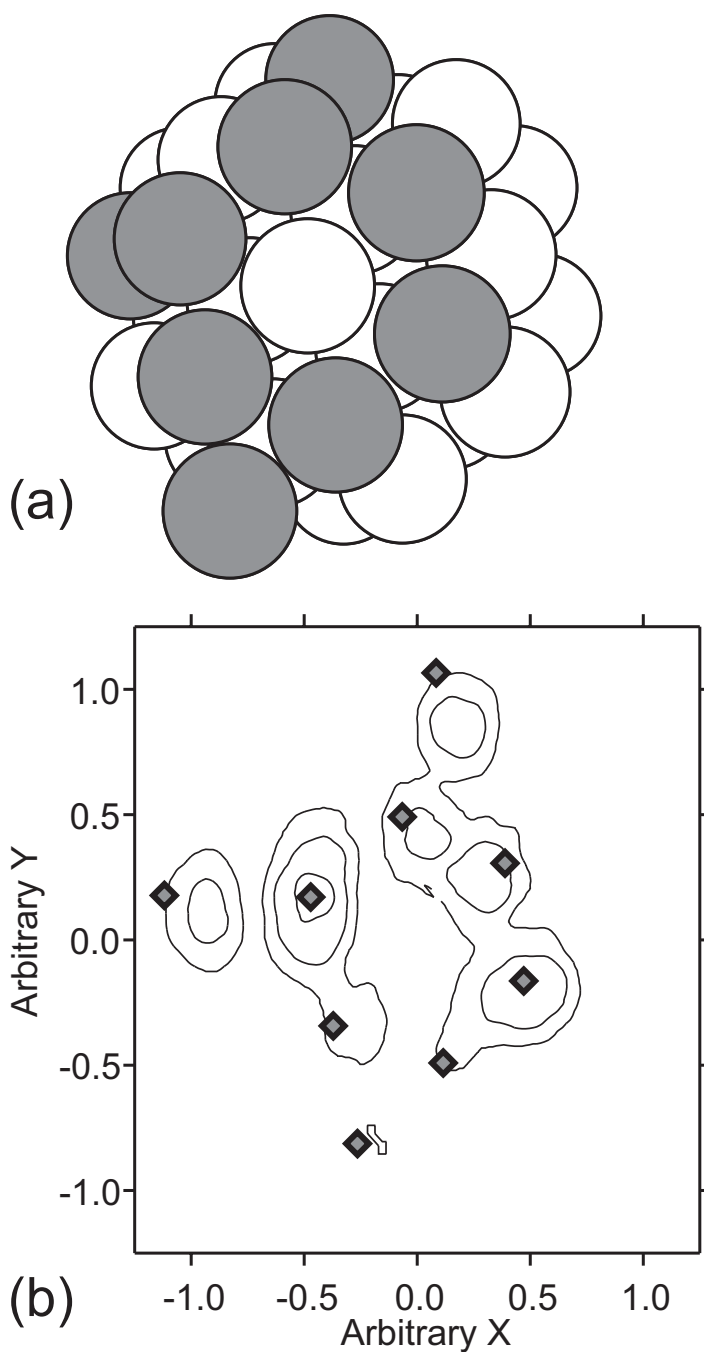


Figure 5.7 (a) The 39 atom cluster shown in the orientation that best fits the experimental FIM image. The shaded atoms represent those imaged in the experiment. (b) Simulated FIM micrograph (squares) of a 39 atom TO Au cluster which has been rotated to an orientation approximating that of the cluster imaged in Fig. 5.6. The contour plot shows the intensity of the recorded FIM image.

5.4 Au Clusters on Pt/Ir Substrate

While good results were obtained using Pt tips as supports for nanometer size Au clusters, in practice they are fragile and frequently needed replacement. Pt/Ir tips are often used in STM as a more robust alternative to Pt tips, and this was the original reason for switching to Pt/Ir tips as supports for Au clusters. Tips made from both 80% Pt/20% Ir and 90% Pt/10% Ir were used.

Pt/Ir tips were found to be much more robust than tips made from pure Pt. While they will not withstand the temperatures normally used to pulse clean W tips, they can be repeatedly pulse cleaned at lower temperatures. Like Pt, and in contrast to W, the orientation of the tip is unpredictable. Some tips were (111) oriented while the majority were (100) oriented. A field emission pattern from a (100) oriented Pt/Ir tip made from 90% Pt/10% Ir is shown in Fig. 5.8. A FIM image from this same tip is shown in Fig. 3.4.

During four successful capture sessions, five clusters were captured on Pt/Ir tips. Four yielded FIM data, though the final run was cut short due to a high voltage arc, destroying the tip. Partial wetting was observed for only one cluster, which was captured <20 s after cleaning the tip.

Unannealed Au clusters were deposited on Pt/Ir tips. Previous studies by Castro [70, 24] have shown that these are expected to be multiply twinned particles. Simulations of FIM images from icosahedral clusters [71] show that images from icosahedral clusters should be significantly different from images from TO clusters. Other multiply twinned particles, such as decahedra, should yield images similar to icosahedral particles.

An example of an Ar image from an unannealed cluster deposited on a Pt/Ir tip is shown in Fig. 5.9. This cluster landed near one of the off-apex (100) regions of the tip. It was possible to image this cluster at 4.8 kV, much lower than the BIV of ~ 10.5 kV for the bare tip. This confirms that the object being imaged has a radius of curvature much smaller than that of the tip. As the voltage was slowly increased, the



Figure 5.8 Field emission image of a Pt/Ir tip oriented in the 100 direction.

four atoms imaged here dramatically increased in brightness and their image spots were badly smeared. This suggests that they lie on corners of the cluster, since the electric field there would have a high local enhancement.

Close inspection of images taken at higher voltages revealed additional atoms, imaged more dimly than the four most prominent atoms. This can be seen in Fig. 5.10. Comparison of these images to simulations show a similarity. A proposed configuration that is close to experimental results is shown in Fig. 5.11. The simulated image shows fair agreement with the experimental image.

The discrepancies between the experimental images shown in Figs. 5.9 and 5.10, and the proposed structure shown in 5.11 can be attributed to deformation of the cluster by the substrate or to deviations of the cluster from a “true” icosahedron or decahedron. Unlike single crystal TO clusters which have been annealed, unannealed clusters appear “as formed”. There can be significant asymmetries present in the cluster, and there may be unequal numbers of atoms on edges of each face. Previous studies of unannealed clusters [70, 24] can be interpreted in this way. An example of such a cluster structure is shown in Fig. 5.12.

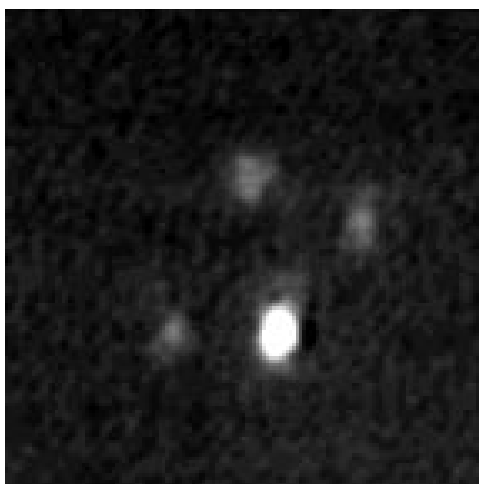


Figure 5.9 Field-ion image of an unannealed Au cluster. $V=4800\text{V}$, $T \simeq 100\text{ K}$.

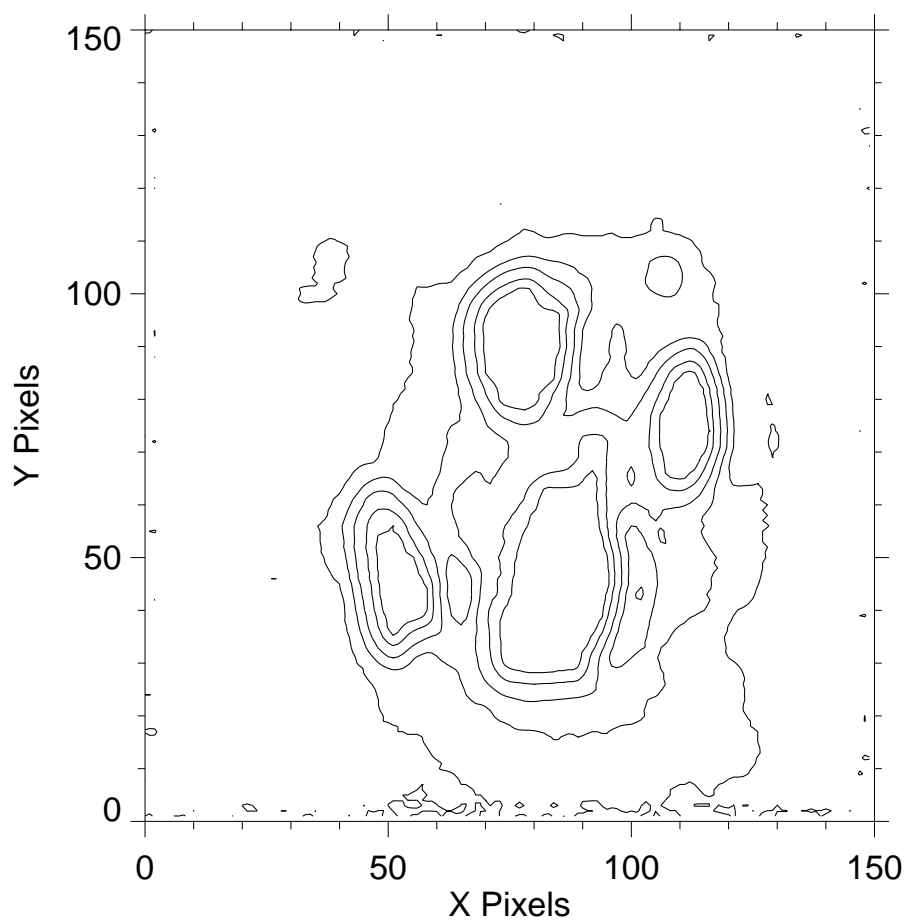


Figure 5.10 Contour plot of a field-ion image of an unannealed Au cluster, enhanced to show dimly imaged atoms. $V \simeq 5300$ V, $T \simeq 100$ K.

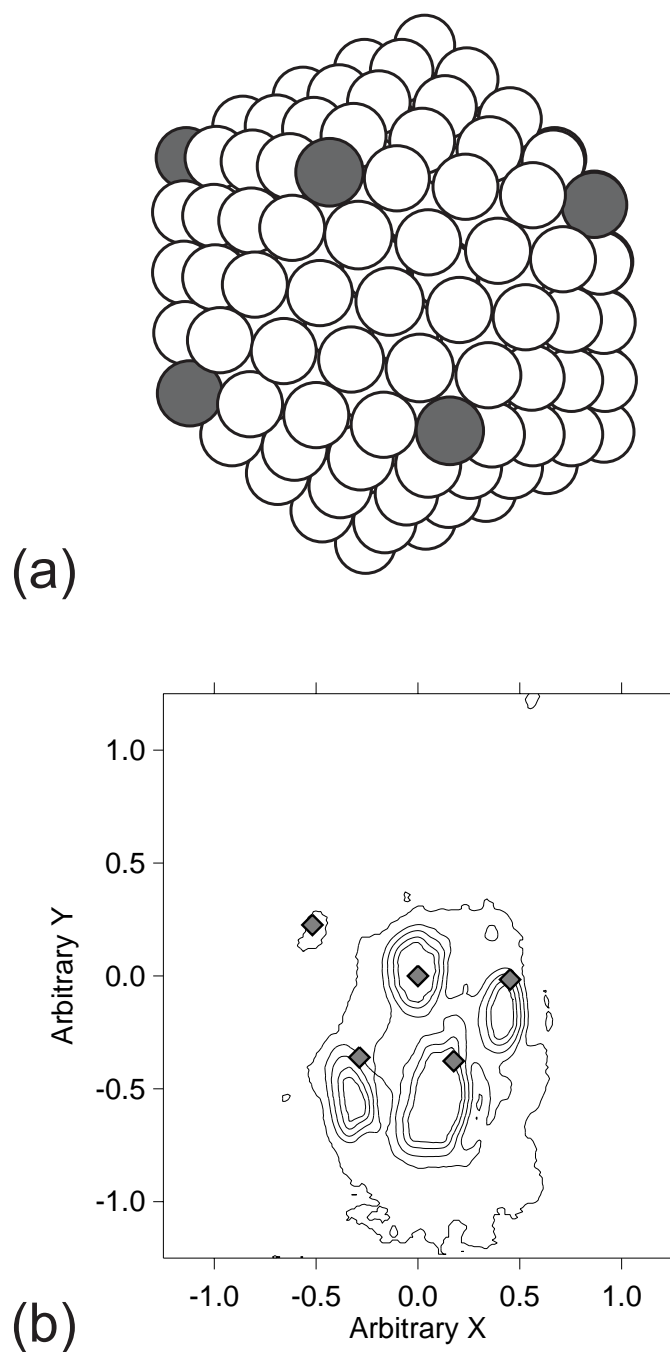


Figure 5.11 (a) Proposed icosahedral structure which is close to that which produced Fig. 5.9. The shaded atoms are those which are imaged in Fig. 5.10. (b) Comparison of simulated image from the structure in (a) to the experimental image. The two show fair agreement. Discrepancies suggest that the cluster is either deformed by the substrate or a structure other than a “perfect” icosahedron.

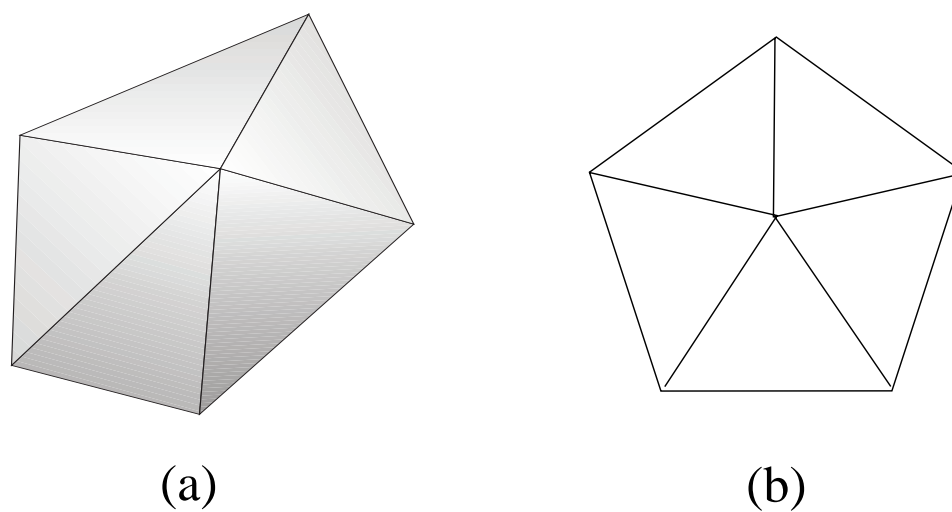


Figure 5.12 (a) Proposed multiply twinned structure for an unannealed Au cluster which is closer to the experimental data which produced Fig. 5.9. Comparing this to the “ideal” decahedron in (b), note that the edges of the structure in (a) are of unequal lengths.

5.5 Observed Physical Characteristics of Clusters

5.5.1 Structure

As a whole annealed clusters which were deposited on W and Pt FIM tips were identified as TO clusters, an observation which is corroborated by previous TEM [4] and AFM [21] studies of clusters produced in the Purdue MECS. Unannealed clusters in the same size range were seen to be MTPs in the FIM micrographs, also agreeing with previous studies [4, 24]. While we have observed clusters which we have tentatively identified as TO+ clusters, no M-Dh clusters have been identified in the current study.

The absence of the energetically favorable [22] M-Dh structures can be better understood if one considers the total energy of the particles rather than the excess energy Y which is traditionally used to characterize energetic favorability of cluster structures, as discussed above in Sec. 2.1. The total energy $E = \epsilon n$, where ϵ is the average energy per atom in the cluster. Inserting this into Eqn. 2.4 and rearranging,

$$E = Y + \epsilon_b N. \quad [5.6]$$

For ~ 200 atom clusters, $\epsilon_b = 3.93\text{eV}$, $\frac{Y}{N^{\frac{2}{3}}} = 1.675\text{eV}$ for a M-Dh structure, and $Y = 1.68\text{eV}$ for a TO structure. This corresponds to a total energy difference of only $\sim 0.17\text{eV}$ between the two structures, a difference of only 0.02%.

The energy increase required for a TO structure can be accounted for by considering that annealed MECS clusters are heated to 1200K in the annealing furnace, thus adding $8 \times 10^{-2}\text{eV}$ to the total cluster energy by thermal excitation. Cooling in the sonic expansion during the trip through the capillary separating the annealing furnace and the main vacuum chamber occurs very rapidly. It is likely that clusters are frozen into the structure they hold before this expansion.

5.5.2 Cluster Stability

Initial FIM imaging of Au clusters on W tips were very unstable and difficult to interpret. Image spots of atoms can be very sparse, with only one or two initially appearing. Composite mapping of the positions of these atoms such as the one in Fig. 5.13, however revealed that there are regions which are not imaged at all, whereas other regions yield many imaged atoms.

Images such as the ones in Figs. 5.4, 5.6, and 5.9 followed such periods of image instability. The images were then quite stable for periods between ~ 30 secs and ~ 15 mins, then deteriorated as edge atoms began to be removed via field evaporation. Occasionally, structures are imaged and return later during the imaging session as shown in Fig. 5.14, an image of an unannealed cluster deposited on a Pt/Ir tip. This suggests that there is an underlying core structure with “extra” atoms on the surface which are imaged. Because there is a high local enhancement of the electric field around these adsorbed atoms, the underlying structure is not imaged.

The cluster imaged in 5.9 showed a remarkable degree of stability. Fig. 5.15 shows a comparison of two images of this cluster taken approximately 10 mins apart. A voltage was applied to the tip during the entire time interval between these two images. It was increased shortly before the image in Fig. 5.15(b) in an attempt to more clearly image the dimly lit atoms apparent in Fig. 5.10. As a result, the atoms imaged here were removed via field evaporation and the cluster deteriorated.

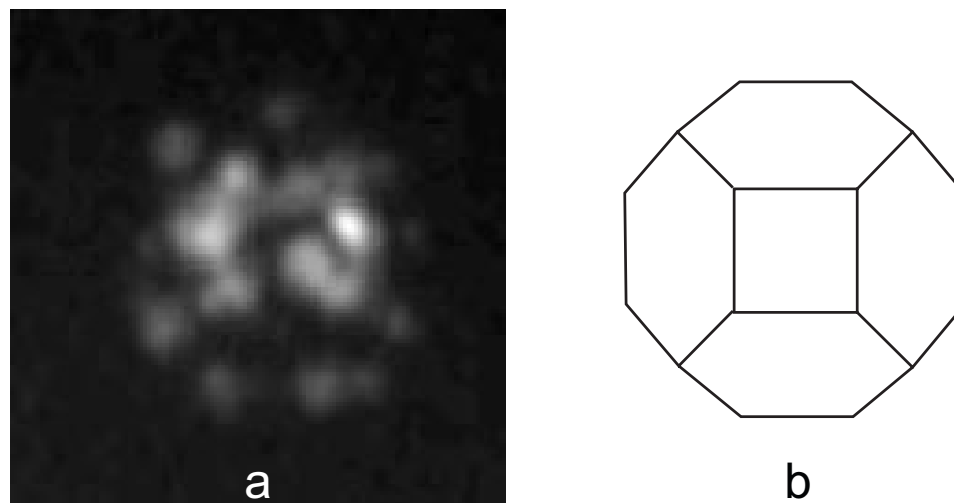


Figure 5.13 (a) Composite map for an annealed cluster deposited on a W tip, showing the underlying structure represented in (b).

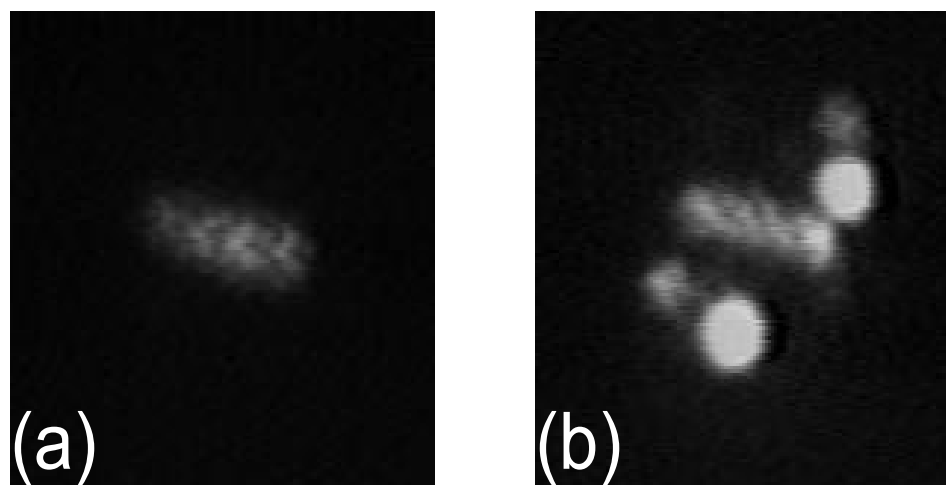


Figure 5.14 The ridge structure consisting of three or four atoms in (a) was imaged on an unannealed cluster deposited on a Pt/Ir tip, on 5/6/97 at 14:08:41. It then disappeared and later returned in (b), at 21:50:22.

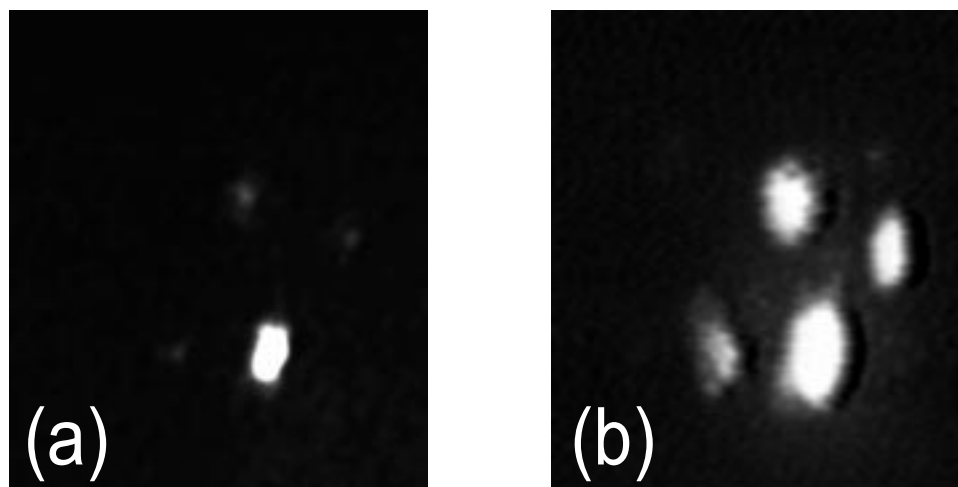


Figure 5.15 These images demonstrate the stability of an unannealed Au cluster deposited on a Pt/Ir tip. The image in (a) was taken at 4.8 kV and has been enhanced so the atoms are more clearly visible. The image in (b) was taken 9 min, 48 s later at 5.3 kV. This cluster remained essentially unchanged for over 12 minutes before the increased electric field caused it to slowly field evaporate.

6. CARBON NANOTUBE STUDIES

6.1 General Considerations

Since the discovery of C_{60} molecules [72], and more recently fullerene nanotubes, also known as carbon nanotubes or buckytubes, fullerenes have commanded intense scientific curiosity [73]. The existence of carbon nanotubes was first reported in 1991 by Iijima [74] after examining the by-products of C_{60} production. Since then, efforts have been made to increase both the quantity and the purity of the buckytubes produced, with excellent results. The buckytubes involved with the current study were produced in R.E. Smalley's lab at Rice University, where they have increased their yield to over 70% [73].

6.1.1 Physical Properties

To date, studies of buckytubes have largely focused on their physical characteristics. They can be imaged in the TEM relatively easily. Such studies have gone a long way to afford a general understanding of the growth mechanisms involved in buckytube production [75, 73, 76]. These, along with STM studies such as the ones performed by Lin *et. al* [77], have also yielded valuable insight into the atomic structure of buckytubes.

Carbon nanotubes can be subdivided into two major families. The first buckytubes discovered were multi-walled nanotubes (MWNT) [74]. These consist of a series of concentric carbon shells. As their name suggests, single-walled nanotubes (SWNT) are a single tubular shell of C atoms, basically an elongated C_{60} molecule. They typically bunch up, with several SWNTs forming a rope.

SWNTs can be thought of as being made from a sheet of C atoms arranged in a simple hexagonal array, much like a single plane of graphite. They can be characterized by using the hexagonal basis vectors \vec{a} and \vec{b} to define the line perpendicular to the axis of the tube, as shown in Fig. 6.1. This specifies a (n,m) buckytube.

For any (n,m) tube, the diameter d in nm is [73]

$$d = 0.078\sqrt{n^2 + nm + m^2}. \quad [6.1]$$

The chiral angle, θ is

$$\theta = \arctan \left[\frac{\sqrt{3m}}{(m + 2n)} \right]. \quad [6.2]$$

This gives a measure of the tube's helicity, which is a factor in determining the expected electrical properties.

6.1.2 Electrical Properties

Studies of the electrical properties of carbon nanotubes are of particular interest. The electronic structure of SWNTs have been calculated [75, 78]. Based on these calculations, SWNTs of the (n,n) variety are expected to be metallic. Nanotubes of the (n,0) family can be either metallic or semiconducting, while nanotubes with an inherent helicity are expected to be semiconducting.

Researchers at NEC have measured the electrical conductivity of SWNTs using a four probe technique [79] to avoid uncertainties due to poor contacts. They used lithographic deposition to place four W probes along the length of single MWNTs, allowing the measurements to be made. The results are difficult to interpret; the nanotubes included in the study are a mixed lot of metallic and semiconducting MWNTs and structural defects may play a role in the observations [79]. They do, however show that observations of the temperature and magnetic field dependence of the resistivity can aid in characterization of buckytubes as metallic or semiconducting, a matter which is related to their helicity [78, 79, 80].

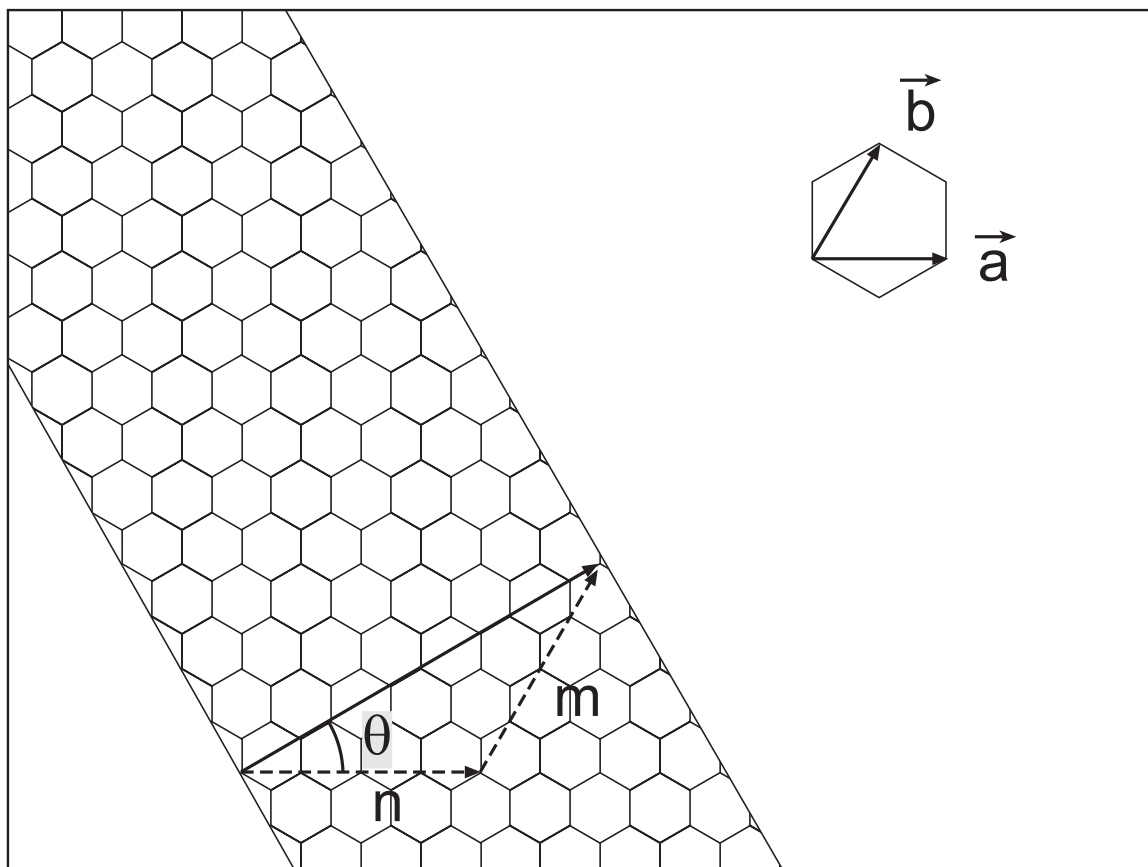
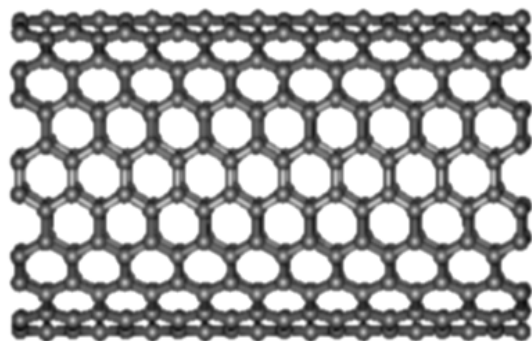
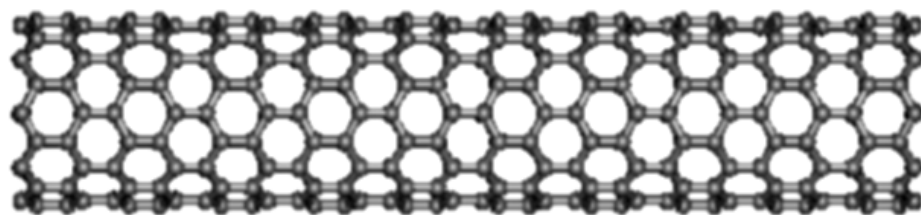


Figure 6.1 Method of characterizing SWNTs. The hexagonal basis vectors \vec{a} and \vec{b} define a line perpendicular to the axis of the tube. If one cut a belt out of a sheet of graphite defined by $n\vec{a} + m\vec{b}$ and wrapped it so that the axis of the buckytube were perpendicular to $n\vec{a} + m\vec{b}$, the result would be a (n,m) buckytube. The tube can also be described by specifying the chiral angle θ , which describes the tube's helicity.



(a)



(b)

Figure 6.2 (a) A (10,10) nanotube. (b) A (10,0) nanotube. The tubes included in this study are expected to be (10,10) nanotubes, based on size and energy considerations.

Many authors have studied field emission from arrays of carbon nanotubes [81, 80, 82, 83], and Rinzler *et al.* have recently reported field emission studies of single MWNTs [13, 73]. Their work builds on previous work on field emission from carbon nanotubes [81, 80] and from carbon fiber tips [84, 85, 82], a topic which has been of interest for roughly the last twenty years due to their performance as stable electron sources in scanning electron microscopes (SEM) and cathode ray tubes. Such fibers have shown to be capable of maintaining large, stable emission currents ($> 2\mu\text{A}$) for long periods of time [84]. In contrast to carbon fiber tips, we and other researchers have seen that carbon nanotubes burn out at emission currents greater than $\sim 1\mu\text{A}$ [13].

Previous studies [13, 81, 80] have been performed with relatively high pressure ($10^{-6} - 10^{-7}$ Torr) present in the test apparatus. We have endeavored to ensure a cleaner test environment, operating at pressures $\sim 10^{-9}$ Torr or lower. This minimizes the possibility of spurious results due to contamination of the nanotube.

6.2 Experimental Results

6.2.1 Nanotubes Included in This Study

The nanotubes included in the studies presented here are SWNTs which were synthesized in Dr. R.E. Smalley's lab at Rice University. They were presented to Michael Buss of Dr. R.P. Andres' group in the School of Chemical Engineering at Purdue for use as nanoprobe tips for AFM [12]. Based on size and energy considerations, they are expected to be (10,10) tubes.

The SWNTs were mounted on Pt field emitters which were in turn mounted on holders which were designed to fit into a TEM cradle. Using a dark field microscope to observe the process, a small amount of SEM glue is applied to the end of the Pt tip, and then a SWNT is stuck to the glue. A small voltage pulse is then applied to separate the tube from the boule, or "felt" which contains it.

Afterwards, the sample was examined using TEM. The SWNT used is shown in Fig. 6.3. This figure shows that the bundle has an uneven thickness, with the thinnest

portions having a radius $r_b = 55 \pm 5 \text{ \AA}$. For the thickest portions $r_b = 85 \pm 5 \text{ \AA}$. The radius of the end of the tube is difficult to determine because it is not resolved in the TEM due to thermal vibrations.

After characterization of the tube in the TEM it was placed in the UHV field emission microscope located in the Physics Department. It was moved yet another time into the FIM located in the Potter Engineering building so that preliminary total energy distributions (TEDs) of the emitted electrons could be recorded.

6.2.2 Field Emission From Single Walled Carbon Nanotubes

Initial attempts at imaging SWNTs using field emission were frustrated by the inherent weakness of the images. This problem was solved for the tube shown below, which was imaged using a channel plate detector equipped with an integral phosphor screen. Figure 6.4 is a contour plot of the image intensity of the field emission images. The apparent three-fold symmetry suggested by this image is consistent with emission from a bundle of SWNTs rather than a single SWNT, which would be expected to yield a round pattern. This observation is born out in the FIM images of the same bundle presented below.

A Fowler-Nordheim plot of I-V data from this bundle is shown in Fig. 6.5. Using a radius of $r_b = 85 \pm 5 \text{ \AA}$ as measured from the TEM shown in Fig. 6.3, we calculate $\beta = (2.4 \pm 0.4) \times 10^5 \text{ cm}^{-1}$ from Eqn. 3.9, which is used to calculate the applied electric field F in the next section. From the slope of the Fowler-Nordheim plot in Fig. 6.5, the work function can be calculated at $\phi = 5.1 \text{ eV}$. This is consistent with the expected metallic nature of the nanotube.

6.2.3 Total Energy Distribution of Field Emitted Electrons

Measurement of the total energy distribution (TED) of electrons field emitted from a surface can give insights into the underlying electronic structure of the sample [48, 86]. For a metal, the current density j is expected to depend on the energy relative to the Fermi energy $\epsilon = E - E_F$ as [48]



Figure 6.3 Single walled carbon nanotube (SWNT) mounted on a Pt field emitter. The bundle thickness is uneven, with the radius ranging between $55 \pm 5 \text{ \AA}$ to $85 \pm 5 \text{ \AA}$. The end of the bundle is not resolved due to thermal vibrations.

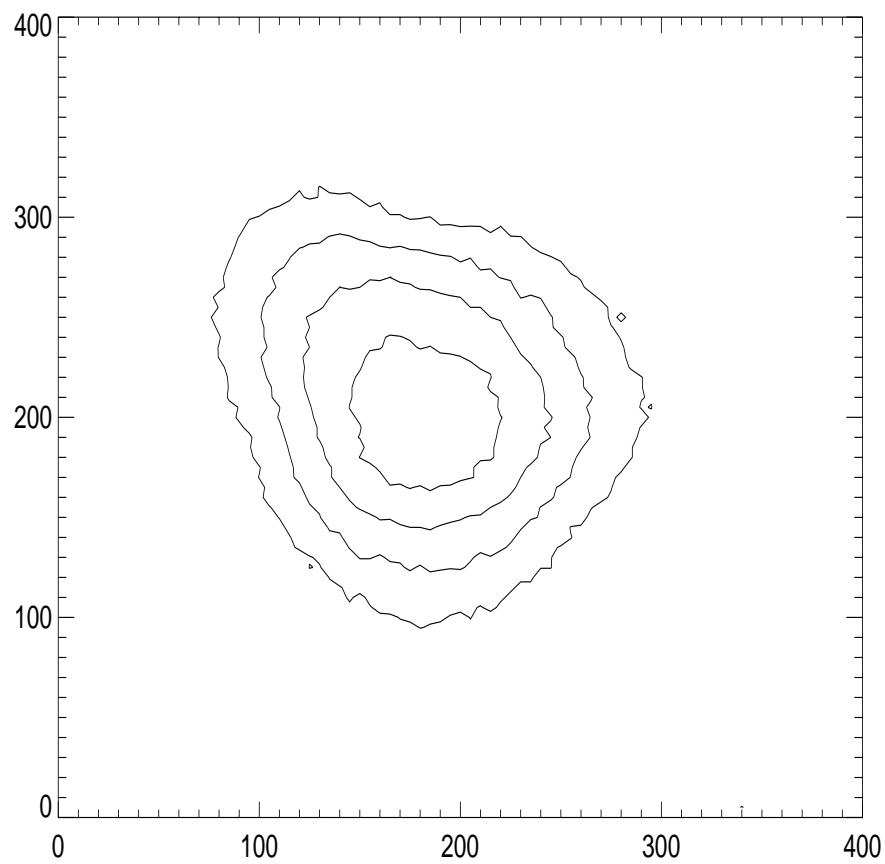


Figure 6.4 Contour plot of a field-emission micrograph of a SWNT.

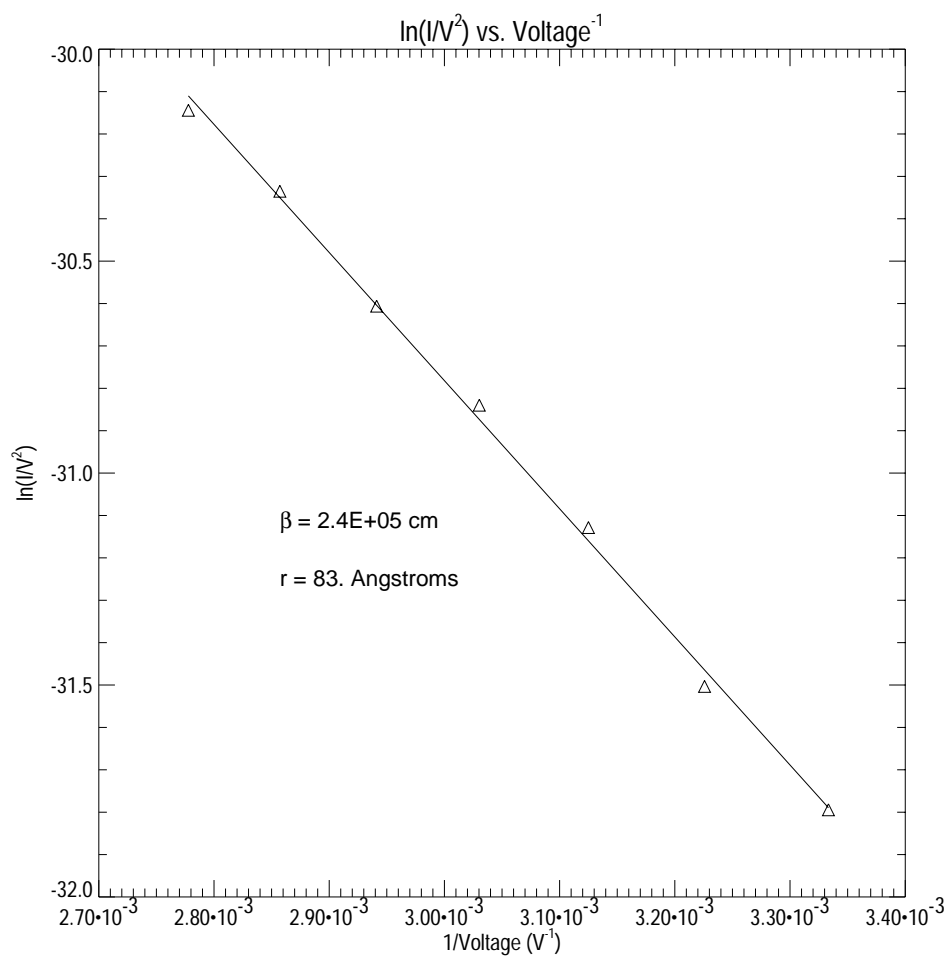


Figure 6.5 Fowler-Nordheim plot for a SWNT. The field compression factor β , and the bundle radius are given in the figure.

$$j(\epsilon) = \frac{J_0}{d} \exp\left(\frac{\epsilon}{d}\right) f(\epsilon), \quad [6.3]$$

with $f(\epsilon)$ being the Fermi-Dirac distribution function. The d factor is related to the applied field F and is given by

$$d = \frac{1}{9.76 \times 10^{-9} \frac{F}{\sqrt{\phi} t(y)}} \quad [6.4]$$

where $t(y)$ is a dimensionless constant, also related to the applied field. In order to predict the experimental TED, the energy distribution given by Eqn. 6.3 must be convoluted with a gaussian function with a FWHM corresponding to the resolution of the energy analyzer.

A comparison of an experimental TED for the buckytube imaged in Fig. 6.4 with an theoretical fit is shown in Fig. 6.6. This TED was obtained with the bundle biased -250V relative to ground in a vacuum of $\sim 5 \times 10^{-9}$ Torr held at 100K.

The theoretical fit was made by calculating the TED for an emitter and convoluting the theoretical TED with a gaussian with a FWHM of 0.15eV, corresponding to the resolution of the energy analyzer. A work function $\phi = 5.1\text{eV}$ was also used for the theoretical fit. The TED suggests that the electronic structure for this nanotube is metallic, as expected for a (10,10) nanotube [78, 75].

6.2.4 Field-ion Microscopy of SWNT Bundles

FIM of carbon structures has been performed in the past with mixed results. Tsong published FIM images of graphite tips using He as an imaging gas [30] where the images showed the basal planes of graphite but were not atomically resolved. More and Joag [85] reported He ion imaging of a carbon fiber tip which clearly shows the graphitic structure.

In order to better understand the structure of the SWNT bundle imaged in Fig. 6.4, it was imaged in the FIM using both Ar and He as imaging gases. C atoms in graphite require an electric field of 1433 MV/cm to be field evaporated from the

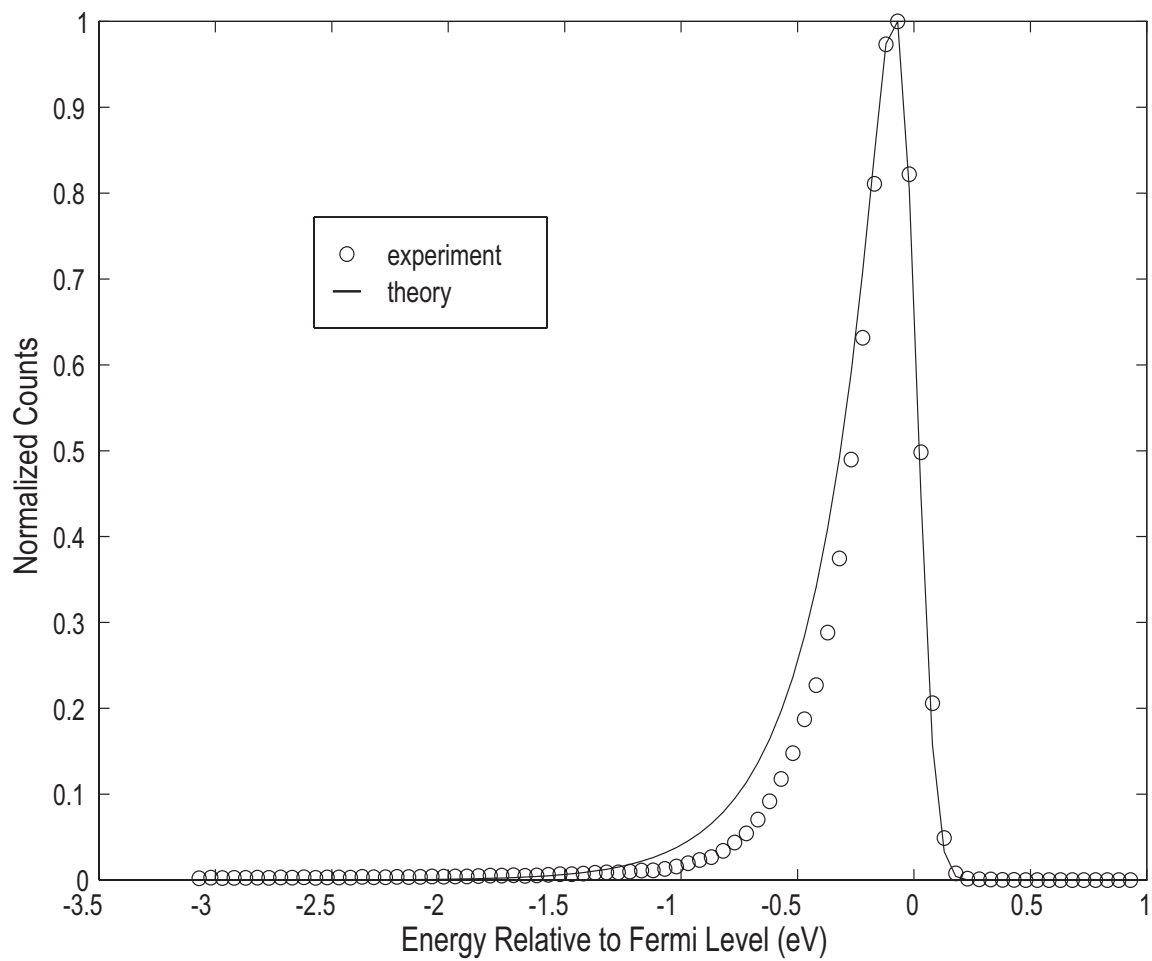


Figure 6.6 Total energy distribution of electrons field emitted from a SWNT bundle. For this fit, $T=100\text{K}$, $\phi=5.1\text{eV}$, $F=6.0\times 10^7\text{V/cm}$.

surface [3]; however Rinzler *et. al.* have suggested that “unraveling” of MWNTs may occur during field emission experiments, so the first images were taken using Ar to reduce the possibility of the bundle breaking apart in the high electric field. The bundle was first imaged using Ar at $\sim 1\text{kV}$, which corresponds to an applied electric field of $\sim 2\text{ MV/cm}$. These images were weak and showed little structure. We then switched to He to take advantage of its higher resolution and higher BIV, resulting in stronger images. A representative He image is shown in Fig. 6.7. The BIV for imaging with He was found to be 5700 V .

In this image a large ring structure can be seen, with several other atoms apparent in the lower left portion of the image. The ring structure is slightly oblong, which is suggestive of a tube which has been flattened. This deformation is to be expected, as TEM studies of nanotubes show that bundled SWNTs tend to conform to each other’s walls due to inter-tube forces.

After imaging with He, the field required to image the bundle with Ar increased to $\sim 2\text{kV}$. This indicates that the length of the tube may have been decreased, thus changing the field compression factor β in Eq. 3.11. This may explain why the tube imaged in Fig. 6.7 appear to be open tubes rather than tubes capped with C_{60} -like hemispheres. High electric fields such as the ones encountered in FIM are known to cause significant polarization of even He atoms [87, 88], resulting in field-induced chemical adsorption of atom onto kink-sites and atomic planes on FIM tips. The presence of such polarized atoms may be sufficient to hold the end of the tubes open rather than closing to form hemispherical end caps.

By considering the magnification of the FIM we can demonstrate that it is reasonable that the ring structure in Fig. 6.7 is indeed a SWNT. It is likely that the SWNT bundle imaged has an uneven end form, i.e. there is one SWNT that sticks out further than the rest. This is discussed in detail, below. The electric field lines around this SWNT will diverge more than those for the entire bundle, enhancing the local magnification. The magnification will therefore depend upon how far this SWNT sticks out. If it sticks out very little, the magnification will be essentially set

by the radius of the entire bundle. On the other hand, it could stick out so far that the magnification is set by the radius of the lone SWNT.

Assuming a typical value of 1.5 for ρ in Eq. 3.19 in both cases, a lower limit of 1.0×10^7 can be obtained by inserting a radius of 85\AA into Eq. 3.19. Similarly, if 7\AA the radius of a single (10,10) nanotube is inserted into Eq. 3.19, an upper limit of 1.2×10^8 is obtained.

Referring to the ring structure imaged in Fig. 6.7, the average radius on the phosphor screen was found to be 1.4cm. This implies a magnification of 2×10^7 , a value which is entirely reasonable when the geometry of the SWNT bundle is considered.

It should be noted here that the length of C-C bonds in graphite are 1.4\AA . It is reasonable to assume that this is also true in carbon nanotubes [75, 73]. The resolution of the FIM is only about 2.5\AA under the best of conditions, *i.e.* He imaging of a carefully field evaporated tip at 4 K. The image in Fig. 6.7 was taken using He at 100K, therefore the image is not likely to be atomically resolved. This observation is supported by the simulations of FIM images from bundles of buckytubes discussed below. Each image spot probably represents between 2 and 4 atoms, depending on the relative orientation of the adjacent tubes.

Based on size and energy considerations, it is expected that the sample was comprised primarily of (10,10) nanotubes [89]. Therefore, thin-shell model simulations of FIM images from (10,10) buckytubes were performed assuming the following models:

1. A bundle with one or more SWNT protruding further than the rest.
2. A bundle with all of its SWNTs terminating evenly.
3. A bundle with a rounded end form.

These scenarios are illustrated in Fig. 6.8.

For the first and second model, the simulations assumed that the images would result from ionization events occurring over the atoms terminating the nanotube. The image positions were then projected from a point $2r$ from the end of the tube/bundle,

where r is the radius of the tube or bundle in question. The image spots are plotted as gaussians to approximate the resolution of the FIM.

A simulated image from a single (10,10) buckytube is shown in Fig. 6.9. Note that the image spots from each of the nearest neighbor pairs which terminate the tube have coalesced into a single spot due to the limited resolution. A simulated image from a (10,0) nanotube is also given in Fig. 6.10 to show that FIM images from so-called (n,n) tubes are expected to be markedly different from (n,0) tubes. Note that it is smaller in size, and the single atoms terminating the tube are more clearly resolved due to their greater separation.

Fig. 6.11 shows a series of simulated images of a bundle of 19 (10,10) buckytubes. This corresponds to a bundle radius of about 7 nm. It is smaller than the bundle imaged in Fig. 6.3, however a larger bundle would have contained over 10,000 atoms, making it too cumbersome to work with. Note that some of the image spots are brighter than others. This is due to the fact that the gaussians which are plotted for adjacent atoms overlap, resulting in a brighter spot. The dependence of the brightness of these spots is illustrated in Fig. 6.11. The central (10,10) tube in the bundle was rotated 10° on its axis and then the image was simulated again. As the central tube rotates through 30° , the bright spots move, then disappear, then reappear. This may explain why some of the image spots in the experimental image are brighter than others.

The third model yielded simulated images which were similar to the second, as shown in Fig. 6.12. This scenario, or a combination of this scenario with scenario (2) is likely the most physically realistic. This is because the electric field is highest around the perimeter of the bundle. As the electric field is increased, atoms will field evaporate from the bundle and the end form is rounded in the same manner that the surface of a conventional field ion tip is rounded by field evaporation during imaging. As can be seen from the simulated image, the features are similar, except for the fact that the tubes near the outside of the bundle yield oval patterns.

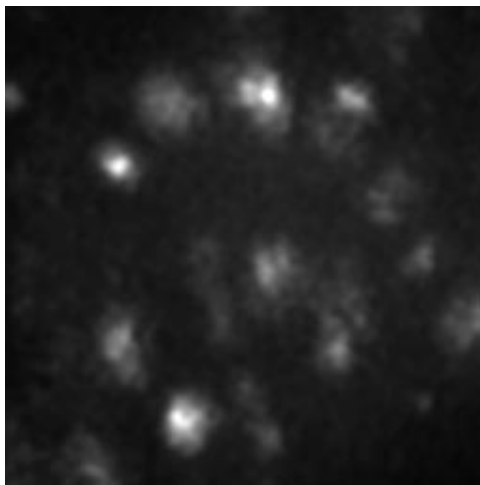


Figure 6.7 He FIM image of a SWNT bundle. This was taken at $\sim 100\text{K}$, 5700V .

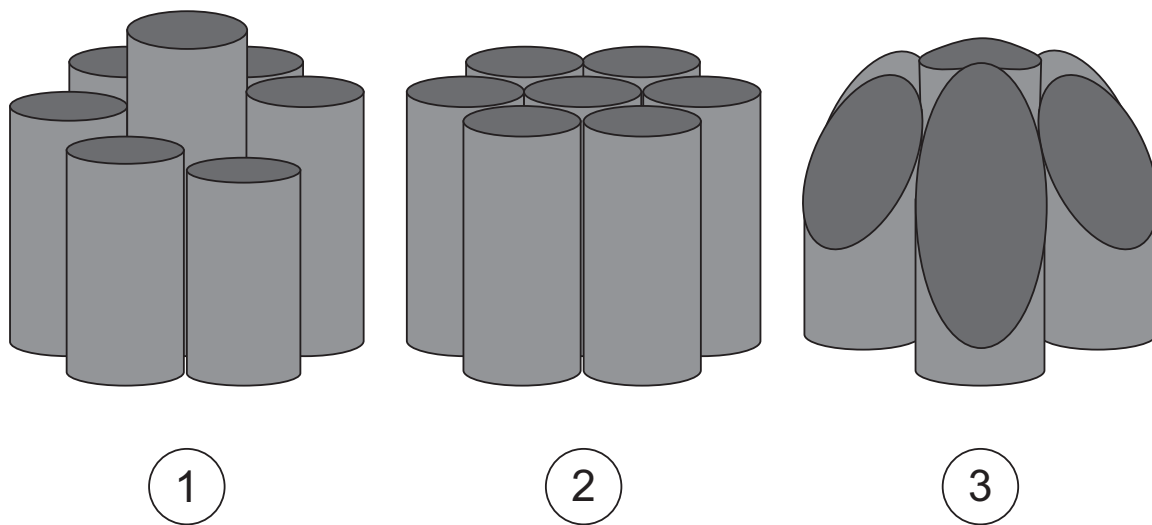


Figure 6.8 Scenarios used in simulations of FIM images from buckytubes. 1) bundle with one or more tubes sticking out further than the rest. 2) Bundle with all tubes terminating together. 3) Bundle with a rounded end form.

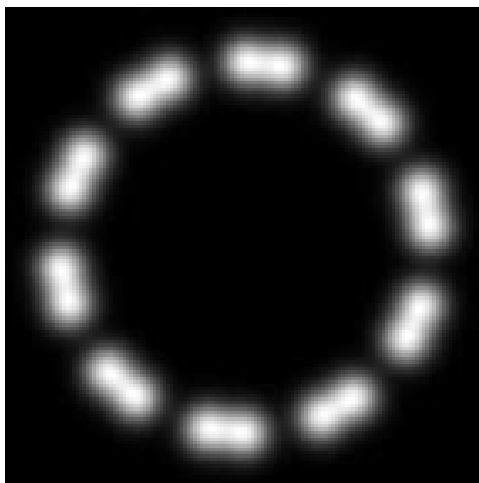


Figure 6.9 Simulated image from a single (10,10) nanotube. Note that the image spots from each of the C doublets terminating the tube have coalesced into single spots.

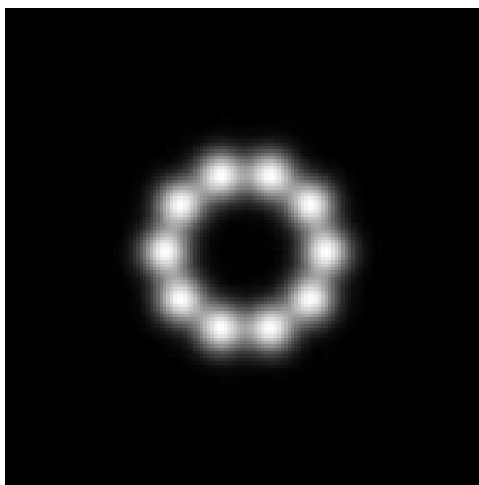


Figure 6.10 Simulated image from a single (10,0) nanotube.

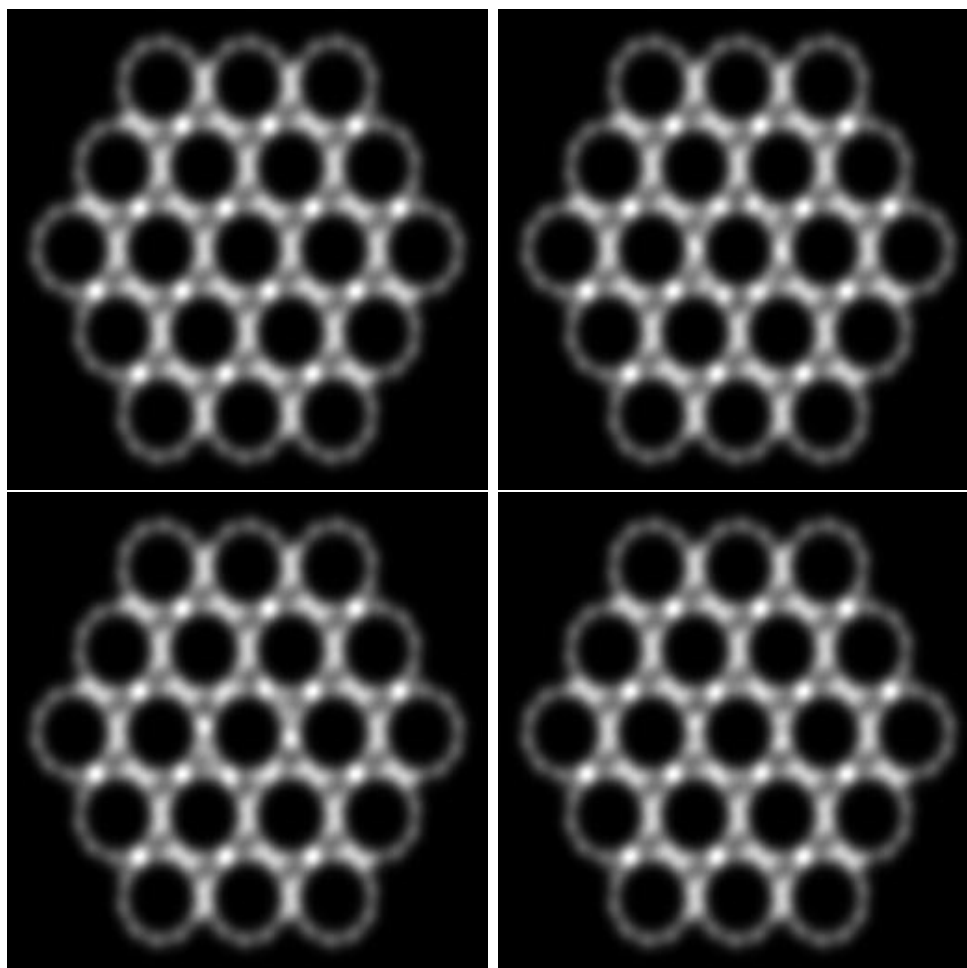


Figure 6.11 Simulated images from a bundle of 19 (10,10) nanotubes. Focus your attention on the tube in the center of the bundle. a) Original orientation. b) Central tube rotated 10° clockwise. c) Central tube rotated 20° clockwise. d) Central tube rotated 30° clockwise.

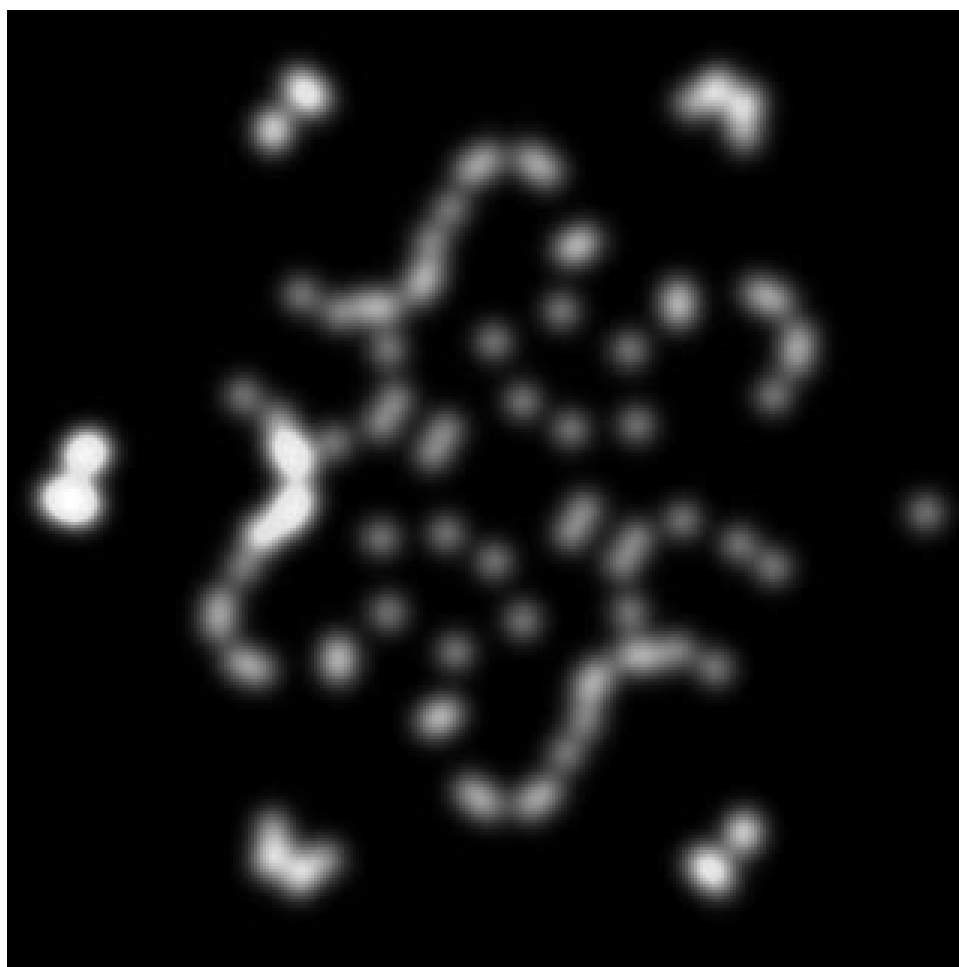


Figure 6.12 Simulated image from a bundle of SWNTs with a rounded end form.

7. CONCLUSIONS

During the course of this work a novel field-ion microscope for the study of supported nanometer-size structures was developed. With this apparatus we were able to further our knowledge of the structural and electrical properties of both nanometer-size clusters and carbon nanotubes by combining the use of field emission and field-ion techniques.

7.1 Supported Nanometer-Size Au Clusters

Techniques for depositing nanometer-size clusters onto the end of field emission tips, first developed by Castro *et al.* [67] were employed to deposit a number of Au clusters onto a variety of tip materials for study. These techniques were improved upon by physically attaching the FIM to the cluster source, thus eliminating the need for a portable transfer cell which was used in previous studies [67, 68]. Cluster deposition was able to be carried out in a vacuum environment of $\sim 10^{-9}$ Torr as opposed to the $\sim 10^{-6}$ Torr during deposition in the previous studies.

Studies of deceleration of clusters in the MECS showed that the mean cluster size can be accurately predicted by measuring the stopping pressure in the deceleration box. Comparisons of the predicted cluster diameters with diameters as measured from TEM micrographs of deposited clusters show that it is likely that clusters are incompletely accelerated to the velocity of the carrier gas. This is reasonable, since it is unlikely that there will be a sufficient number of collisions to fully accelerate the clusters.

Field-ion imaging of supported clusters on a variety of substrates have proven the validity of the FIM technique for cluster studies. Annealed clusters revealed

a truncated octahedron structure, as opposed to the Marks-decahedron. This was confirmed by matching simulated FIM images to experimental images, with a high degree of success.

FIM imaging of clusters often initially showed a high degree of instability, with stable structures emerging after 5-10 minutes of imaging. These observations imply that in each case there is a stable core structure with adatoms on the different faces of the cluster. As the cluster is imaged, these adatoms migrate to the edges of the cluster due to the high electric field and are removed via field evaporation, thus “cleaning” the structure. The underlying core eventually emerges to be imaged, and then deteriorates as weakly bound atoms are themselves removed.

Other observations on the stability of an unannealed Au cluster on a Pt/Ir substrate demonstrated the remarkable stability of clusters produced in the MECS. Continuous imaging of one cluster for over 12 minutes showed absolutely no change in the atomic structure. It was only when a high electric field was applied that the cluster deteriorated, caused by field evaporation of individual atoms from the surface of the cluster.

7.2 Carbon Nanotubes

Single walled carbon nanotubes were mounted and imaged using field emission microscopy. Field emission from SWNTs and their behavior in high electric fields is interesting both from the standpoint of nanotube synthesis and for their potential applications. SWNTs are capable of stable electron emission, an important factor in deciding their suitability in devices utilizing field emitter arrays.

Using Fowler-Nordheim analysis of electron emission from a nominal (10,10) SWNT, an estimate of 90\AA was obtained for the radius of the emitting bundle. This value agrees well with the radius as measured from a TEM of the same bundle. Analysis also yielded a relatively high field enhancement factor. This is to be expected due to the very small radius of curvature.

Measurement of the total energy distribution (TED) of field emitted electrons yielded insights into their electrical properties. Analysis of the TED showed that the SWNTs studied had electrical properties which were metallic in nature. This observation agrees with theoretical predictions for (n,n) SWNTs.

Field-ion imaging of the same bundle showed that it was indeed a bundle of closely packed graphite tubules. It is unlikely that the images obtained were atomically resolved, based on the 1.4 Å length of C-C bonds in the tubules. Simulations of FIM images from lone nanotubes and bundles of nanotubes supported this observation. Agreement was good between the experimental images and simulated images from bundles with flat and rounded end forms.

7.3 Recommendations and Conclusion

Despite the success of applying the technique of field-ion microscopy to the study of cluster and buckytube structures, a number of improvements can be made which will enable the most to be made with the present equipment. In particular, the elimination of the high voltage breakdowns which chronically affect the FIM will increase the range of its usefulness. These breakdowns typically begin occurring in the 7-10kV range, and can adversely affect the quality of the images obtained, particularly when using the MCP for imaging. While their occurrence can be minimized by ensuring that the tip mounting bases are extremely clean, this is not always sufficient. Modifications to the tip mounting and cooling components are almost certainly necessary to completely eliminate them.

The inclusion of a variety of substrates used as supports for nanometer-size clusters also showed promise in probing the phenomenon of cluster wetting the surface after deposition. Continuing studies would almost certainly benefit from a more detailed study of this phenomenon. While Pt and Pt/Ir substrates proved to be less apt to cause clusters to wet, they are difficult to work with in practice. In contrast, W tips rarely need replacement, but clusters are more likely to wet on W than on Pt or

Pt/Ir. The exploration of other tip materials such as Ta, Ni, or Mo could lead to a tip which is easy to work with, yet does not cause deposited clusters to wet.

The results of investigating the structure of Au clusters also shows promise when contemplating research on the structure of other cluster materials. In the past the MECS has been used to produce clusters from a variety of materials, among them Ag, Cu, Sn, Fe, and Ni. Use of the FIM technique should lead to new insights into the mechanisms governing the structure of nanometer size clusters, since the size dependence of cluster structure is expected to be different for each of these materials. The effects of oxidation, especially in Ag and Fe clusters could be ascertained.

In conclusion, the application of the technique of field-ion microscopy to the study of cluster and buckytube structure have opened new avenues of research. In particular, the most recent work on carbon nanotubes begin to realize the true potential of the experimental apparatus. With the planned addition of an electrostatic lens to improve the resolution of the electron energy analyzer, valuable information on the electronic and structural properties of supported clusters can be obtained. More meaningful correlations between the cluster atomic and electronic properties can be made, since the use of FIM imaging will be able to ascertain the exact structure and orientation of the clusters under study.

LIST OF REFERENCES

LIST OF REFERENCES

- [1] M. Buss, (private communication).
- [2] S. H. Overbury, P. A. Bertrand, and G. A. Somorjai, *Chemical Reviews* **75** (5), 547 (1975).
- [3] E.W. Müller and T.T. Tsong, *Field Ion Microscopy, Principles and Applications*, American Elsevier Publishing Co., 1969.
- [4] A.N. Patil, D.Y. Paithankar, N. Otsuka, and R.P. Andres, *Z. Phys. D* **26**, 135 (1993).
- [5] Dilip Paithankar, PhD thesis, Purdue University, 1994.
- [6] P.M. Ajayan and L.D. Marks, *Phys. Rev. Lett.* **60**, 585 (1988).
- [7] M.K. Miller and G.D.W. Smith, *Atom Probe Microanalysis*, Materials Research Society; Pittsburgh, PA, 1989.
- [8] Atul Naredo Patil, PhD thesis, Purdue University, 1994.
- [9] Seung Bin Park, PhD thesis, Purdue University, 1988.
- [10] Michael S. Montemerlo, J. Christopher Love, Gregory J. Opiteck, David Goldhaber-Gordon, and James C. Ellenbogen, *Technologies and designs for electronic nanocomputers*, 1996.
- [11] M. Dorogi, J. Gomez, R. Oschifin, R.P. Andres, and R. Reifengerger, *Phys. Rev.* **B52**, 9071 (1995).
- [12] Hongjie Dai, Jason H. Hafner, Andrew G. Rinzler, Daniel T. Colbert, and Richard E. Smalley, *Nature* **384**, 147 (1996).
- [13] A.G. Rinzler, J.H. Hafner, P. Nikolaev, L. Lou, S.G. Kim, D. Tománek, P. Nordlander, D. T. Colbert, and R.E. Smalley, *Science* **269**, 1550 (1995).
- [14] M.R. Hoare and P. Pal, *Adv. Phys.* **20**, 161 (1971).
- [15] S. Iijima and T. Ichihashi, *Phys. Rev. Lett.* **56**, 616 (1986).

- [16] L.D. Marks, Rep. Prog. Phys. **57**, 603 (1994).
- [17] D.M. Schaefer, A. Ramachandra, R.P. Andres, and R. Reifenberger, Z. Phys. D **26**, S249 (1993).
- [18] D.M. Schaefer, A. Patil, R.P. Andres, and R. Reifenberger, Appl. Phys. Lett. **63**, 1492 (1993).
- [19] David M. Schaefer, PhD thesis, Purdue University, 1993.
- [20] S. Hong, D. B. Janes, D. McInturff, R. Reifenberger, and J. M. Woodall, Appl. Phys. Lett. **68**, 2258 (1996).
- [21] D. Schleef, D. M. Schaefer, R. P. Andres, and R. Reifenberger, Phys. Rev. B **submitted**, L925 (1996).
- [22] C.L. Cleveland, U. Landman, M.N. Shafiqullin, P.W. Stephens, and R.L. Whetten, Z. Phys. **D40**, 503 (1997).
- [23] Mong-Ea Lin, PhD thesis, Purdue University, 1991.
- [24] T. Castro, Y.Z. Li, R. Reifenberger, E. Choi, S.B. Park, and R.P. Andres, J. Vac. Sci. Technol. **A7**, 2845 (1989).
- [25] E.W. Müller, Z. Physik **131**, 136 (1951).
- [26] R. Gomer, *Field Emission and Field Ionization*, Harvard University Press, 1961.
- [27] Allan J. Melmed and Erwin W. Müller, J. Chem. Phys. **29**, 1037 (1958).
- [28] Robert Gomer and Donald Speer, J. Chem. Phys. **21**, 73 (1953).
- [29] S.C. Wang and T.T. Tsong, Phys. Rev. B **26**, 6470 (1982).
- [30] T.T. Tsong, *Atom Probe Field Ion Microscopy*, Cambridge University Press, 1990.
- [31] G. L. Kellogg, Surface Science Reports **21**, 1 (1994).
- [32] G.L. Kellogg, in *Science and Technology of Atomically Engineered Materials*, edited by P. Jena, S.N. Khanna, and B.K. Rao, pages 91–97, World Scientific, Singapore, 1996.
- [33] S.C. Wang and G. Ehrlich, Phys. Rev. Lett. **75**, 2964 (1995).
- [34] C.L. Cleveland and U. Landman, J. Chem. Phys. **94**, 7379 (1991).
- [35] C.L. Cleveland, U. Landman, T.G. Schaaff, M.N. Shafiqullin, P.W. Stephens, and R.L. Whetten, Phys. Rev. Lett. **79** (1997).

- [36] W.D. Luedtke and U. Landman, Phys. Rev. Lett. **73**, 569 (1994).
- [37] P.M. Ajayan and L.D. Marks, Phys. Rev. Lett. **63**, 279 (1989).
- [38] F. Ercolessi, W. Andreoni, and E. Tosatti, Phys. Rev. Lett. **66**, 911 (1991).
- [39] T. Castro, R. Reifengerger, E. Choi, and R.P. Andres, Surf. Sci. **234**, 43 (1990).
- [40] W. Mahoney, D. M. Schaefer, A. Patil, R. P. Andres, and R. Reifengerger, Surf. Sci. **316**, 383 (1994).
- [41] D. Maugis and H.M. Pollock, Acta Metall. **32**, 1323 (1984).
- [42] Nobuo Ohmae, Masataka Umeno, and Kenji Tsubouchi, ASLE Transactions **30**, 409 (1987).
- [43] E.W. Plummer and T.N. Rhodin, J. Chem. Phys. **49**, 3479 (1968).
- [44] K.L. Johnson, K. Kendall, and A.D. Roberts, Proc. R. Soc. London **A324**, 301 (1971).
- [45] J. P. Jones, Journal of Solid State Chemistry **104**, 149 (1993).
- [46] M. Drechsler, Surface Science **70**, 1 (1978).
- [47] R.H. Good and E.W. Müller, Field emission, in *Handbuch der Physik, 2nd. edition, Vol 2*, page 176, Springer Verlag, 1956.
- [48] J.W. Gadzuk and E.W. Plummer, Rev. Mod. Phys. **43**, 487 (1973).
- [49] Y. C. Chen and D. N. Seidman, Surface Science **26**, 61 (1971).
- [50] D.J. Rose, J. Appl. Phys. **27**, 215 (1956).
- [51] T. Castro, R. Reifengerger, E. Choi, and R.P. Andres, Phys. Rev. B **42**, 8548 (1990).
- [52] Caio M C de Castilho and David R. Kingham, J. Phys. D: Appl. Phys **20**, 116 (1987).
- [53] A.J.W. Moore, J. Phys. Chem. Solids **23**, 907 (1962).
- [54] R. Smith and J.M. Walls, J. Phys. D **11**, 409 (1978).
- [55] Herbert Goldstein, *Classical Mechanics*, Addison-Wesley Publishing Company, 1980.
- [56] E. W. Müller and O. Nishikawa, Rev. Sci. Instr. **36**, 556 (1965).
- [57] A.J. Melmed, J. Vac. Sci. Technol. **B9**, 601 (1991).

- [58] Mircea Fotino, Appl. Phys. Lett. **60**, 2395 (1992).
- [59] L. Libioulle, Y. Houbion, and J.-M. Gilles, Rev. Sci. Instrum. **66**, 97 (1995).
- [60] A.P. Janssen and J.P. Jones, J. Phys. D: Appl. Phys. **4**, 118 (1971).
- [61] C. Schiller, A.A. Koomans, T.L. van Rooy, C. Schönenberger, and H.B. Elswijk, Surface Science **339**, L925 (1995).
- [62] Jeffery David Bielefeld, PhD thesis, Purdue University, 1996.
- [63] H-P. Cheng and U. Landman, Science **260**, 1304 (1993).
- [64] G. Betz and W. Husinsky, Nuclear Instruments and Methods in Physics Research B **122**, 311 (1997).
- [65] Seung Bin Park, PhD thesis, Purdue University, 1988.
- [66] R.P. Andres, (private communication).
- [67] T. Castro, PhD thesis, 1989, Purdue University (unpublished).
- [68] M.E. Lin, PhD thesis, 1991, Purdue University (unpublished).
- [69] A.Cetronio, Surf. Sci. **44**, 109 (1974).
- [70] Tom Castro, PhD thesis, Purdue University, 1989.
- [71] D. Lovall, R.P. Andres, and R. Reifengerger, in *Science and Technology of Atomically Engineered Materials*, edited by P. Jena, S.N. Khanna, and B.K. Rao, pages 137–46, World Scientific, Singapore, 1996.
- [72] H.W. Kroto, J.R. Heath, S.C. O'Brien, R.F. Curl, and R.E. Smalley, Nature **318**, 162 (1985).
- [73] Boris I. Yakobson and Richard E. Smalley, American Scientist **85**, 324 (1997).
- [74] Sumio Iijima, Nature **354**, 56 (1991).
- [75] P.C. Eklund M.S. Dresselhaus, G. Dresselhaus, *Science of Fullerenes and Carbon Nanotubes*, Academic Press, Inc., 1996.
- [76] T.W. Ebbesen and P.M. Ajayan, Nature **358**, 220 (1992).
- [77] N. Lin, J. Ding, S. Yang, and N. Cue, Carbon **34**, 1295 (1996).
- [78] J.W. Mintmire, B.I. Dunlap, and C.T. White, Physical Review Letters **1992**, 631 (1992).

- [79] T.W. Ebbesen, H.J. Lezec, H. Hiura, J.W. Bennett, H.F. Ghaemi, and T. Thio, *Nature* **382**, 54 (1996).
- [80] B.H. Fishbine, C.J. Miglionico, K.E. Hackett, K.J. Hendricks, X.K. Wang, R.P.H. Chang, J.D. Shovlin, and M.E. Kordesch, *Mat. Res. Soc. Symp. Proc.* **359**, 93 (1995).
- [81] B.H. Fishbine, C.J. Miglionico, K.E. Hackett, and K.J. Hendricks, *Mat. Res. Soc. Symp. Proc.* **349**, 319 (1994).
- [82] Yu.V. Gulyaev, Z.Ja. Kosakovskaja, N.I. Sinitsyn, G.V. Torgashov, E.A. Fedorov, Yu.F. Zakharchenko, and V.P. Val'chuk, *Mat. Res. Soc. Symp. Proc.* **359**, 99 (1995).
- [83] Q.H. Wang, T.D. Corrigan, J.Y. Dai, R.P.H. Chang, and A.R. Krauss, *Appl. Phys. Lett.* **70**, 3308 (1997).
- [84] M.S. Mousa, *Applied Surface Science* **94/95**, 129 (1996).
- [85] Mahendra A. More and Dilip S. Joag, *J. Phys. D: Appl. Phys.* **25**, 1844 (1992).
- [86] R.D. Young, *Phys. Rev.* **113**, 110 (1958).
- [87] H.J. Kreuzer, *Surface Science* **246**, 336 (1990).
- [88] W.A. Schmidt, Yu. Suchorski, and J.H. Block, *Surface Science* **301**, 52 (1994).
- [89] J.M. Cowley, Pavel Nikolaev, Andreas Thess, and Richard E. Smalley, *Chem. Phys. Lett.* **in press**, 501 (1997).

APPENDICES

Appendix A: A Listing of Programs Used During This Research

A.1 C programs

1. **all.c**: Simulates FIM images from clusters in a range of orientations. Outputs pgm format images and Xmol xyz files for each orientation. Requires input files in format (1), below.
2. **cluster.c** Outputs xyz data files for some TO-family clusters.
3. **coord2.c**: Plots simulated images and provides coordinates of image spots. Used for **all.c** and **fmsingle.c**.
4. **euler.c**: Rotates atom positions through arbitrary Euler angles. Used for **all.c** and **fmsingle.c**.
5. **fm.c**: Simulates FIM images from tips and clusters. Outputs pgm format image files.
6. **fmsingle.c**: Generates a simulated FIM image for a specified orientation. Outputs pgm format images and Xmol xyz files for each orientation. Requires input files in format (1), below.
7. **im.c**: Plots simulated images. Used for **fm.c**.
8. **xyz2dat.c**: Converts Xmol xyz files for use with FIM simulation programs.
9. **fownord.c**: DOS program which outputs a voltage to control a high voltage power supply and reads in currents from a Keithley 485 picoammeter. Specifically written to take Fowler-Nordheim data.

A.2 IDL programs

1. **fownord.pro**: Plots Fowler-Nordheim data and calculates β and the tip radius. Data must be formatted as in format (3), below.
2. **center.pro**: Procedure to center FIM image data. Used in **interactsim.pro**, **matchfim.pro**, and **imagepoints.pro**.
3. **euler.pro**: Rotates atom position data through a specified series of Euler angles. Used in **interactsim.pro**, **matchfim.pro**, and **imagepoints.pro**.
4. **imagepoints.pro**: Interactive program to specify image coordinates used to match experimental and simulated FIM images. Requires **euler.pro** and **center.pro**.
5. **interactsim.pro**: Interactive program to simulate FIM images from structures. Requires **euler.pro** and **center.pro**. Requires input files in format (2), below.
match.dat
6. **matchfim.pro**: Program to match experimental and simulated FIM images. Requires **euler.pro** and **center.pro**. Requires input files in format (2) below, and output file from **imagepoints.pro**.
7. **matchfim2.pro**: Program to match experimental and simulated FIM images. Requires **euler.pro** and **center.pro**. Differs from **matchfim.pro** in that it plots the simulated image over the experimental image. Requires input files in format (2) below, and output file from **imagepoints.pro**.

A.3 Input file formats

1. Input for C-language FIM simulations

format		example
--------	--	---------

# of atoms in file		201		
radius of cluster		20.426120		
x1 y1 z1		-0.000000	3.926547	4.426388
x2 y2 z2		1.965439	1.965439	4.335424
x3 y3 z3		3.926547	-0.000000	4.426388
x4 y4 z4		-1.965439	1.965439	4.335424
x5 y5 z5		-0.000000	-0.000000	4.235872
...		...		

2. Input for IDL-language FIM simulations

format		example			
# of atoms in file		201			
x1 y1 z1		-0.000000	3.926547	4.426388	
x2 y2 z2		1.965439	1.965439	4.335424	
x3 y3 z3		3.926547	-0.000000	4.426388	
x4 y4 z4		-1.965439	1.965439	4.335424	
x5 y5 z5		-0.000000	-0.000000	4.235872	
...		...			

3. Input for fownord.pro

format		example						
#n of data points		7						
V1 V2 V3 ... Vn		300	310	320	330	340	350	360
I1 I2 I3 ... In		1.4	2.0	3.1	4.4	5.9	8.2	10.5

note: I1, I2, etc. are in nA units.

Appendix B: Cluster Coordinates

These coordinates represent the lowest energy structure at 0 K. The coordinates for the TO clusters were provided by Michael Buss of Dr. R.P. Andres' research group. The coordinates for the Ih cluster were provided by Dilip Paithankar, also of Dr. Andres' research group.

B.1 Coordinates for a 38 atom Au cluster with TO structure

Atom	x	y	z	atom	x	y	z
1	-0.012699	1.990921	2.308186	20	-3.838692	1.933747	6.172875
2	1.901057	0.0638	2.263034	21	-1.987526	0.006931	6.128129
3	-1.940155	0.077176	2.282783	22	-0.007121	-1.987241	6.081488
4	-0.026435	-1.849868	2.237747	23	1.906999	-3.851617	6.037566
5	0.003976	3.880188	4.268073	24	-3.852503	-1.906893	6.102528
6	2.061895	2.095341	4.080367	25	-1.934466	-3.838308	6.057355
7	3.83577	0.021807	4.177712	26	0.023516	3.809765	8.108564
8	-2.068134	2.109674	4.101686	27	2.082906	2.019636	8.209767
9	-0.010108	0.036436	4.130714	28	3.855313	-0.048612	8.018438
10	2.047031	-2.033998	4.00482	29	-2.047125	2.03397	8.231001
11	-3.855329	0.048589	4.217294	30	0.010112	-0.036431	8.105055
12	-2.082804	-2.019574	4.026139	31	2.068042	-2.109713	8.134045
13	-0.023527	-3.809812	4.127123	32	-3.835787	-0.021832	8.058102
14	1.934425	3.838247	6.178418	33	-2.061795	-2.095287	8.155279
15	3.8524	1.906935	6.133251	34	-0.003986	-3.880226	7.967803
16	-1.90689	3.851646	6.198208	35	0.026427	1.849935	9.997951
17	0.00712	1.987125	6.154284	36	1.940176	-0.077192	9.952943
18	1.987462	-0.006937	6.107652	37	-1.901022	-0.063818	9.972774
19	3.838785	-1.933639	6.062904	38	0.012691	-1.990867	9.927686

B.2 Coordinates for a 39 atom cluster with TO structure

This structure was used to match an orientation to the cluster in Fig. 5.6

atom	x	y	z	atom	x	y	z
1	1.00706	-2.67210	-3.21307	20	0.03051	2.67588	-3.36403
2	0.14253	-4.15162	-1.10548	21	-0.86104	1.23534	-1.29729
3	-1.52158	-1.76409	-3.61266	22	-1.75561	-0.29563	0.88372
4	-2.38603	-3.24349	-1.50507	23	-2.56463	-1.76584	2.96354
5	3.05241	-0.90527	-2.88810	24	-3.36246	2.10463	-1.65609
6	2.34834	-2.56476	-0.83717	25	-4.22889	0.62187	0.45625
7	1.32158	-3.86756	1.33173	26	3.74111	2.04908	-0.53180
8	0.55908	0.00234	-3.53279	27	3.08887	0.61185	1.69639
9	-0.35636	-1.52870	-1.21924	28	2.01033	-0.91302	3.68818
10	-1.29967	-3.17887	0.99920	29	1.29959	3.17888	-0.99928
11	-2.01039	0.91292	-3.68826	30	0.35635	1.52862	1.21918
12	-3.08876	-0.61187	-1.69633	31	-0.55919	-0.00240	3.53266
13	-3.74119	-2.04923	0.53170	32	-1.32162	3.86752	-1.33177
14	4.22880	-0.62193	-0.45631	33	-2.34829	2.56453	0.83708
15	3.36244	-2.10463	1.65595	34	-3.05245	0.90528	2.88812
16	2.56468	1.76570	-2.96354	35	2.38605	3.24337	1.50492
17	1.75548	0.29554	-0.88373	36	1.52155	1.76397	3.61260
18	0.86099	-1.23537	1.29719	37	-0.14254	4.15155	1.10548
19	-0.03039	-2.67599	3.36399	38	-1.00701	2.67212	3.21304
				39	-2.06178	-4.32914	3.16241

B.3 Coordinates for a 201 atom Au cluster with TO structure

atom	x	y	z	atom	x	y	z
1	0.00000	3.92655	4.42639	101	0.00000	0.00000	12.23578
2	1.96544	1.96544	4.33542	102	2.04097	-2.04097	12.23578
3	3.92655	0.00000	4.42639	103	4.08574	-4.08574	12.23578
4	-1.96544	1.96544	4.33542	104	5.96278	-5.96278	12.23578
5	0.00000	0.00000	4.23587	105	-7.80939	3.92655	12.23578
6	1.96544	-1.96544	4.33542	106	-5.99218	2.01986	12.23578
7	-3.92655	0.00000	4.42639	107	-3.97751	0.00000	12.23578
8	-1.96544	-1.96544	4.33542	108	-2.04097	-2.04097	12.23578
9	0.00000	-3.92655	4.42639	109	0.00000	-3.97751	12.23578
10	0.00000	5.96278	6.27300	110	2.01986	-5.99218	12.23578
11	2.06317	4.06793	6.17434	111	3.92655	-7.80939	12.23578
12	4.06793	2.06317	6.17434	112	-7.99990	0.00000	12.23578
13	5.96278	0.00000	6.27300	113	-5.99218	-2.01986	12.23578
14	-2.06317	4.06793	6.17434	114	-4.08574	-4.08574	12.23578
15	0.00000	2.01986	6.24359	115	-2.01986	-5.99218	12.23578
16	2.01986	0.00000	6.24359	116	0.00000	-7.99990	12.23578
17	4.06793	-2.06317	6.17434	117	-7.80939	-3.92655	12.23578
18	-4.06793	2.06317	6.17434	118	-5.96278	-5.96278	12.23578
19	-2.01986	0.00000	6.24359	119	-3.92655	-7.80939	12.23578
20	0.00000	-2.01986	6.24359	120	1.96544	7.90035	14.20122
21	2.06317	-4.06793	6.17434	121	4.06793	6.06144	14.29895
22	-5.96278	0.00000	6.27300	122	6.06144	4.06793	14.29895
23	-4.06793	-2.06317	6.17434	123	7.90035	1.96544	14.20122
24	-2.06317	-4.06793	6.17434	124	-1.96544	7.90035	14.20122
25	0.00000	-5.96278	6.27300	125	0.00000	5.99218	14.25564
26	0.00000	7.80939	8.30923	126	2.08173	4.07188	14.31751
27	2.06317	6.06144	8.16785	127	4.07188	2.08173	14.31751
28	4.08708	4.08708	8.14869	128	5.99218	0.00000	14.25564
29	6.06144	2.06317	8.16785	129	7.90035	-1.96544	14.20122
30	7.80939	0.00000	8.30923	130	-4.06793	6.06144	14.29895
31	-2.06317	6.06144	8.16785	131	-2.08173	4.07188	14.31751
32	0.00000	4.08574	8.15004	132	0.00000	2.04097	14.27674

33	2.08173	2.08173	8.16390	133	2.04097	0.00000	14.27674
34	4.08574	0.00000	8.15004	134	4.07188	-2.08173	14.31751
35	6.06144	-2.06317	8.16785	135	6.06144	-4.06793	14.29895
36	-4.08708	4.08708	8.14869	136	-6.06144	4.06793	14.29895
37	-2.08173	2.08173	8.16390	137	-4.07188	2.08173	14.31751
38	0.00000	0.00000	8.25826	138	-2.04097	0.00000	14.27674
39	2.08173	-2.08173	8.16390	139	0.00000	-2.04097	14.27674
40	4.08708	-4.08708	8.14869	140	2.08173	-4.07188	14.31751
41	-6.06144	2.06317	8.16785	141	4.06793	-6.06144	14.29895
42	-4.08574	0.00000	8.15004	142	-7.90035	1.96544	14.20122
43	-2.08173	-2.08173	8.16390	143	-5.99218	0.00000	14.25564
44	0.00000	-4.08574	8.15004	144	-4.07188	-2.08173	14.31751
45	2.06317	-6.06144	8.16785	145	-2.08173	-4.07188	14.31751
46	-7.80939	0.00000	8.30923	146	0.00000	-5.99218	14.25564
47	-6.06144	-2.06317	8.16785	147	1.96544	-7.90035	14.20122
48	-4.08708	-4.08708	8.14869	148	-7.90035	-1.96544	14.20122
49	-2.06317	-6.06144	8.16785	149	-6.06144	-4.06793	14.29895
50	0.00000	-7.80939	8.30923	150	-4.06793	-6.06144	14.29895
51	1.96544	7.90035	10.2703	151	-1.96544	-7.90035	14.20122
52	4.06793	6.06144	10.1726	152	0.00000	7.80939	16.16232
53	6.06144	4.06793	10.1726	153	2.06317	6.06144	16.30371
54	7.90035	1.96544	10.2703	154	4.08708	4.08708	16.32286
55	-1.96544	7.90035	10.2703	155	6.06144	2.06317	16.30371
56	0.00000	5.99218	10.2159	156	7.80939	0.00000	16.16232
57	2.08173	4.07188	10.1540	157	-2.06317	6.06144	16.30371
58	4.07188	2.08173	10.1540	158	0.00000	4.08574	16.32152
59	5.99218	0.00000	10.2159	159	2.08173	2.08173	16.30765
60	7.90035	-1.96544	10.2703	160	4.08574	0.00000	16.32152
61	-4.06793	6.06144	10.1726	161	6.06144	-2.06317	16.30371
62	-2.08173	4.07188	10.1540	162	-4.08708	4.08708	16.32286
63	0.00000	2.04097	10.1948	163	-2.08173	2.08173	16.30765
64	2.04097	0.00000	10.1948	164	0.00000	0.00000	16.21329
65	4.07188	-2.08173	10.1540	165	2.08173	-2.08173	16.30765
66	6.06144	-4.06793	10.1726	166	4.08708	-4.08708	16.32286
67	-6.06144	4.06793	10.1726	167	-6.06144	2.06317	16.30371

68	-4.07188	2.08173	10.1540	168	-4.08574	0.00000	16.32152
69	-2.04097	0.00000	10.1948	169	-2.08173	-2.08173	16.30765
70	0.00000	-2.04097	10.1948	170	0.00000	-4.08574	16.32152
71	2.08173	-4.07188	10.1540	171	2.06317	-6.06144	16.30371
72	4.06793	-6.06144	10.1726	172	-7.80939	0.00000	16.16232
73	-7.90035	1.96544	10.2703	173	-6.06144	-2.06317	16.30371
74	-5.99218	0.00000	10.2159	174	-4.08708	-4.08708	16.32286
75	-4.07188	-2.08173	10.1540	175	-2.06317	-6.06144	16.30371
76	-2.08173	-4.07188	10.1540	176	0.00000	-7.80939	16.16232
77	0.00000	-5.99218	10.2159	177	0.00000	5.96278	18.19856
78	1.96544	-7.90035	10.2703	178	2.06317	4.06793	18.29721
79	-7.90035	-1.96544	10.2703	179	4.06793	2.06317	18.29721
80	-6.06144	-4.06793	10.1726	180	5.96278	0.00000	18.19856
81	-4.06793	-6.06144	10.1726	181	-2.06317	4.06793	18.29721
82	-1.96544	-7.90035	10.2703	182	0.00000	2.01986	18.22796
83	3.92655	7.80939	12.2357	183	2.01986	0.00000	18.22796
84	5.96278	5.96278	12.2357	184	4.06793	-2.06317	18.29721
85	7.80939	3.92655	12.2357	185	-4.06793	2.06317	18.29721
86	0.00000	7.99990	12.2357	186	-2.01986	0.00000	18.22796
87	2.01986	5.99218	12.2357	187	0.00000	-2.01986	18.22796
88	4.08574	4.08574	12.2357	188	2.06317	-4.06793	18.29721
89	5.99218	2.01986	12.2357	189	-5.96278	0.00000	18.19856
90	7.99990	0.00000	12.2357	190	-4.06793	-2.06317	18.29721
91	-3.92655	7.80939	12.2357	191	-2.06317	-4.06793	18.29721
92	-2.01986	5.99218	12.2357	192	0.00000	-5.96278	18.19856
93	0.00000	3.97751	12.2357	193	0.00000	3.92655	20.04516
94	2.04097	2.04097	12.2357	194	1.96544	1.96544	20.13613
95	3.97751	0.00000	12.2357	195	3.92655	0.00000	20.04516
96	5.99218	-2.01986	12.2357	196	-1.96544	1.96544	20.13613
97	7.80939	-3.92655	12.2357	197	0.00000	0.00000	20.23568
98	-5.96278	5.96278	12.2357	198	1.96544	-1.96544	20.13613
99	-4.08574	4.08574	12.2357	199	-3.92655	0.00000	20.04516
100	-2.04097	2.04097	12.2357	200	-1.96544	-1.96544	20.13613
				201	0.00000	-3.92655	20.04516

B.4 Coordinates for a 202 atom Au cluster with TO structure

This structure was used to match an orientation to the cluster depicted in Fig. 5.4.

atom	x	y	z	atom	x	y	z
1	1.58008	-1.80439	-8.40546	102	1.56511	-1.79335	1.63261
2	3.09712	-3.58455	-6.90654	103	3.13314	-3.59004	3.26827
3	4.59114	-5.25456	-5.26454	104	4.57254	-5.23935	4.76975
4	-0.72942	-3.18365	-7.71192	105	-6.79084	3.84617	-3.93647
5	0.78757	-4.97252	-6.21709	106	-5.41581	2.17993	-2.42961
6	2.28496	-6.63763	-4.56753	107	-3.87194	0.40566	-0.81494
7	-3.05351	-4.45364	-6.87353	108	-2.40848	-1.37704	0.79628
8	-1.54158	-6.23673	-5.37292	109	-0.82180	-3.08929	2.36676
9	-0.04245	-7.90381	-3.73261	110	0.72820	-4.86006	3.97940
10	1.81900	0.92493	-8.18201	111	2.20882	-6.46593	5.45135
11	3.44562	-0.81852	-6.70846	112	-7.78757	0.81589	-1.63907
12	4.98296	-2.58006	-5.10481	113	-6.25046	-0.95768	-0.02583
13	6.39153	-4.31443	-3.41226	114	-4.82145	-2.75666	1.59404
14	-0.57120	-0.39769	-7.55389	115	-3.20430	-4.44806	3.15171
15	1.00724	-2.15577	-5.85869	116	-1.65287	-6.21344	4.76022
16	2.55617	-3.93058	-4.24296	117	-8.41338	-2.25325	0.73639
17	4.13042	-5.78494	-2.64950	118	-7.03649	-4.02310	2.32636
18	-2.93695	-1.75030	-6.77174	119	-5.43583	-5.66501	3.84236
19	-1.37634	-3.51857	-5.07064	120	3.35208	7.15733	-2.77085
20	0.17259	-5.29338	-3.45491	121	5.00920	5.57539	-1.16991
21	1.76466	-7.13756	-1.86735	122	6.53792	3.82374	0.42474
22	-5.21749	-3.09817	-5.85564	123	7.90325	1.94246	1.97661
23	-3.78950	-4.95519	-4.31643	124	-0.47447	7.55823	-3.57624
24	-2.25216	-6.71672	-2.71278	125	1.03920	5.90956	-1.99582
25	-0.64496	-8.33753	-1.08589	126	2.66283	4.24422	-0.37858
26	2.00006	3.62484	-7.69835	127	4.18897	2.49553	1.21338
27	3.66125	1.96892	-6.34542	128	5.63429	0.64437	2.79745
28	5.22540	0.21715	-4.77082	129	7.09108	-1.11061	4.31561
29	6.72730	-1.54426	-3.14712	130	-2.91071	6.40514	-2.83684
30	7.98867	-3.23709	-1.45146	131	-1.39013	4.66884	-1.23161
31	-0.35557	2.38976	-7.19085	132	0.22076	2.85380	0.37168

32	1.24639	0.63377	-5.60637	133	1.78587	1.06046	2.00430
33	2.85745	-1.12642	-3.97663	134	3.32875	-0.73819	3.69079
34	4.37953	-2.95628	-2.33810	135	4.85696	-2.49530	5.26585
35	5.87476	-4.74914	-0.69181	136	-5.26319	5.06012	-2.05908
36	-2.73180	1.05081	-6.44560	137	-3.73863	3.32609	-0.45516
37	-1.19551	-0.70180	-4.82966	138	-2.18772	1.47676	1.16796
38	0.39158	-2.47231	-3.09111	139	-0.62261	-0.31659	2.80057
39	1.99724	-4.36014	-1.49922	140	0.98024	-2.08095	4.46724
40	3.53653	-6.13164	0.09308	141	2.50448	-3.84032	6.04361
41	-5.07380	-0.30788	-5.63094	142	-7.47807	3.55393	-1.26075
42	-3.57506	-2.12289	-4.01233	143	-6.03199	1.86662	0.34201
43	-2.05572	-3.93552	-2.35226	144	-4.59885	0.09237	2.02224
44	-0.44193	-5.71293	-0.74406	145	-3.07272	-1.65632	3.61420
45	1.15653	-7.44678	0.86810	146	-1.43690	-3.39857	5.13528
46	-7.21555	-1.64417	-4.65154	147	0.08748	-5.11491	6.63110
47	-5.92635	-3.51277	-3.17563	148	-8.29023	0.50086	1.07826
48	-4.42067	-5.29798	-1.58169	149	-6.94415	-1.25892	2.78203
49	-2.86029	-7.02595	0.02267	150	-5.41543	-3.01057	4.37668
50	-1.22695	-8.50610	1.59535	151	-3.73906	-4.71401	5.82572
51	3.73906	4.71401	-5.82572	152	1.22695	8.50610	-1.59535
52	5.41543	3.01057	-4.37668	153	2.86029	7.02595	-0.02267
53	6.94415	1.25892	-2.78203	154	4.42067	5.29798	1.58169
54	8.29023	-0.50086	-1.07826	155	5.92635	3.51277	3.17563
55	-0.08748	5.11491	-6.63110	156	7.21555	1.64417	4.65154
56	1.43690	3.39857	-5.13528	157	-1.15653	7.44678	-0.86810
57	3.07272	1.65632	-3.61420	158	0.44193	5.71293	0.74406
58	4.59885	-0.09237	-2.02224	159	2.05572	3.93552	2.35226
59	6.03199	-1.86662	-0.34201	160	3.57506	2.12289	4.01233
60	7.47807	-3.55393	1.26075	161	5.07380	0.30788	5.63094
61	-2.50448	3.84032	-6.04361	162	-3.53653	6.13164	-0.09308
62	-0.98024	2.08095	-4.46724	163	-1.99724	4.36014	1.49922
63	0.62261	0.31659	-2.80057	164	-0.39158	2.47231	3.09111
64	2.18772	-1.47676	-1.16796	165	1.19551	0.70180	4.82966
65	3.73863	-3.32609	0.45516	166	2.73180	-1.05081	6.44560
66	5.26319	-5.06012	2.05908	167	-5.87476	4.74914	0.69181

67	-4.85696	2.49530	-5.26585	168	-4.37953	2.95628	2.33810
68	-3.32875	0.73819	-3.69079	169	-2.85745	1.12642	3.97663
69	-1.78587	-1.06046	-2.00430	170	-1.24639	-0.63377	5.60637
70	-0.22076	-2.85380	-0.37168	171	0.35557	-2.38976	7.19085
71	1.39013	-4.66884	1.23161	172	-7.98867	3.23709	1.45146
72	2.91071	-6.40514	2.83684	173	-6.72730	1.54426	3.14712
73	-7.09108	1.11061	-4.31561	174	-5.22540	-0.21715	4.77082
74	-5.63429	-0.64437	-2.79745	175	-3.66125	-1.96892	6.34542
75	-4.18897	-2.49553	-1.21338	176	-2.00006	-3.62484	7.69835
76	-2.66283	-4.24422	0.37858	177	0.64496	8.33753	1.08589
77	-1.03920	-5.90956	1.99582	178	2.25216	6.71672	2.71278
78	0.47447	-7.55823	3.57624	179	3.78950	4.95519	4.31643
79	-7.90325	-1.94246	-1.97661	180	5.21749	3.09817	5.85564
80	-6.53792	-3.82374	-0.42474	181	-1.76466	7.13756	1.86735
81	-5.00920	-5.57539	1.16991	182	-0.17259	5.29338	3.45491
82	-3.35208	-7.15733	2.77085	183	1.37634	3.51857	5.07064
83	5.43583	5.66501	-3.84236	184	2.93695	1.75030	6.77174
84	7.03649	4.02310	-2.32636	185	-4.13042	5.78494	2.64950
85	8.41338	2.25325	-0.73639	186	-2.55617	3.93058	4.24296
86	1.65287	6.21344	-4.76022	187	-1.00724	2.15577	5.85869
87	3.20430	4.44806	-3.15171	188	0.57120	0.39769	7.55389
88	4.82145	2.75666	-1.59404	189	-6.39153	4.31443	3.41226
89	6.25046	0.95768	0.02583	190	-4.98296	2.58006	5.10481
90	7.78757	-0.81589	1.63907	191	-3.44562	0.81852	6.70846
91	-2.20882	6.46593	-5.45135	192	-1.81900	-0.92493	8.18201
92	-0.72820	4.86006	-3.97940	193	0.04245	7.90381	3.73261
93	0.82180	3.08929	-2.36676	194	1.54158	6.23673	5.37292
94	2.40848	1.37704	-0.79628	195	3.05351	4.45364	6.87353
95	3.87194	-0.40566	0.81494	196	-2.28496	6.63763	4.56753
96	5.41581	-2.17993	2.42961	197	-0.78757	4.97252	6.21709
97	6.79084	-3.84617	3.93647	198	0.72942	3.18365	7.71192
98	-4.57254	5.23935	-4.76975	199	-4.59114	5.25456	5.26454
99	-3.13314	3.59004	-3.26827	200	-3.09712	3.58455	6.90654
100	-1.56511	1.79335	-1.63261	201	-1.58008	1.80439	8.40546
101	0.00000	0.00000	0.00000	202	-7.33776	1.22629	5.88927

B.5 Coordinates for a 309 atom Au cluster with Ih structure

atom	x	y	z	atom	x	y	z
1	0.00000	0.00000	0.00000	155	6.23912	3.85666	5.32945
2	1.43352	2.31934	0.00000	156	3.85666	5.32945	6.23912
3	-1.43352	2.31934	0.00000	157	7.71310	4.76577	0.00000
4	-1.43352	-2.31934	0.00000	158	8.62275	2.38341	1.47274
5	1.43352	-2.31934	0.00000	159	8.62275	2.38341	-1.47274
6	2.31934	0.00000	1.43352	160	5.32945	6.23912	-3.85666
7	-2.31934	0.00000	1.43352	161	6.23912	3.85666	-5.32945
8	-2.31934	0.00000	-1.4335	162	3.85666	5.32945	-6.23912
9	2.31934	0.00000	-1.4335	163	-1.47274	-8.62275	2.38341
10	0.00000	1.43352	2.31934	164	1.47274	-8.62275	2.38341
11	0.00000	-1.43352	2.31934	165	0.00000	-7.71310	4.76577
12	0.00000	-1.43352	-2.3193	166	-1.47274	-8.62275	-2.38341
13	0.00000	1.43352	-2.3193	167	1.47274	-8.62275	-2.38341
14	4.72213	0.00000	0.00000	168	0.00000	-7.71310	-4.76577
15	-4.72213	0.00000	0.00000	169	-5.32945	-6.23912	3.85666
16	0.00000	4.72213	0.00000	170	-6.23912	-3.85666	5.32945
17	0.00000	-4.72213	0.00000	171	-3.85666	-5.32945	6.23912
18	0.00000	0.00000	4.72213	172	-7.71310	-4.76577	0.00000
19	0.00000	0.00000	-4.7221	173	-8.62275	-2.38341	1.47274
20	3.82045	2.36105	1.45931	174	-8.62275	-2.38341	-1.47274
21	-3.82045	2.36105	1.45931	175	-5.32945	-6.23912	-3.85666
22	-3.82045	-2.36105	1.45931	176	-6.23912	-3.85666	-5.32945
23	3.82045	-2.36105	1.45931	177	-3.85666	-5.32945	-6.23912
24	3.82045	2.36105	-1.4593	178	4.76577	0.00000	7.71310
25	-3.82045	2.36105	-1.4593	179	2.38341	1.47274	8.62275
26	-3.82045	-2.36105	-1.4593	180	2.38341	-1.47274	8.62275
27	3.82045	-2.36105	-1.4593	181	-2.38341	-1.47274	8.62275
28	1.45931	3.82045	2.36105	182	-2.38341	1.47274	8.62275
29	-1.45931	3.82045	2.36105	183	-4.76577	0.00000	7.71310
30	-1.45931	-3.82045	2.36105	184	-6.23912	3.85666	5.32945
31	1.45931	-3.82045	2.36105	185	-3.85666	5.32945	6.23912
32	1.45931	3.82045	-2.3610	186	-5.32945	6.23912	3.85666

33	-1.45931	3.82045	-2.3610	187	-8.62275	2.38341	1.47274
34	-1.45931	-3.82045	-2.3610	188	-7.71310	4.76577	0.00000
35	1.45931	-3.82045	-2.3610	189	-8.62275	2.38341	-1.47274
36	2.36105	1.45931	3.82045	190	-5.32945	6.23912	-3.85666
37	-2.36105	1.45931	3.82045	191	-6.23912	3.85666	-5.32945
38	-2.36105	-1.45931	3.82045	192	-3.85666	5.32945	-6.23912
39	2.36105	-1.45931	3.82045	193	-4.76577	0.00000	-7.71310
40	2.36105	1.45931	-3.8204	194	-2.38341	1.47274	-8.62275
41	-2.36105	1.45931	-3.8204	195	-2.38341	-1.47274	-8.62275
42	-2.36105	-1.45931	-3.8204	196	2.38341	1.47274	-8.62275
43	2.36105	-1.45931	-3.8204	197	2.38341	-1.47274	-8.62275
44	2.86275	4.63149	0.00000	198	4.76577	0.00000	-7.71310
45	-2.86275	4.63149	0.00000	199	3.85666	-5.32945	-6.23912
46	-2.86275	-4.63149	0.00000	200	6.23912	-3.85666	-5.32945
47	2.86275	-4.63149	0.00000	201	5.32945	-6.23912	-3.85666
48	4.63149	0.00000	2.86275	202	8.62275	-2.38341	-1.47274
49	-4.63149	0.00000	2.86275	203	7.71310	-4.76577	0.00000
50	-4.63149	0.00000	-2.8627	204	8.62275	-2.38341	1.47274
51	4.63149	0.00000	-2.8627	205	5.32945	-6.23912	3.85666
52	0.00000	2.86275	4.63149	206	6.23912	-3.85666	5.32945
53	0.00000	-2.86275	4.63149	207	3.85666	-5.32945	6.23912
54	0.00000	-2.86275	-4.6314	208	2.90823	9.34783	0.00000
55	0.00000	2.86275	-4.6314	209	0.00000	9.36847	0.00000
56	0.00000	6.30532	-2.4081	210	-2.90823	9.34783	0.00000
57	3.89686	3.89686	-3.8968	211	6.66490	7.02620	1.43489
58	6.30532	2.40819	0.00000	212	7.57984	4.68423	2.89538
59	3.89686	3.89686	3.89686	213	8.46124	2.32161	4.34318
60	0.00000	6.30532	2.40819	214	6.66490	7.02620	-1.43489
61	-2.40819	0.00000	6.30532	215	7.57984	4.68423	-2.89538
62	2.40819	0.00000	6.30532	216	8.46124	2.32161	-4.34318
63	3.89686	-3.89686	3.89686	217	4.34318	8.46124	2.32161
64	6.30532	-2.40819	0.00000	218	2.89538	7.57984	4.68423
65	3.89686	-3.89686	-3.8968	219	1.43489	6.66490	7.02620
66	2.40819	0.00000	-6.3053	220	4.34318	8.46124	-2.32161
67	-2.40819	0.00000	-6.3053	221	2.89538	7.57984	-4.68423

68	-3.89686	3.89686	-3.8968	222	1.43489	6.66490	-7.02620
69	-6.30532	2.40819	0.00000	223	2.90823	-9.34783	0.00000
70	-3.89686	3.89686	3.89686	224	0.00000	-9.36847	0.00000
71	-3.89686	-3.89686	3.89686	225	-2.90823	-9.34783	0.00000
72	0.00000	-6.30532	2.40819	226	6.66490	-7.02620	1.43489
73	0.00000	-6.30532	-2.4081	227	7.57984	-4.68423	2.89538
74	-3.89686	-3.89686	-3.8968	228	8.46124	-2.32161	4.34318
75	-6.30532	-2.40819	0.00000	229	6.66490	-7.02620	-1.43489
76	5.30177	4.71989	1.47359	230	7.57984	-4.68423	-2.89538
77	6.19363	2.38416	2.91744	231	8.46124	-2.32161	-4.34318
78	5.30177	4.71989	-1.4735	232	4.34318	-8.46124	2.32161
79	6.19363	2.38416	-2.9174	233	2.89538	-7.57984	4.68423
80	2.91744	6.19363	2.38416	234	1.43489	-6.66490	7.02620
81	1.47359	5.30177	4.71989	235	4.34318	-8.46124	-2.32161
82	2.91744	6.19363	-2.3841	236	2.89538	-7.57984	-4.68423
83	1.47359	5.30177	-4.7198	237	1.43489	-6.66490	-7.02620
84	1.44385	7.10411	0.00000	238	-6.66490	7.02620	1.43489
85	-1.44385	7.10411	0.00000	239	-7.57984	4.68423	2.89538
86	5.30177	-4.71989	1.47359	240	-8.46124	2.32161	4.34318
87	6.19363	-2.38416	2.91744	241	-6.66490	7.02620	-1.43489
88	5.30177	-4.71989	-1.4735	242	-7.57984	4.68423	-2.89538
89	6.19363	-2.38416	-2.9174	243	-8.46124	2.32161	-4.34318
90	2.91744	-6.19363	2.38416	244	-4.34318	8.46124	2.32161
91	1.47359	-5.30177	4.71989	245	-2.89538	7.57984	4.68423
92	2.91744	-6.19363	-2.3841	246	-1.43489	6.66490	7.02620
93	1.47359	-5.30177	-4.7198	247	-4.34318	8.46124	-2.32161
94	1.44385	-7.10411	0.00000	248	-2.89538	7.57984	-4.68423
95	-1.44385	-7.10411	0.00000	249	-1.43489	6.66490	-7.02620
96	-5.30177	4.71989	1.47359	250	-6.66490	-7.02620	1.43489
97	-6.19363	2.38416	2.91744	251	-7.57984	-4.68423	2.89538
98	-5.30177	4.71989	-1.4735	252	-8.46124	-2.32161	4.34318
99	-6.19363	2.38416	-2.9174	253	-6.66490	-7.02620	-1.43489
100	-2.91744	6.19363	2.38416	254	-7.57984	-4.68423	-2.89538
101	-1.47359	5.30177	4.71989	255	-8.46124	-2.32161	-4.34318
102	-2.91744	6.19363	-2.3841	256	-4.34318	-8.46124	2.32161

103	-1.47359	5.30177	-4.7198	257	-2.89538	-7.57984	4.68423
104	-5.30177	-4.71989	1.47359	258	-1.43489	-6.66490	7.02620
105	-6.19363	-2.38416	2.91744	259	-4.34318	-8.46124	-2.32161
106	-5.30177	-4.71989	-1.4735	260	-2.89538	-7.57984	-4.68423
107	-6.19363	-2.38416	-2.9174	261	-1.43489	-6.66490	-7.02620
108	-2.91744	-6.19363	2.38416	262	9.34783	0.00000	2.90823
109	-1.47359	-5.30177	4.71989	263	9.36847	0.00000	0.00000
110	-2.91744	-6.19363	-2.3841	264	9.34783	0.00000	-2.90823
111	-1.47359	-5.30177	-4.7198	265	7.02620	1.43489	6.66490
112	4.71989	1.47359	5.30177	266	4.68423	2.89538	7.57984
113	2.38416	2.91744	6.19363	267	2.32161	4.34318	8.46124
114	4.71989	-1.47359	5.30177	268	7.02620	-1.43489	6.66490
115	2.38416	-2.91744	6.19363	269	4.68423	-2.89538	7.57984
116	7.10411	0.00000	1.44385	270	2.32161	-4.34318	8.46124
117	7.10411	0.00000	-1.4438	271	7.02620	1.43489	-6.66490
118	4.71989	1.47359	-5.3017	272	4.68423	2.89538	-7.57984
119	2.38416	2.91744	-6.1936	273	2.32161	4.34318	-8.46124
120	4.71989	-1.47359	-5.3017	274	7.02620	-1.43489	-6.66490
121	2.38416	-2.91744	-6.1936	275	4.68423	-2.89538	-7.57984
122	-4.71989	1.47359	5.30177	276	2.32161	-4.34318	-8.46124
123	-2.38416	2.91744	6.19363	277	-9.34783	0.00000	2.90823
124	-4.71989	-1.47359	5.30177	278	-9.36847	0.00000	0.00000
125	-2.38416	-2.91744	6.19363	279	-9.34783	0.00000	-2.90823
126	-7.10411	0.00000	1.44385	280	-7.02620	1.43489	6.66490
127	-7.10411	0.00000	-1.4438	281	-4.68423	2.89538	7.57984
128	-4.71989	1.47359	-5.3017	282	-2.32161	4.34318	8.46124
129	-2.38416	2.91744	-6.1936	283	-7.02620	-1.43489	6.66490
130	-4.71989	-1.47359	-5.3017	284	-4.68423	-2.89538	7.57984
131	-2.38416	-2.91744	-6.1936	285	-2.32161	-4.34318	8.46124
132	0.00000	1.44385	7.10411	286	-7.02620	1.43489	-6.66490
133	0.00000	-1.44385	7.10411	287	-4.68423	2.89538	-7.57984
134	0.00000	1.44385	-7.1041	288	-2.32161	4.34318	-8.46124
135	0.00000	-1.44385	-7.1041	289	-7.02620	-1.43489	-6.66490
136	4.30661	6.96714	0.00000	290	-4.68423	-2.89538	-7.57984
137	4.30661	-6.96714	0.00000	291	-2.32161	-4.34318	-8.46124

138	-4.30661	6.96714	0.00000	292	0.00000	2.90823	9.34783
139	-4.30661	-6.96714	0.00000	293	0.00000	0.00000	9.36847
140	6.96714	0.00000	4.30661	294	0.00000	-2.90823	9.34783
141	6.96714	0.00000	-4.3066	295	0.00000	2.90823	-9.34783
142	-6.96714	0.00000	4.30661	296	0.00000	0.00000	-9.36847
143	-6.96714	0.00000	-4.3066	297	0.00000	-2.90823	-9.34783
144	0.00000	4.30661	6.96714	298	5.66933	9.17171	0.00000
145	0.00000	4.30661	-6.9671	299	5.66933	-9.17171	0.00000
146	0.00000	-4.30661	6.96713	300	-5.66933	9.17171	0.00000
147	0.00000	-4.30661	-6.9671	301	-5.66933	-9.17171	0.00000
148	1.47274	8.62275	2.38341	302	9.17171	0.00000	5.66933
149	-1.47274	8.62275	2.38341	303	9.17171	0.00000	-5.66933
150	0.00000	7.71310	4.76576	304	-9.17171	0.00000	5.66933
151	1.47274	8.62275	-2.3834	305	-9.17171	0.00000	-5.66933
152	-1.47274	8.62275	-2.3834	306	0.00000	5.66933	9.17171
153	0.00000	7.71310	-4.7657	307	0.00000	5.66933	-9.17171
154	5.32945	6.23912	3.85666	308	0.00000	-5.66933	9.17171
				309	0.00000	-5.66933	-9.17171

Appendix C: Carbon Nanotube Coordinates

These coordinates assume a C-C bond length of 1.4\AA . They are raw coordinates, and do not represent a relaxed structure.

C.1 Coordinates for a section of a (10,10) buckytube

atom	x	y	z	atom	x	y	z
1	6.68451	0.00000	1.21244	201	6.68451	0.00000	13.33679
2	6.64789	0.69872	0.00000	202	6.64789	0.69872	12.12436
3	6.35734	2.06563	0.00000	203	6.35734	2.06563	12.12436
4	6.10660	2.71883	1.21244	204	6.10660	2.71883	13.33679
5	5.40788	3.92905	1.21244	205	5.40788	3.92905	13.33679
6	4.96756	4.47281	0.00000	206	4.96756	4.47281	12.12436
7	3.92905	5.40788	0.00000	207	3.92905	5.40788	12.12436
8	3.34225	5.78895	1.21244	208	3.34225	5.78895	13.33679
9	2.06563	6.35734	1.21244	209	2.06563	6.35734	13.33679
10	1.38979	6.53844	0.00000	210	1.38979	6.53844	12.12436
11	0.00000	6.68451	0.00000	211	0.00000	6.68451	12.12436
12	-0.69872	6.64789	1.21244	212	-0.69872	6.64789	13.33679
13	-2.06563	6.35734	1.21244	213	-2.06563	6.35734	13.33679
14	-2.71883	6.10660	0.00000	214	-2.71883	6.10660	12.12436
15	-3.92905	5.40788	0.00000	215	-3.92905	5.40788	12.12436
16	-4.47281	4.96756	1.21244	216	-4.47281	4.96756	13.33679
17	-5.40788	3.92905	1.21244	217	-5.40788	3.92905	13.33679
18	-5.78895	3.34225	0.00000	218	-5.78895	3.34225	12.12436
19	-6.35734	2.06563	0.00000	219	-6.35734	2.06563	12.12436
20	-6.53844	1.38979	1.21244	220	-6.53844	1.38979	13.33679
21	-6.68451	0.00000	1.21244	221	-6.68451	0.00000	13.33679
22	-6.64789	-0.69872	0.00000	222	-6.64789	-0.69872	12.12436
23	-6.35734	-2.06563	0.00000	223	-6.35734	-2.06563	12.12436
24	-6.10660	-2.71883	1.21244	224	-6.10660	-2.71883	13.33679
25	-5.40788	-3.92905	1.21244	225	-5.40788	-3.92905	13.33679
26	-4.96756	-4.47281	0.00000	226	-4.96756	-4.47281	12.12436
27	-3.92905	-5.40788	0.00000	227	-3.92905	-5.40788	12.12436

28	-3.34225	-5.78895	1.21244	228	-3.34225	-5.78895	13.33679
29	-2.06563	-6.35734	1.21244	229	-2.06563	-6.35734	13.33679
30	-1.38979	-6.53844	0.00000	230	-1.38979	-6.53844	12.12436
31	0.00000	-6.68451	0.00000	231	0.00000	-6.68451	12.12436
32	0.69872	-6.64789	1.21244	232	0.69872	-6.64789	13.33679
33	2.06563	-6.35734	1.21244	233	2.06563	-6.35734	13.33679
34	2.71883	-6.10660	0.00000	234	2.71883	-6.10660	12.12436
35	3.92905	-5.40788	0.00000	235	3.92905	-5.40788	12.12436
36	4.47281	-4.96756	1.21244	236	4.47281	-4.96756	13.33679
37	5.40788	-3.92905	1.21244	237	5.40788	-3.92905	13.33679
38	5.78895	-3.34225	0.00000	238	5.78895	-3.34225	12.12436
39	6.35734	-2.06563	0.00000	239	6.35734	-2.06563	12.12436
40	6.53844	-1.38979	1.21244	240	6.53844	-1.38979	13.33679
41	6.68451	0.00000	3.63731	241	6.68451	0.00000	15.76166
42	6.64789	0.69872	2.42487	242	6.64789	0.69872	14.54923
43	6.35734	2.06563	2.42487	243	6.35734	2.06563	14.54923
44	6.10660	2.71883	3.63731	244	6.10660	2.71883	15.76166
45	5.40788	3.92905	3.63731	245	5.40788	3.92905	15.76166
46	4.96756	4.47281	2.42487	246	4.96756	4.47281	14.54923
47	3.92905	5.40788	2.42487	247	3.92905	5.40788	14.54923
48	3.34225	5.78895	3.63731	248	3.34225	5.78895	15.76166
49	2.06563	6.35734	3.63731	249	2.06563	6.35734	15.76166
50	1.38979	6.53844	2.42487	250	1.38979	6.53844	14.54923
51	0.00000	6.68451	2.42487	251	0.00000	6.68451	14.54923
52	-0.69872	6.64789	3.63731	252	-0.69872	6.64789	15.76166
53	-2.06563	6.35734	3.63731	253	-2.06563	6.35734	15.76166
54	-2.71883	6.10660	2.42487	254	-2.71883	6.10660	14.54923
55	-3.92905	5.40788	2.42487	255	-3.92905	5.40788	14.54923
56	-4.47281	4.96756	3.63731	256	-4.47281	4.96756	15.76166
57	-5.40788	3.92905	3.63731	257	-5.40788	3.92905	15.76166
58	-5.78895	3.34225	2.42487	258	-5.78895	3.34225	14.54923
59	-6.35734	2.06563	2.42487	259	-6.35734	2.06563	14.54923
60	-6.53844	1.38979	3.63731	260	-6.53844	1.38979	15.76166
61	-6.68451	0.00000	3.63731	261	-6.68451	0.00000	15.76166
62	-6.64789	-0.69872	2.42487	262	-6.64789	-0.69872	14.54923

63	-6.35734	-2.06563	2.42487	263	-6.35734	-2.06563	14.54923
64	-6.10660	-2.71883	3.63731	264	-6.10660	-2.71883	15.76166
65	-5.40788	-3.92905	3.63731	265	-5.40788	-3.92905	15.76166
66	-4.96756	-4.47281	2.42487	266	-4.96756	-4.47281	14.54923
67	-3.92905	-5.40788	2.42487	267	-3.92905	-5.40788	14.54923
68	-3.34225	-5.78895	3.63731	268	-3.34225	-5.78895	15.76166
69	-2.06563	-6.35734	3.63731	269	-2.06563	-6.35734	15.76166
70	-1.38979	-6.53844	2.42487	270	-1.38979	-6.53844	14.54923
71	0.00000	-6.68451	2.42487	271	0.00000	-6.68451	14.54923
72	0.69872	-6.64789	3.63731	272	0.69872	-6.64789	15.76166
73	2.06563	-6.35734	3.63731	273	2.06563	-6.35734	15.76166
74	2.71883	-6.10660	2.42487	274	2.71883	-6.10660	14.54923
75	3.92905	-5.40788	2.42487	275	3.92905	-5.40788	14.54923
76	4.47281	-4.96756	3.63731	276	4.47281	-4.96756	15.76166
77	5.40788	-3.92905	3.63731	277	5.40788	-3.92905	15.76166
78	5.78895	-3.34225	2.42487	278	5.78895	-3.34225	14.54923
79	6.35734	-2.06563	2.42487	279	6.35734	-2.06563	14.54923
80	6.53844	-1.38979	3.63731	280	6.53844	-1.38979	15.76166
81	6.68451	0.00000	6.06218	281	6.68451	0.00000	18.18653
82	6.64789	0.69872	4.84974	282	6.64789	0.69872	16.97410
83	6.35734	2.06563	4.84974	283	6.35734	2.06563	16.97410
84	6.10660	2.71883	6.06218	284	6.10660	2.71883	18.18653
85	5.40788	3.92905	6.06218	285	5.40788	3.92905	18.18653
86	4.96756	4.47281	4.84974	286	4.96756	4.47281	16.97410
87	3.92905	5.40788	4.84974	287	3.92905	5.40788	16.97410
88	3.34225	5.78895	6.06218	288	3.34225	5.78895	18.18653
89	2.06563	6.35734	6.06218	289	2.06563	6.35734	18.18653
90	1.38979	6.53844	4.84974	290	1.38979	6.53844	16.97410
91	0.00000	6.68451	4.84974	291	0.00000	6.68451	16.97410
92	-0.69872	6.64789	6.06218	292	-0.69872	6.64789	18.18653
93	-2.06563	6.35734	6.06218	293	-2.06563	6.35734	18.18653
94	-2.71883	6.10660	4.84974	294	-2.71883	6.10660	16.97410
95	-3.92905	5.40788	4.84974	295	-3.92905	5.40788	16.97410
96	-4.47281	4.96756	6.06218	296	-4.47281	4.96756	18.18653
97	-5.40788	3.92905	6.06218	297	-5.40788	3.92905	18.18653

98	-5.78895	3.34225	4.84974	298	-5.78895	3.34225	16.97410
99	-6.35734	2.06563	4.84974	299	-6.35734	2.06563	16.97410
100	-6.53844	1.38979	6.06218	300	-6.53844	1.38979	18.18653
101	-6.68451	0.00000	6.06218	301	-6.68451	0.00000	18.18653
102	-6.64789	-0.69872	4.84974	302	-6.64789	-0.69872	16.97410
103	-6.35734	-2.06563	4.84974	303	-6.35734	-2.06563	16.97410
104	-6.10660	-2.71883	6.06218	304	-6.10660	-2.71883	18.18653
105	-5.40788	-3.92905	6.06218	305	-5.40788	-3.92905	18.18653
106	-4.96756	-4.47281	4.84974	306	-4.96756	-4.47281	16.97410
107	-3.92905	-5.40788	4.84974	307	-3.92905	-5.40788	16.97410
108	-3.34225	-5.78895	6.06218	308	-3.34225	-5.78895	18.18653
109	-2.06563	-6.35734	6.06218	309	-2.06563	-6.35734	18.18653
110	-1.38979	-6.53844	4.84974	310	-1.38979	-6.53844	16.97410
111	0.00000	-6.68451	4.84974	311	0.00000	-6.68451	16.97410
112	0.69872	-6.64789	6.06218	312	0.69872	-6.64789	18.18653
113	2.06563	-6.35734	6.06218	313	2.06563	-6.35734	18.18653
114	2.71883	-6.10660	4.84974	314	2.71883	-6.10660	16.97410
115	3.92905	-5.40788	4.84974	315	3.92905	-5.40788	16.97410
116	4.47281	-4.96756	6.06218	316	4.47281	-4.96756	18.18653
117	5.40788	-3.92905	6.06218	317	5.40788	-3.92905	18.18653
118	5.78895	-3.34225	4.84974	318	5.78895	-3.34225	16.97410
119	6.35734	-2.06563	4.84974	319	6.35734	-2.06563	16.97410
120	6.53844	-1.38979	6.06218	320	6.53844	-1.38979	18.18653
121	6.68451	0.00000	8.48705	321	6.68451	0.00000	20.61140
122	6.64789	0.69872	7.27461	322	6.64789	0.69872	19.39897
123	6.35734	2.06563	7.27461	323	6.35734	2.06563	19.39897
124	6.10660	2.71883	8.48705	324	6.10660	2.71883	20.61140
125	5.40788	3.92905	8.48705	325	5.40788	3.92905	20.61140
126	4.96756	4.47281	7.27461	326	4.96756	4.47281	19.39897
127	3.92905	5.40788	7.27461	327	3.92905	5.40788	19.39897
128	3.34225	5.78895	8.48705	328	3.34225	5.78895	20.61140
129	2.06563	6.35734	8.48705	329	2.06563	6.35734	20.61140
130	1.38979	6.53844	7.27461	330	1.38979	6.53844	19.39897
131	0.00000	6.68451	7.27461	331	0.00000	6.68451	19.39897
132	-0.69872	6.64789	8.48705	332	-0.69872	6.64789	20.61140

133	-2.06563	6.35734	8.48705	333	-2.06563	6.35734	20.61140
134	-2.71883	6.10660	7.27461	334	-2.71883	6.10660	19.39897
135	-3.92905	5.40788	7.27461	335	-3.92905	5.40788	19.39897
136	-4.47281	4.96756	8.48705	336	-4.47281	4.96756	20.61140
137	-5.40788	3.92905	8.48705	337	-5.40788	3.92905	20.61140
138	-5.78895	3.34225	7.27461	338	-5.78895	3.34225	19.39897
139	-6.35734	2.06563	7.27461	339	-6.35734	2.06563	19.39897
140	-6.53844	1.38979	8.48705	340	-6.53844	1.38979	20.61140
141	-6.68451	0.00000	8.48705	341	-6.68451	0.00000	20.61140
142	-6.64789	-0.69872	7.27461	342	-6.64789	-0.69872	19.39897
143	-6.35734	-2.06563	7.27461	343	-6.35734	-2.06563	19.39897
144	-6.10660	-2.71883	8.48705	344	-6.10660	-2.71883	20.61140
145	-5.40788	-3.92905	8.48705	345	-5.40788	-3.92905	20.61140
146	-4.96756	-4.47281	7.27461	346	-4.96756	-4.47281	19.39897
147	-3.92905	-5.40788	7.27461	347	-3.92905	-5.40788	19.39897
148	-3.34225	-5.78895	8.48705	348	-3.34225	-5.78895	20.61140
149	-2.06563	-6.35734	8.48705	349	-2.06563	-6.35734	20.61140
150	-1.38979	-6.53844	7.27461	350	-1.38979	-6.53844	19.39897
151	0.00000	-6.68451	7.27461	351	0.00000	-6.68451	19.39897
152	0.69872	-6.64789	8.48705	352	0.69872	-6.64789	20.61140
153	2.06563	-6.35734	8.48705	353	2.06563	-6.35734	20.61140
154	2.71883	-6.10660	7.27461	354	2.71883	-6.10660	19.39897
155	3.92905	-5.40788	7.27461	355	3.92905	-5.40788	19.39897
156	4.47281	-4.96756	8.48705	356	4.47281	-4.96756	20.61140
157	5.40788	-3.92905	8.48705	357	5.40788	-3.92905	20.61140
158	5.78895	-3.34225	7.27461	358	5.78895	-3.34225	19.39897
159	6.35734	-2.06563	7.27461	359	6.35734	-2.06563	19.39897
160	6.53844	-1.38979	8.48705	360	6.53844	-1.38979	20.61140
161	6.68451	0.00000	10.9119	361	6.68451	0.00000	23.03628
162	6.64789	0.69872	9.69948	362	6.64789	0.69872	21.82384
163	6.35734	2.06563	9.69948	363	6.35734	2.06563	21.82384
164	6.10660	2.71883	10.9119	364	6.10660	2.71883	23.03628
165	5.40788	3.92905	10.9119	365	5.40788	3.92905	23.03628
166	4.96756	4.47281	9.69948	366	4.96756	4.47281	21.82384
167	3.92905	5.40788	9.69948	367	3.92905	5.40788	21.82384

168	3.34225	5.78895	10.9119	368	3.34225	5.78895	23.03628
169	2.06563	6.35734	10.9119	369	2.06563	6.35734	23.03628
170	1.38979	6.53844	9.69948	370	1.38979	6.53844	21.82384
171	0.00000	6.68451	9.69948	371	0.00000	6.68451	21.82384
172	-0.69872	6.64789	10.9119	372	-0.69872	6.64789	23.03628
173	-2.06563	6.35734	10.9119	373	-2.06563	6.35734	23.03628
174	-2.71883	6.10660	9.69948	374	-2.71883	6.10660	21.82384
175	-3.92905	5.40788	9.69948	375	-3.92905	5.40788	21.82384
176	-4.47281	4.96756	10.9119	376	-4.47281	4.96756	23.03628
177	-5.40788	3.92905	10.9119	377	-5.40788	3.92905	23.03628
178	-5.78895	3.34225	9.69948	378	-5.78895	3.34225	21.82384
179	-6.35734	2.06563	9.69948	379	-6.35734	2.06563	21.82384
180	-6.53844	1.38979	10.9119	380	-6.53844	1.38979	23.03628
181	-6.68451	0.00000	10.9119	381	-6.68451	0.00000	23.03628
182	-6.64789	-0.69872	9.69948	382	-6.64789	-0.69872	21.82384
183	-6.35734	-2.06563	9.69948	383	-6.35734	-2.06563	21.82384
184	-6.10660	-2.71883	10.9119	384	-6.10660	-2.71883	23.03628
185	-5.40788	-3.92905	10.9119	385	-5.40788	-3.92905	23.03628
186	-4.96756	-4.47281	9.69948	386	-4.96756	-4.47281	21.82384
187	-3.92905	-5.40788	9.69948	387	-3.92905	-5.40788	21.82384
188	-3.34225	-5.78895	10.9119	388	-3.34225	-5.78895	23.03628
189	-2.06563	-6.35734	10.9119	389	-2.06563	-6.35734	23.03628
190	-1.38979	-6.53844	9.69948	390	-1.38979	-6.53844	21.82384
191	0.00000	-6.68451	9.69948	391	0.00000	-6.68451	21.82384
192	0.69872	-6.64789	10.9119	392	0.69872	-6.64789	23.03628
193	2.06563	-6.35734	10.9119	393	2.06563	-6.35734	23.03628
194	2.71883	-6.10660	9.69948	394	2.71883	-6.10660	21.82384
195	3.92905	-5.40788	9.69948	395	3.92905	-5.40788	21.82384
196	4.47281	-4.96756	10.9119	396	4.47281	-4.96756	23.03628
197	5.40788	-3.92905	10.9119	397	5.40788	-3.92905	23.03628
198	5.78895	-3.34225	9.69948	398	5.78895	-3.34225	21.82384
199	6.35734	-2.06563	9.69948	399	6.35734	-2.06563	21.82384
200	6.53844	-1.38979	10.9119	400	6.53844	-1.38979	23.03628

C.2 Coordinates for a section of a (10,0) buckytube

atom	x	y	z	atom	x	y	z
1	3.67041	1.19259	0	201	-3.67041	-1.19259	0
2	3.85930	0.00000	0.7	202	-3.85930	0.00000	0.7
3	3.85930	0.00000	2.1	203	-3.85930	0.00000	2.1
4	3.67041	1.19259	2.8	204	-3.67041	-1.19259	2.8
5	3.67041	1.19259	4.2	205	-3.67041	-1.19259	4.2
6	3.85930	0.00000	4.9	206	-3.85930	0.00000	4.9
7	3.85930	0.00000	6.3	207	-3.85930	0.00000	6.3
8	3.67041	1.19259	7	208	-3.67041	-1.19259	7
9	3.67041	1.19259	8.4	209	-3.67041	-1.19259	8.4
10	3.85930	0.00000	9.1	210	-3.85930	0.00000	9.1
11	3.85930	0.00000	10.	211	-3.85930	0.00000	10.5
12	3.67041	1.19259	11.	212	-3.67041	-1.19259	11.2
13	3.67041	1.19259	12.	213	-3.67041	-1.19259	12.6
14	3.85930	0.00000	13.	214	-3.85930	0.00000	13.3
15	3.85930	0.00000	14.	215	-3.85930	0.00000	14.7
16	3.67041	1.19259	15.	216	-3.67041	-1.19259	15.4
17	3.67041	1.19259	16.	217	-3.67041	-1.19259	16.8
18	3.85930	0.00000	17.	218	-3.85930	0.00000	17.5
19	3.85930	0.00000	18.	219	-3.85930	0.00000	18.9
20	3.67041	1.19259	19.	220	-3.67041	-1.19259	19.6
21	3.67041	1.19259	21	221	-3.67041	-1.19259	21
22	3.85930	0.00000	21.	222	-3.85930	0.00000	21.7
23	3.85930	0.00000	23.	223	-3.85930	0.00000	23.1
24	3.67041	1.19259	23.	224	-3.67041	-1.19259	23.8
25	3.67041	1.19259	25.	225	-3.67041	-1.19259	25.2
26	3.85930	0.00000	25.	226	-3.85930	0.00000	25.9
27	3.85930	0.00000	27.	227	-3.85930	0.00000	27.3
28	3.67041	1.19259	28	228	-3.67041	-1.19259	28
29	3.67041	1.19259	29.	229	-3.67041	-1.19259	29.4
30	3.85930	0.00000	30.	230	-3.85930	0.00000	30.1
31	3.85930	0.00000	31.	231	-3.85930	0.00000	31.5
32	3.67041	1.19259	32.	232	-3.67041	-1.19259	32.2

33	3.67041	1.19259	33.	233	-3.67041	-1.19259	33.6
34	3.85930	0.00000	34.	234	-3.85930	0.00000	34.3
35	3.85930	0.00000	35.	235	-3.85930	0.00000	35.7
36	3.67041	1.19259	36.	236	-3.67041	-1.19259	36.4
37	3.67041	1.19259	37.	237	-3.67041	-1.19259	37.8
38	3.85930	0.00000	38.	238	-3.85930	0.00000	38.5
39	3.85930	0.00000	39.	239	-3.85930	0.00000	39.9
40	3.67041	1.19259	40.	240	-3.67041	-1.19259	40.6
41	2.26844	3.12224	0	241	-2.26844	-3.12224	0
42	3.12224	2.26844	0.7	242	-3.12224	-2.26844	0.7
43	3.12224	2.26844	2.1	243	-3.12224	-2.26844	2.1
44	2.26844	3.12224	2.8	244	-2.26844	-3.12224	2.8
45	2.26844	3.12224	4.2	245	-2.26844	-3.12224	4.2
46	3.12224	2.26844	4.9	246	-3.12224	-2.26844	4.9
47	3.12224	2.26844	6.3	247	-3.12224	-2.26844	6.3
48	2.26844	3.12224	7	248	-2.26844	-3.12224	7
49	2.26844	3.12224	8.4	249	-2.26844	-3.12224	8.4
50	3.12224	2.26844	9.1	250	-3.12224	-2.26844	9.1
51	3.12224	2.26844	10.	251	-3.12224	-2.26844	10.5
52	2.26844	3.12224	11.	252	-2.26844	-3.12224	11.2
53	2.26844	3.12224	12.	253	-2.26844	-3.12224	12.6
54	3.12224	2.26844	13.	254	-3.12224	-2.26844	13.3
55	3.12224	2.26844	14.	255	-3.12224	-2.26844	14.7
56	2.26844	3.12224	15.	256	-2.26844	-3.12224	15.4
57	2.26844	3.12224	16.	257	-2.26844	-3.12224	16.8
58	3.12224	2.26844	17.	258	-3.12224	-2.26844	17.5
59	3.12224	2.26844	18.	259	-3.12224	-2.26844	18.9
60	2.26844	3.12224	19.	260	-2.26844	-3.12224	19.6
61	2.26844	3.12224	21	261	-2.26844	-3.12224	21
62	3.12224	2.26844	21.	262	-3.12224	-2.26844	21.7
63	3.12224	2.26844	23.	263	-3.12224	-2.26844	23.1
64	2.26844	3.12224	23.	264	-2.26844	-3.12224	23.8
65	2.26844	3.12224	25.	265	-2.26844	-3.12224	25.2
66	3.12224	2.26844	25.	266	-3.12224	-2.26844	25.9
67	3.12224	2.26844	27.	267	-3.12224	-2.26844	27.3

68	2.26844	3.12224	28	268	-2.26844	-3.12224	28
69	2.26844	3.12224	29.	269	-2.26844	-3.12224	29.4
70	3.12224	2.26844	30.	270	-3.12224	-2.26844	30.1
71	3.12224	2.26844	31.	271	-3.12224	-2.26844	31.5
72	2.26844	3.12224	32.	272	-2.26844	-3.12224	32.2
73	2.26844	3.12224	33.	273	-2.26844	-3.12224	33.6
74	3.12224	2.26844	34.	274	-3.12224	-2.26844	34.3
75	3.12224	2.26844	35.	275	-3.12224	-2.26844	35.7
76	2.26844	3.12224	36.	276	-2.26844	-3.12224	36.4
77	2.26844	3.12224	37.	277	-2.26844	-3.12224	37.8
78	3.12224	2.26844	38.	278	-3.12224	-2.26844	38.5
79	3.12224	2.26844	39.	279	-3.12224	-2.26844	39.9
80	2.26844	3.12224	40.	280	-2.26844	-3.12224	40.6
81	0.00000	3.85930	0	281	0.00000	-3.85930	0
82	1.19259	3.67041	0.7	282	-1.19259	-3.67041	0.7
83	1.19259	3.67041	2.1	283	-1.19259	-3.67041	2.1
84	0.00000	3.85930	2.8	284	0.00000	-3.85930	2.8
85	0.00000	3.85930	4.2	285	0.00000	-3.85930	4.2
86	1.19259	3.67041	4.9	286	-1.19259	-3.67041	4.9
87	1.19259	3.67041	6.3	287	-1.19259	-3.67041	6.3
88	0.00000	3.85930	7	288	0.00000	-3.85930	7
89	0.00000	3.85930	8.4	289	0.00000	-3.85930	8.4
90	1.19259	3.67041	9.1	290	-1.19259	-3.67041	9.1
91	1.19259	3.67041	10.	291	-1.19259	-3.67041	10.5
92	0.00000	3.85930	11.	292	0.00000	-3.85930	11.2
93	0.00000	3.85930	12.	293	0.00000	-3.85930	12.6
94	1.19259	3.67041	13.	294	-1.19259	-3.67041	13.3
95	1.19259	3.67041	14.	295	-1.19259	-3.67041	14.7
96	0.00000	3.85930	15.	296	0.00000	-3.85930	15.4
97	0.00000	3.85930	16.	297	0.00000	-3.85930	16.8
98	1.19259	3.67041	17.	298	-1.19259	-3.67041	17.5
99	1.19259	3.67041	18.	299	-1.19259	-3.67041	18.9
100	0.00000	3.85930	19.	300	0.00000	-3.85930	19.6
101	0.00000	3.85930	21	301	0.00000	-3.85930	21
102	1.19259	3.67041	21.	302	-1.19259	-3.67041	21.7

103	1.19259	3.67041	23.	303	-1.19259	-3.67041	23.1
104	0.00000	3.85930	23.	304	0.00000	-3.85930	23.8
105	0.00000	3.85930	25.	305	0.00000	-3.85930	25.2
106	1.19259	3.67041	25.	306	-1.19259	-3.67041	25.9
107	1.19259	3.67041	27.	307	-1.19259	-3.67041	27.3
108	0.00000	3.85930	28	308	0.00000	-3.85930	28
109	0.00000	3.85930	29.	309	0.00000	-3.85930	29.4
110	1.19259	3.67041	30.	310	-1.19259	-3.67041	30.1
111	1.19259	3.67041	31.	311	-1.19259	-3.67041	31.5
112	0.00000	3.85930	32.	312	0.00000	-3.85930	32.2
113	0.00000	3.85930	33.	313	0.00000	-3.85930	33.6
114	1.19259	3.67041	34.	314	-1.19259	-3.67041	34.3
115	1.19259	3.67041	35.	315	-1.19259	-3.67041	35.7
116	0.00000	3.85930	36.	316	0.00000	-3.85930	36.4
117	0.00000	3.85930	37.	317	0.00000	-3.85930	37.8
118	1.19259	3.67041	38.	318	-1.19259	-3.67041	38.5
119	1.19259	3.67041	39.	319	-1.19259	-3.67041	39.9
120	0.00000	3.85930	40.	320	0.00000	-3.85930	40.6
121	-2.26844	3.12224	0	321	2.26844	-3.12224	0
122	-1.19259	3.67041	0.7	322	1.19259	-3.67041	0.7
123	-1.19259	3.67041	2.1	323	1.19259	-3.67041	2.1
124	-2.26844	3.12224	2.8	324	2.26844	-3.12224	2.8
125	-2.26844	3.12224	4.2	325	2.26844	-3.12224	4.2
126	-1.19259	3.67041	4.9	326	1.19259	-3.67041	4.9
127	-1.19259	3.67041	6.3	327	1.19259	-3.67041	6.3
128	-2.26844	3.12224	7	328	2.26844	-3.12224	7
129	-2.26844	3.12224	8.4	329	2.26844	-3.12224	8.4
130	-1.19259	3.67041	9.1	330	1.19259	-3.67041	9.1
131	-1.19259	3.67041	10.	331	1.19259	-3.67041	10.5
132	-2.26844	3.12224	11.	332	2.26844	-3.12224	11.2
133	-2.26844	3.12224	12.	333	2.26844	-3.12224	12.6
134	-1.19259	3.67041	13.	334	1.19259	-3.67041	13.3
135	-1.19259	3.67041	14.	335	1.19259	-3.67041	14.7
136	-2.26844	3.12224	15.	336	2.26844	-3.12224	15.4
137	-2.26844	3.12224	16.	337	2.26844	-3.12224	16.8

138	-1.19259	3.67041	17.	338	1.19259	-3.67041	17.5
139	-1.19259	3.67041	18.	339	1.19259	-3.67041	18.9
140	-2.26844	3.12224	19.	340	2.26844	-3.12224	19.6
141	-2.26844	3.12224	21	341	2.26844	-3.12224	21
142	-1.19259	3.67041	21.	342	1.19259	-3.67041	21.7
143	-1.19259	3.67041	23.	343	1.19259	-3.67041	23.1
144	-2.26844	3.12224	23.	344	2.26844	-3.12224	23.8
145	-2.26844	3.12224	25.	345	2.26844	-3.12224	25.2
146	-1.19259	3.67041	25.	346	1.19259	-3.67041	25.9
147	-1.19259	3.67041	27.	347	1.19259	-3.67041	27.3
148	-2.26844	3.12224	28	348	2.26844	-3.12224	28
149	-2.26844	3.12224	29.	349	2.26844	-3.12224	29.4
150	-1.19259	3.67041	30.	350	1.19259	-3.67041	30.1
151	-1.19259	3.67041	31.	351	1.19259	-3.67041	31.5
152	-2.26844	3.12224	32.	352	2.26844	-3.12224	32.2
153	-2.26844	3.12224	33.	353	2.26844	-3.12224	33.6
154	-1.19259	3.67041	34.	354	1.19259	-3.67041	34.3
155	-1.19259	3.67041	35.	355	1.19259	-3.67041	35.7
156	-2.26844	3.12224	36.	356	2.26844	-3.12224	36.4
157	-2.26844	3.12224	37.	357	2.26844	-3.12224	37.8
158	-1.19259	3.67041	38.	358	1.19259	-3.67041	38.5
159	-1.19259	3.67041	39.	359	1.19259	-3.67041	39.9
160	-2.26844	3.12224	40.	360	2.26844	-3.12224	40.6
161	-3.67041	1.19259	0	361	3.67041	-1.19259	0
162	-3.12224	2.26844	0.7	362	3.12224	-2.26844	0.7
163	-3.12224	2.26844	2.1	363	3.12224	-2.26844	2.1
164	-3.67041	1.19259	2.8	364	3.67041	-1.19259	2.8
165	-3.67041	1.19259	4.2	365	3.67041	-1.19259	4.2
166	-3.12224	2.26844	4.9	366	3.12224	-2.26844	4.9
167	-3.12224	2.26844	6.3	367	3.12224	-2.26844	6.3
168	-3.67041	1.19259	7	368	3.67041	-1.19259	7
169	-3.67041	1.19259	8.4	369	3.67041	-1.19259	8.4
170	-3.12224	2.26844	9.1	370	3.12224	-2.26844	9.1
171	-3.12224	2.26844	10.	371	3.12224	-2.26844	10.5
172	-3.67041	1.19259	11.	372	3.67041	-1.19259	11.2

173	-3.67041	1.19259	12.	373	3.67041	-1.19259	12.6
174	-3.12224	2.26844	13.	374	3.12224	-2.26844	13.3
175	-3.12224	2.26844	14.	375	3.12224	-2.26844	14.7
176	-3.67041	1.19259	15.	376	3.67041	-1.19259	15.4
177	-3.67041	1.19259	16.	377	3.67041	-1.19259	16.8
178	-3.12224	2.26844	17.	378	3.12224	-2.26844	17.5
179	-3.12224	2.26844	18.	379	3.12224	-2.26844	18.9
180	-3.67041	1.19259	19.	380	3.67041	-1.19259	19.6
181	-3.67041	1.19259	21	381	3.67041	-1.19259	21
182	-3.12224	2.26844	21.	382	3.12224	-2.26844	21.7
183	-3.12224	2.26844	23.	383	3.12224	-2.26844	23.1
184	-3.67041	1.19259	23.	384	3.67041	-1.19259	23.8
185	-3.67041	1.19259	25.	385	3.67041	-1.19259	25.2
186	-3.12224	2.26844	25.	386	3.12224	-2.26844	25.9
187	-3.12224	2.26844	27.	387	3.12224	-2.26844	27.3
188	-3.67041	1.19259	28	388	3.67041	-1.19259	28
189	-3.67041	1.19259	29.	389	3.67041	-1.19259	29.4
190	-3.12224	2.26844	30.	390	3.12224	-2.26844	30.1
191	-3.12224	2.26844	31.	391	3.12224	-2.26844	31.5
192	-3.67041	1.19259	32.	392	3.67041	-1.19259	32.2
193	-3.67041	1.19259	33.	393	3.67041	-1.19259	33.6
194	-3.12224	2.26844	34.	394	3.12224	-2.26844	34.3
195	-3.12224	2.26844	35.	395	3.12224	-2.26844	35.7
196	-3.67041	1.19259	36.	396	3.67041	-1.19259	36.4
197	-3.67041	1.19259	37.	397	3.67041	-1.19259	37.8
198	-3.12224	2.26844	38.	398	3.12224	-2.26844	38.5
199	-3.12224	2.26844	39.	399	3.12224	-2.26844	39.9
200	-3.67041	1.19259	40.	400	3.67041	-1.19259	40.6

VITA

Appendix C: VITA

Daniel Lee Lovall was born in Gary, Indiana on April 27, 1966. He was raised in Hobart, IN and later in Portage, IN. Daniel graduated from Purdue University in December, 1989 with a B.S. in Applied Physics. He attended San Diego State University in fall of 1991 as a non-degree student, and returned to Purdue in the fall of 1992. He received his M.S. Physics in May, 1994.